Advanced High Speed Data and Clock Transmission over Optical Fibre for Square Kilometre Telescope Array

By

George Mosoti Isoe

Submitted in fulfilment of the requirements for the degree of

Philosophiae Doctor

to be awarded at the

Nelson Mandela University

April 2018

Promoter

Prof. Timothy Gibbon

Co-promoters

Prof. Andrew Leitch

Dr. Romeo Gamatham

Dedication

This thesis is dedicated to my family

Declaration

I, *George Mosoti Isoe, Student number: s215245407*, hereby declare that the thesis for PhD award is my own work and that it has not previously been submitted for assessment or completion of any postgraduate qualification to another University or for another qualification.

George Mosoti Isoe

Acknowledgement

First and foremost, am very grateful to the almighty God for the gift of life, good health and for the strength He gave me during the entire my research period. This thesis would not have been possible without the guidance and encouragement from my promotor prof. Timothy Gibbon. Your constant intellectual challenge, scientific insights, enthusiasm, and accurate suggestions are the reasons that I am able to get this far. I am deeply humbled by your constant mind opening suggestions, many encouragements and discussions that generated new ideas and perceptions towards this works. I would also like to thank Prof. Andrew Leitch for giving me an opportunity to learn under him to acquire skills in high speed optical communication thereby molding my future in a special way. To Dr Romeo Gamatham, thank you for agreeing to serve as my co-promoter and for your great contribution towards this work. To my former supervisors Dr David Waswa and Dr. Kennedy Muguro, thank you very much for nurturing me. Special regards to Mrs. Alta McCleland for her continuous support and assistance to the Centre for Broadband Communication over my entire study period. I am very grateful to Nelson Mandela University in particular the Physics department for offering me this opportunity to complete my PhD studies. I am very grateful for research funding and support from: Telkom, Dartcom, Ingoma, CISCO, DST, CSIR, NLC, NRF, THRIP, ALC and scholarship funding from SKA/NRF. To my colleagues at Centre for Broadband Communication, I thank each and every one of you for the love and support through our student life.

Finally I convey gratitude to all members of my family for their moral support throughout this period. I appreciate great encouragement and prayers from my parents Mr. and Mrs. Isoe and my siblings Annette and Emmy. Many thanks to my wife Metrine and our daughter Lindsey for being very supportive, focused and patient all along.

Contents

List of figures

List of tables

Abstract

There is an ever present need from Internet users for more bandwidth. This is manifested by continuous increase in bandwidth demanding applications such as 5G wireless, new end user consumer links like thunderbolt, video conferencing, high definition video-on-demand transmitted over the Internet and massive data transfers required with and within data centres for backup, storage and data processing in cloud computing. Fibre optic communications technologies are playing a pivotal role in communication, being a major enabling technology in our increasingly Internet-centric society.

As network services continue to become more dynamic and diverse, Internet service providers are faced with a challenge of cost reduction in the transmission network, power and spectral efficiency as well as scalability of the optical network infrastructure to support incremental expansions and virtual machines. Intelligent design of terrestrial optical networks to allow for simultaneous signal transmission through shared network infrastructure, and the use of low cost, power efficient, high bandwidth transmitters such as vertical surface emitting lasers (VCSELs) as well as exploitation of spectral efficient in-complex advanced modulation formats is a viable approach to this situation.

In this study, techniques for spectral efficiency upgrade and simultaneous transmission of data signal, reference frequency (RF) clock signal and pulse-per-second (PPS) over shared infrastructure have experimentally been optimized in a laboratory environment for adoption in next-generation telescope array networks such as the Square Kilometre Array (SKA), time keeping systems such as banking systems, Coordinated Universal Time(UTC) timing and Global Positioning Systems (GPS), as well as high capacity spectral efficient short reach optical fibre networks such as data centres.

This work starts by experimentally optimizing VCSEL technology for simultaneous transmission of 10 Gbps data and 1.712 GHz RF clock signal over a single G. 655 optical fibre of length 24.75 Km at different channel spacing and different propagation direction for implementation in a cost effective next-generation telescope array network. The wavelength tuneability property of VCSEL transmitters allows for wavelength adjustment, a key requirement for simultaneous data and RF clock signal transmission over a single optical fibre. A receiver sensitivity of -19.19 dBm was experimentally achieved at back-to-back analysis. A 24.75 Km of simultaneous data and RF clock signal transmission performed at 0.4 nm channel spacing introduced a transmission penalty of 1.07 dB and 1.63 dB for counter and co-propagation scheme respectively.

This work mainly utilized direct modulation and direct detection using a positive intrinsic negative (PIN) due to its simplicity and cost effectiveness. A novel modulation technique for simultaneous data and polarization-based pulse-per-second timing clock signal transmission using a single VCSEL carrier is experimentally demonstrated. Two signal types, a directly modulated 10 Gbps data signal and a polarization-based pulse per second (PPS) clock signal are modulated onto a single mode 10 GHz bandwidth VCSEL carrier at 1310 nm. Spectral efficiency is maximized by exploiting the inherent orthogonal polarization switching of the

VCSEL with changing bias in transmission of the PPS signal. A 10 Gbps VCSEL transmission with PPS over 11 Km of G.652 fibre introduced a transmission penalty of 0.52 dB. The contribution of PPS clock signal to this penalty was found to be 0.08 dB.

A technique for simultaneous directly modulated data and phase modulated reference clock signal transmission over a signal channel in wavelength division multiplexing (WDM) solutions is experimentally demonstrated. This is to prepare solutions to the ever-increasing demand over gigabit/s, terabit/s and gigahertz capacities in WDM-based terrestrial optical fibre transmission systems such as telescope array networks. a total capacity of 30 Gbps (3×10 Gbps) data and 12 GHz (3×4 GHz) reference clock signal are multiplexed at a channel spacing of 100 GHz and simultaneously transmitted over a single mode G.655 fibre of length 24.73 Km. The recovery of the phase modulated RF clock signal using a differential delay line interferometry technique is experimentally demonstrated. A 625 Gbps (25×25 Gbps) DWDM data transmission system is further implemented in simulation by multiplexing 25 channels at 25 Gbps per channel using 50 GHz channel spacing.

A four level pulse amplitude modulation (4-PAM) data modulation format employing VCSELs is experimentally demonstrated for adoption in high bitrate networks such as big data science projects and data centre networks. 4-PAM offers a good trade-off between complexity, efficiency, reach, and sensitivity. A software defined digital signal processing (DSP) receiver is designed and implemented in MATLAB to recover the transmitted 4-PAM data signal cost effectively without the necessity of costly receiver hardware. A novel technique for maximizing carrier spectral efficiency through simultaneous 20 Gbps 4-PAM data and phase modulated 2 GHz RF clock signal transmission on a single mode 10 GHz bandwidth VCSEL carrier at 1310 nm is experimentally demonstrated for the first time to the best of our knowledge. Data transmission and clock stability performance of the designed high spectral efficient VCSEL-based link network is evaluated through BER curve plots, phase noise measurements and Allan variance analysis respectively. VCSEL-based Raman amplification is experimentally demonstrated as a viable approach for RF clock signal distribution in extended reach astronomical telescope array networks and other extended reach terrestrial optical fibre network application. This is achieved by adopting two pumping techniques namely forward pumping and backward pumping. A maximum on off gain of 5.7 dB and 1.5 dB was experimentally attained for forward pumping and backward pumping at 24 dBm pump power respectively, while a maximum 100.8 Km fibre transmission achieved experimentally.

In summary, this study has successfully demonstrated in-complex, spectral efficient, low cost and power efficient simultaneous data signal, reference frequency (RF) clock signal and pulse-per-second (PPS) transmission techniques over shared network infrastructure. Simultaneous transmission of data, RF clock and PPS timing signal is relevant in next-generation telescope array networks such as the Square Kilometre Array (SKA), time keeping systems such as banking systems, Coordinated Universal Time (UTC) timing and Global Positioning Systems (GPS), as well as high capacity spectral efficient short reach optical fibre networks such as data centres.

Keywords: *Vertical surface emitting laser, Square Kilometre Array, pulse-per-second, reference frequency, Raman Amplification, Signal impairments, WDM, polarization modulation, PAM, optical fibre network, data transmission, clock distribution*

List of acronyms

B2B - Back-to-Back

BER – Bit error ratio

BERT- Bit error rate tester

CO – Central office

DWDM - Dense wavelength division multiplexing

ER – Extinction ratio

ISI – Inter symbol interference

KAPB - Karoo processing building

MMF – Multimode fibre

NRZ – Non-return to zero

OLT - Optical line terminal

ONU - Optical network unit

OOK – On-off keying

P2MP - Point to multi-point

P2P – Point-to-point

PAM - Pulse amplitude modulation

PC - polarization controller

PD - Photodiode

PIN - Positive intrinsic negative

PMD – Polarization mode dispersion

PON - Passive optical network

PPS - Pulse per second.

QoS - Quality of signal

RF – Reference frequency

RS - Reduced slope

RX – Receiver

SKA - the Square Kilometre Array

SMF – Single mode fibre

SNR – Signal to noise ratio

SOA – Semiconductor optical amplifier

SOP - States of polarization

SSB - Single side band

TX – Transmitter

VCSEL – Vertical cavity surface emitting laser

VOA - Variable optical attenuator

WDM - Wavelength division multiplexing

UTC – Coordinated Universal Time

GPS – Global Positioning Systems

Chapter 1

Introduction

Communication industry has been experiencing dramatic changes in the recent past. Over the last decade, network traffic has been increasing exponentially and this trend is anticipated to continue for the next several years. This is driven by emerging high bandwidth demanding applications, such as 5 G wireless, Internet of things (IoT), high-definition video streaming, cloud computing and new consumer links such as thunder bolts. This situation is creating a pressing need for high scalable optical communication systems, as network services continue to become more dynamic and diverse. With bandwidth limitation of electrical signal based technologies such as digital subscriber line techniques (DSL, ADL and VDL) and cabled modem as well as reach limitation of free-space optical transmission techniques due to high signal attenuation in air, optical fibre-based transmission technologies are a viable approach. The high bandwidth of optical fibres and developments in semiconductor lasers and photodetectors have seen the adoption of optical fibre communication technologies in modern communication systems. Moreover, network service providers are further facing a challenge of developing new business models through innovation of their existing network infrastructure to support an ever-increasing number of end-user mobile devices, user base mobile applications and virtual machines. Extending the bit rate on such links will therefore require the use of advanced modulation formats. Modern optical fibre communication links are also expected to comply with strict power consumption, cost and size limitations to allow for integration with optical interconnects to further increase their capacities. This has seen the adoption of high-speed, low cost vertical cavity surface emitting lasers (VCSELs) in optical communication systems.

Optical fibre networks also forms the transmission layer of data, timing and reference frequency (TRF) control and monitoring signals of big data science projects (telescope array networks) such as the Square Kilometre Array (SKA). The SKA is an international science project in the field of radio astronomy to build a next generation radio telescope. The SKA will push the boundaries of science into the dark ages of our universe before the formation of the first stars. Optical fibres forms the backbone of this mega science project. This is because optical fibres are immune to electromagnetic interference (EMI) therefore ensuring effective distribution of RF timing signals for control and monitoring function on the dish. The SKA phase 1, the MeerKAT is made up of 64 interconnected dishes with a maximum baseline of 12 Km. Moreover, with the spiral arms of the SKA project extending to baselines over 3000 Km across other partner countries, distance is a key aspect in realization of the observational objectives of the project.

This thesis presents viable techniques for capacity, efficiency and flexibility upgrade of optical fibre communication systems such as next-generation telescope array networks, access-networks and high capacity short-reach optical communication systems like data centre networks (DCNs). Energy and cost-effective techniques for providing simultaneous transmission of data and RF clock signal over shared network infrastructure are presented. Focus has been emphasized on various technique for implementing simultaneous transmission of data and timing clock signals in optical fibre communication networks using high bandwidth, wavelength tunable, low cost and power efficient single mode VCSEL transmitters. Simultaneous data and RF clock tone transmission over a single optical fibre has been demonstrated as a viable approach to minimize the installation cost of next-generation telescope array networks.

This study has experimentally demonstrated the first reported simultaneous data and polarization-based pulse-per-second (PPS) signal transmission using a single mode 10 GHz bandwidth VCSEL carrier, for time keeping applications such as UCT timing, GPS, banking and big data science project. A novel technique for capacity upgrade in high-speed short-reach networks such as DCN has experimentally been demonstrated through the combined use of VCSEL-based 4-PAM and phase modulation in simultaneous transmission of 20 Gbps 4-PAM data and 2 GHz phase modulated RF clock signal over a single mode VCSEL carrier at 1310 nm. For the first time to the best of our knowledge, this study has successfully demonstrated a cost effective and energy efficient multi-signal modulation technique for multicast transmission systems in cloud computing and efficiency upgrade in DCNs. This has experimentally been achieved by multiple-signal modulation on a signal VCSEL carrier in simultaneous transmission of 10 Gbps data, 2 GHz RF clock tone and PPS timing signal over a single mode 10 GHz VCSEL carriers. The potential of Raman amplification for RF clock signal distribution in extended reach astronomical telescope array networks and other long reach terrestrial optical fibre network applications has been demonstrated experimentally.

1.1 Outline of the thesis

This thesis is structured as follows; chapter 1 introduces the growth of bandwidth demand in modern communication systems and the need for optical communication technologies in big data science projects like SKA, high capacity short-range networks such as data centre networks, as well as the importance for simultaneous data and RF clock signal transmission over shared infrastructure for next-generation terrestrial optical communication networks. Chapter 2 gives a brief overview of the SKA and describes the SKA data and clock transport requirements.

This chapter also presents existing state-of-the-art astronomical telescopes. Chapter 3 starts by presenting a review of precisely stable state-of-the-art reference frequency dissemination and synchronization systems. Different clock stability measurement techniques are presented in this chapter. This is then followed by a discussion on Allan variance. High capacity data transmission techniques are presented in chapter 4. This chapter begins with VCSEL technology in simultaneous transmission of data and RF clock signal. Advanced modulation techniques for VCSEL-based links are then presented. This is followed by some state-of-the-art experiments employing VCSELs. Different modulation techniques (and their realization) like NRZ, 4-PAM and polarization modulation are then discussed. This chapter concludes with a discussion on fibre impairments in optical communication links that affect signal quality such as chromatic dispersion, attenuation and modal dispersion.

Chapter 5 to 9 presents experimental and simulation research findings of this work as performed in a laboratory test bed. Chapter 5 begins by demonstrating VCSEL technology as an ideal candidate for adoption in next-generation high-speed terrestrial optical fibre networks. The use of VCSELs in simultaneous data and reference frequency (RF) clock signal transmission in next-generation telescope array networks is proposed and experimentally verified at different channel spacing and direction of propagation. Chapter 6 reports on a novel modulation technique for simultaneous data and polarization-based Pulse-Per-Second clock signal transmission using a single mode 10 GHz bandwidth VCSEL carrier.

Chapter 7 reports on simultaneous directly modulated data and phase modulated reference clock signal transmission over a single wavelength in WDM solutions. A differential delay line interferometry technique is also developed and used to recover the simultaneous phase modulated RF clock signal. The relevance of WDM solutions for simultaneous data and RF clock signal transmission in telescope array networks is reported. Chapter 8 reports on a VCSEL-based 4-PAM data modulation format for adoption in high bitrate networks such as big data science project and data centre networks. A novel technique for maximizing carrier spectral efficiency through simultaneous 20 Gbps 4-PAM data and phase modulated 2 GHz reference frequency (RF) clock signal transmission on a single mode 10 GHz bandwidth VCSEL carrier at 1310 nm is reported for the first time to the best of our knowledge.

Chapter 9 presents the potential of Raman amplification for RF clock signal distribution in extended reach astronomical telescope array networks and other extended reach terrestrial optical fibre network applications. This chapter begins by experimentally optimizing the Raman gain. This is then followed by experimental demonstration of Raman amplification in extended reach clock signal distribution then concludes by presenting the stability analysis of Raman-based 2 GHz reference frequency clock signal distribution. Chapter 10 summarizes the findings of this thesis. It is then followed by references and appendices.

Chapter 2

The Square Kilometre Array and other existing state of the art astronomical observatory facilities

2.1 The Square Kilometre Array

Radio astronomy has produced some of the greatest discoveries of the 20th century. Advances in astronomy over the past decades have brought the international community to the verge of charting a complete history of the universe. In order to achieve this goal, the world community is pooling resources and expertise to design and construct powerful observatories that will probe the entire electromagnetic spectrum, from radio to gamma rays, and beyond the electromagnetic spectrum, studying gravitational waves, cosmic rays, and neutrinos. One of such extraordinary observatory facility is the Square Kilometre Array (SKA) radio telescope [1-3]. The SKA will be the largest radio telescope ever build and will produce science that will change our understanding of the universe. The SKA will be co-located in Australia and Africa, with the MeerKAT telescope in South Africa and Australian Square Kilometre Array pathfinder (ASKAP) in Australia makeup precursors to SKA respectively [4, 5].

South Africa will host the medium frequency aperture arrays dish receivers, constructed at the Karoo region, while Australia will host the low frequency aperture arrays dish receivers constructed at Boolardy station western Australia [6, 7]. These sites were carefully selected because they are sparsely populated therefore minimum chances for radio frequency interference (RFI). SKA Phase 1, the MeerKAT radio telescope is the largest science and engineering project ever undertaken in South Africa [8]. This project is being developed in several interlinked phases which include; the construction (Carnavon) and remote operation (Cape Town) of the technology demonstrator KAT-7, the critical human capacity development programme in South Africa and associated SKA Africa partner countries (Botswana, Ghana, Kenya, Madagascar, Mauritius, Mozambique, Namibia, and Zambia), and lastly the integration of the MeerKAT array into phase 1 of the international SKA project [9]. A picture of the location of SKA radio telescopes in South Africa, and other African partner countries is shown in fig 2.1. Upon its completion, the MeerKAT will be the most sensitive radio interferometer in the L-band (1-2 GHz) [6, 10].

The MeerKAT telescope is an array of 64 interlinked receptors whose configuration is dictated by the scientific objective on the telescope. 48 of these receptors will be concentrated in the core are with an approximate of 1 Km diameter, with a maximum baseline of 8 Km. Other dishes will be distribute across SKA Africa partner countries to form the African very long baseline interferometry (VLBI) Network composing approximately 3000 dish antennae spreading to about 3000 Km from the central core [11]. South Africa's Karoo Array Telescope KAT-7 is the first of the 64 MeerKAT interlinked telescopes to be completed, and is currently used as a test array [12]. The first significant scientific results from KAT-7 test array have already been reported in the astronomical literature [4, 9, 12-17]. This marks a major milestone on the path to the SKA in Africa, and highlights the commencement of cutting-edge science observations with South Africa's new radio interferometer.

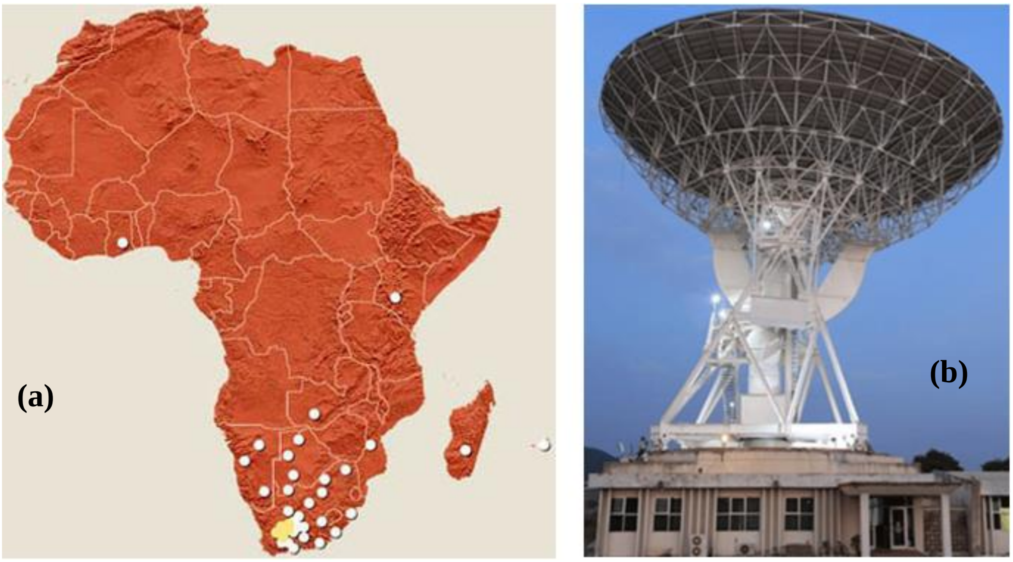

Fig 2.1: The location of SKA radio telescopes in South Africa, and other African partner countries (a); the Ghana 32 m telescope antenna (b).

Ghana is the first African partner country of the VLBI network to complete the conversion of a communication antenna into a functioning SKA radio telescope. An image of Ghana SKA radio telescope is shown in fig 2.1. The 32-metre converted telecommunications antenna at the Ghana Intelsat satellite earth station at Kutunse will be integrated into the African VLBI network in preparation for the second phase construction of the SKA across the African continent [18]. The science observational objective of this telescope includes methanol maser detections, VLBI fringe testing and pulsar observations [19-21]. A team of scientists and engineers from SKA SA/HartRAO and the Ghana space science and technology institute (GSSTI), has been researching on the effect of RFI and how well the antenna does a full rotation. For phase 1, the existing telecommunication feed horn was used in the frequency range of 3.8 – 6.4 GHz (C-band) [19]. For the actual science observations (Phase 2), an uncooled 5 GHz and 6.7 GHz (C-band) receivers were fitted. Future receiver developments may include replacing the original C-band feed horn with a wider band design covering more VLBI bands and introducing cryogenic receivers for improved sensitivity and adding more frequency bands [19]. Following the initial '*first light*' observations of the telescope [19], the research teams from Ghana and South Africa together with other international research partners, continue to do more observations and are analyzing the data generated from this telescope with an aim to characterize the system and optimize its accuracy for future astronomical experiments [20-25].

2.2 The SKA data and clock signal transport over optical fibres

Optical fibres links forms the backbone of data and clock signal transport in SKA telescope array network. Individual remote antennae in the SKA phase 1 are inter-linked to a central processor station with a total of 24 stands of optical fibres (12 fibres of G. 652 and 12 fibres of G. 655) [26]. Optical communication is required to aggregate science data from remote dishes to a central computing science station. After a fast, high resolution sampling process by digitizers mounted on each receptor, each dish collects enormous amount of data, which needs to be transmitted to a central processor computer engine [2, 27, 28]. Phase 1 of the SKA radio telescopes will collect up to 160 Gbps of science data per dish by 2018 [6]. However, upon its completion, the SKA dish array will make use of the wide field of view expansion technology to collect up to 120 Tbps of astronomical data [27]. Optical fibre further distributes centrally generate reference frequency (RF) clock signals to individual antennae elements, as well as transferring monitoring and control signals. Stable RF clock tones are required for phase coherence of the antennae array, absolute time code for dish controllers and beam forming as well as accurate timing ticks and counters for data stamping [2, 27].

Synchronization and timing in telescope array networks is therefore required to meet important astronomical observational objectives. A central reference clock system consisting of a single clock or an ensemble of clocks is distributed over fibre to remote antennae elements. Distribution of clock tones over fibre to each antennae element ensures phase coherence of the entire telescope array network. Phase coherence in the order of picoseconds and below is required over time intervals ranging from one second to tens of minutes, depending on the nature of the observational objective. The stability, accuracy and precision of the reference clock frequency depends on the science observational objective [29, 30]. Table 2.1 shows the clock frequencies for MeerKAT and SKA, with the clock stability budget for expressed in picoseconds (ps) for a 0.2 radian phase error.

Table 2.1: Clock frequencies for MeerKAT and SKA, with the clock stability budget for expressed in ps for a 0.2 radian phase error [26].

	Clock (GHz)	Clock stability budget (ps)
MeerKAT L-band	1.712	18.6
MeerKAT X-band/ SKA Phase 1 mid	14	2.2
SKA Phase 2	20	1.6

Typically, Hydrogen maser, Rubidium or Cesium reference clocks are used [31-34]. Depending on the implementation details, clock tones are required to provide accurate frequency standards at the dishes for local oscillators, phase locked loops, digitization, time stamping and related functions[30].

2.3 Review of existing state of the art astronomical telescopes like the SKA

There are several astronomical observatory facilities in the world that portray some similarities to the SKA in terms of design, operational objective and magnitude of the total collective area [35-44]. The Australian SKA Pathfinder (ASKAP) is one of such astronomical observatory. ASKAP is a precursor and technology demonstrator for the SKA [45-47]. A specialist wide-field survey instrument, ASKAP is made up of 36 antennae each 12 m in diameter working as a single instrument with a maximum baseline of 6 Km [48]. Each dish is mounted with a 'phased array feed', a radio receiver that dramatically enhances the telescope's field-of-view from 1 to 30 square degrees [49]. ASKAP is located at the Murchison radio-astronomy observatory, Australia's core site for the SKA with possible remote array station capability located in NSW, approximately 3,000 Km from the core site. Astronomical research topics tackled by ASKAP include galaxy evolution, cosmic magnetism, the history of gas in galaxies and cosmology [50, 51]. A program of ASKAP early science commenced in October 2016 using an array of 12 antennas. The 6-antenna Boolardy Engineering Test Array (BETA) is currently being used by the commissioning team and has already produced its first scientific discovery results [45, 52-55]. The results demonstrate exciting new capabilities of ASKAP and learning about the first scientific discoveries made by the commissioning and early science team.

Atacama large millimeter array (ALMA) located in the Atacama desert north of the republic of Chile comprises of 66 high-precision antennas, which operates on wavelengths of 0.32 mm to 3.6 mm [56, 57]. Its main array has fifty antennas, each with 12 m diameters, which act together as a single interferometry telescope. This is complemented by a compact array of four antennas with 12 m diameters and 12 antennas with 7 m diameters [58]. ALMA’s antennas can be configured in different ways, spacing them at distances from 150 m to 16 Km, giving ALMA a powerful “*zoom*” variable, which results in images clearer than the images from other space telescopes of similar objective [56, 59, 60]. ALMA uses optical fibres to transmit astronomical data and all kinds of observatory communications for necessary processes of data reception from the antennas [60]. The frequencies received by ALMA from the universe start at 30 GHz and reach their maximum capacity at 950 GHz [57]. Local oscillators (LO) are used to process these signals, which, under the heterodyne principle, reduce the frequency received from space to one that can be processed, in this case between 2 GHz and 4 GHz. This is why ALMA has two oscillators for each antenna: one at the front end and another at the back end [58]. ALMA started its scientific operations in September 2011 while still under construction with only 16 antennas. Since that time, it has achieved numerous discoveries [61]. The first scientific image published by ALMA revealed massive concentrations of gas in the collision zones, a rich reserve of matter for future generations of stars [62]. In April 2012, ALMA made another discovery by obtaining an unprecedented image of the disc surrounding the star orbiting right between two planets. Since then, ALMA has consistently delivered some of its most unique and spectacular results [61, 63-83].

The e-MARLIN is a 7-interferometer array radio telescope located in the United Kingdom (UK). The array consists of 7 radio telescopes operating at 151 MHz and 24 GHz with a resolution of up to 40 ms at 5 GHz and a maximum baseline of 217 Km. Each telescope streams 30 Gbps of astronomical data at L band, C band and K band [84]. Just like other telescope array networks of similar kind, e-MERLIN has delivered some of its most unique results [85-88]. The e-MERLIN as part of a multi-wavelength study of a pair of colliding galaxies has recently revealed the cause of a supermassive black hole's case of '*indigestion*' [89].

These described observatory facilities uses optical fibres to transmit astronomical data as well as distribute control and monitoring signals to achieve their scientific observational objectives. The ultimate objective of these telescope arrays is to improve quality of service, reliability and have reasonable implementation and running cost. Scientific projects of this magnitude therefore calls for intelligent technological design selection in the telescope array network design and implementation stage, if its observational science objectives are to be achieved, and for prove of technologies and scalability at later stages.

In summary, an overview of the SKA and a description of the SKA data and clock requirements has been presented in this chapter. A review of state of the art astronomical observatory facilities like the SKA has also been reported. The next chapter discusses on State-of-the-Art frequency dissemination and synchronisation systems. This chapter also reports on precisely stable reference frequency dissemination and synchronisation systems as well as different reference clock stability measurement techniques.

Chapter 3

State-of-the-art frequency dissemination and synchronization systems

3.1 Review of precisely stable reference frequency dissemination and synchronization systems over fibre

Research on techniques for stability and synchronized reference frequency dissemination over fibre have already been reported [90-103]. Cliche and Shillue in early 2006 demonstrated three important subsystems of the photonic local oscillator (LO) reference distribution system for the ALMA radio telescope. Subsystems relying on specific control systems that could allow ordinary components to be assembled to form a more accurate and stable global system than its individual components were developed. By using appropriately designed loops, lasers with phase noise of many thousands of rad^2 were phase-locked to generate high-purity frequency signals with phase noise below 3.3×10^{-5} rad^2 at 27 GHz. Moreover, fibres with lengths fluctuating by more than a few millimeters were compensated within a fraction of a micrometer, and optical frequencies of lasers normally fluctuating by tens of megahertz were stabilized to within a few kilohertz. This work demonstrated how control systems could be used with photonic and electronic systems to achieve remarkable stability results [104].

In 2008, Jungwon Kim *et al*. used an ultralow-noise optical pulse trains generator from a mode-locked laser as timing signals, then distributed them by means of timing-stabilized fibre links. This group synchronized the delivered timing signals with high precision. They managed to demonstrate for the first time that remotely located lasers and frequency sources could be synchronized with less than 10 fs precision over more than 10 hrs. This drift-free operation was an important milestone in transitioning mode-locked laser-based synchronization from the laboratory into real-world facilities [101].

Ken G *et al*. in 2012 proposed and experimentally demonstrated a two optical fibre-based radio frequency signal distribution system based on an analogue and all-digital electronics. The group achieved a fractional frequency transfer stability of 6×10^{-17} over 104 seconds for analogue using a 20 Km fibre spool [105]. In 2013, Dong Hou *et al*. presented a fibre-based radio frequency signal distribution system. In their approach, they used a hybrid technique in which digital signal processing was combined with analogue electronic architectures to effectively reduce the fibre-induced phase noise and ensured high-accuracy frequency distributions. Their approach entailed a digital signal processing module for active phase fluctuation analysis and a resistance-capacitance microwave phase shifter for the noise suppression. Their proposed system achieved a fractional frequency transfer stability of 3×10^{-14} at 1 sec and 8×10^{-17} at 50,000 sec over a 22 Km outdoor fibre link. Their system was easy to implement and very scalable, with the ability to suppress fibre-induced phase noise by over two orders of magnitude in the long-term [96].

Ning *et al*. in 2014 demonstrated a new high precision timing distribution system by using highly precision phase detector to overcome the limitations from thermal and shot noise from conventional photodiodes and mixers. Instead of using photodiodes and frequency mixers, they used several fibre Sagnac-loop-based optical frequency phase detectors to realize optical-to-electrical conversion and phase measurement, for suppressing the noise and achieving ultra-high accuracy. A 10 Km fibre link distribution was achieved. Their system provided a residual instability at the level of 4×10^{-15} at 1 sec and 6.1×10^{-15} at 10,000 sec with an integrated timing jitter as low as 3.8 fs in a bandwidth of 1 Hz to 100 KHz. This low instability and timing jitter meant that their system could be used in the optical clock distribution applications for facilities requiring extremely accuracy frequency time synchronization [100]. In the same year, the group further demonstrated using their proposed several fibre Sagnac-loop-based optical frequency phase detectors (OM-PDs) to achieve optical-to-electrical conversion and phase measurement, thereby suppressing the sources of noise and achieving ultra-high accuracy. The results of a distribution experiment using a 10 Km fibre link indicated that their system exhibited a residual instability of 2.0×10^{-15} at 1 sec and 8.8×10^{-19} at 40,000 sec and an integrated timing jitter as low as 3.8 fs in a bandwidth of 1 Hz to 100 KHz [99].

In 2015, Lukasz Sliwczynski *et al*. presented results of their work concerning the long range fibre optic dissemination of time (1 PPS) and frequency (10 MHz) signals generated by atomic sources (cesium clocks, hydrogen masers or Cesium fountains). They developed a fibre optic system with active stabilization of the propagation delay and bidirectional fibre optic amplifiers together with a procedure to enable calibration of the time transfer. A 480 Km fibre length was achieved and an Allan deviation of the order of 4×10^{-17} at 1 sec attained at one-day averaging. After a successful laboratory evaluation, the system was next installed on a 421.4 Km long route between the central office of measures (GUM) in Warsaw, Poland, and the Astrogeodynamic observatory (AOS) in Borowiec near Poznań, Poland. The field operation of the system proved its full functionality and confirmed their previous laboratory evaluation to the maximum extent possible using the methods for comparing distant clocks available at GUM and AOS [92].

Lopez *et al*. in 2016 reported on RF frequency transfer over an urban 86 Km fibre with a resolution of 2×10^{-18} at one day measuring time using an optical compensator. Their results were obtained with a reference carrier frequency of 1 GHz, and a rapid scrambling of the polarization state of the input light in order to reduce the sensitivity to the polarization mode dispersion in the fibre. They further reported on a preliminary test of an extended compensated link over 186 Km using optical amplifiers and attained resolution below10^{-17} at 1 day measuring time.

In early 2017, Cecilia *et al*. developed an ultimate VLBI system to disseminate the highest precision ever reported state-of-the-art atomic clock. In this work, a narrow line width 1550 nm laser phase locked to a hydrogen maser using an optical frequency combo was used to deliver a 100 MHz clock reference from a national metrology institute to a radio telescope using a coherent fibre link 550 Km long. Uncertainty of the delivered frequency at the 10^{-19} level of precision was attained [103].

Shanglin Li *et al*. from Peking University, Beijing China have recently reported on a method for frequency dissemination system over fibre by directly evaluating the radio frequency transfer quality via fibre links at the remote site. In their approach, the radio frequency signal was amplitude modulated on continuous wave lasers with two wavelengths at the local site, multiplexed and disseminated to remote sites. At the remote site, the RF signal was detected from the continuous-wave optical carrier and transfer performance evaluated by measuring the phase fluctuation difference between two different RF signals. This approach greatly simplified the structure of the frequency dissemination link, like in an antenna array system because the remote signal does not necessarily need to be sent back to the local site [90, 106].

A summary of reference frequency distribution experiments is shown in table 3.1.

Table 3.1: Reference frequency distribution experiments

Reference	RF clock frequency distributed	RF clock stability achieved	Distribution distance attained
[90]	150 MHz	3.3×10^{-5} rad^2 at 27 GHz	1100 km
[92]	1 PPS and 10 MHz signals	4×10^{-17} time deviation below 1 ps	421.4 km
[93]	40 MHz	2×10^{-18} at 30 000 sec averaging time	540 km
[94]	774 MHz	7×10^{-15} for a 1sec averaging time	6.9 km round trip
[95]	1 GHz	2×10^{-8} at one day measuring time	86 km
[96]	143 MHz	3×10^{-14} at 1 sec and 8×10^{-17} at 5×10^{4} sec	22 km
[99]	6 GHz	2.0×10^{-15} at 1 sec and 8.8×10^{-19} at 40000 sec	10 km
[103]	10 MHz and 5 MHz	3×10^{-16} and 1×10^{-15} in few hours	550 km

3.2 Clock stability measurement techniques

Several techniques measuring frequency fluctuations in precision oscillators have been proposed [107]. The choice of a particulate technique is dictated by its precision, type of oscillator wave, complexity and its resolution [108]. The first technique is the heterodyne frequency measuring method or the beat frequency method [107, 109]. This method is commonly used to measure square wave of beat signals. The precision of this method is dependent on the detection of up- crossing point. Depending on the frequency counter accuracy, this method provides high precision. However, it is slow and expensive to implement. A full description of heterodyne frequency measuring method is given in [109].

The dual-mixer time difference (DMTD) system technique uses two heterodyne measurement operation simultaneously [110]. The time difference of the zero crossings of each beat frequency is then measured and this technique yields a very high precision. A block diagram of this method is shown in [106]. The high precision of this technique makes it possible to measure time fluctuations as well as frequency fluctuation for shorter time samples. Some experimental works employing this technique has already been reported [111-114].

The loose-phase locked loop method (PLL) is utilized by most signal source analyzers, such as measurement instruments designed for phase noise measurement [115]. In this method, a signal from an oscillator under test is fed into one port of the mixer. The signal from a reference oscillator is fed into the other port of this mixer. The signals are in quadrature so that the average voltage out of the new mixer is zero, and the instantaneous voltage fluctuations corresponds to phase fluctuation between the two signals rather than their amplitude fluctuations. This technique has the advantage of ability to separate phase noise from amplitude noise, carrier suppression thus small offsets can be measured and ability to do phase noise measurement to large offsets even for strongly drifting carriers. However, it is limited by its complexity in setting and calibration. An in-depth description of other commonly used clock stability measurement technique is given in [116, 117].

3.3 Allan variance

Time and frequency metrology provides some of the most accurate measurement ever. Over the last decade, a large number of papers dealing with the statistics of atomic time and frequency standards have been published [33, 118-123] The Allan variance or 2-sample variance is a measure for the stability of an oscillator. It is formed by the average of the squared differences between successive values of a regularly measured quantity taken over sampling periods from the measuring interval up to half the maximum measurement time [124]. For N measurement of values y_i at interval τ_0, the Allan variance is given as [108, 124];

$$\sigma_y^2(\tau_0) = \frac{\sum_{i=1}^{N-1}\left(y_{i+1} - y_y\right)}{2(N-1)} \qquad 3.1$$

The standard variance of the same measurement values is

$$\sigma^2 = \frac{\sum_{i-1}^{N}(y_i - \bar{y})^2}{N-1} = \frac{1}{(N-1)}\left[\sum_{i-1}^{N} y_i^2 - \frac{1}{N}\left(\sum_{i=1}^{N} y_i\right)^2\right] \qquad 3.2$$

Taking any adjacent pair of measurement, N = 2 and the numerator for the Allan variance is

$$(y_{i+1} - y_i)^2 = y_{i+1}^2 - 2y_i y_{i+1} + y_i^2 \qquad 3.3$$

and the numerator of the standard variance is

$$y^2 + y_{i+1}^2 - \frac{1}{2}(y_i + y_{i+1})^2 = \frac{1}{2}(y_{i+1}^2 - 2y_i y_{i+1} + y_i^2) \qquad 3.4$$

The dependence of the Allan variance on time interval within the measurement set can be found by averaging n adjacent values of y_i . Then for $\tau = n\tau_0$ this can be expressed as [108];

$$\sigma_y^2(\tau) = \frac{1}{2(N - 2n + 1)\tau^2} \sum_{i=1}^{N-2n+1} (y_{i+2n} - 2y_{i+n} + y_i)^2 \qquad 3.5$$

A Fourier transform of process steps in forming the Allan variance from data variability measurement in frequency domain is derived explicitly in [125].

In this chapter, State-of-the-Art frequency dissemination and synchronisation systems have been presented. A review of precisely stable reference frequency dissemination and synchronisation systems has been reported. Reference clock stability measurement techniques have also been discussed. The next chapter presents high capacity data transmission techniques exploiting VCSEL technology. This includes, advanced modulation formats for VCSEL-based links as well as fibre impairments in optical fibre communication links.

Chapter 4

High capacity data transmission techniques

4.1 High-speed VCSEL technology

A vertical cavity surface emitting laser (VCSEL) was invented in 1977 [126, 127] by Prof. Emeritus K Iga of Tokyo institute of technology. The first lasing operation [128, 129] and low threshold operation with micro cavity [130] were obtained in 1979 and in 1987, respectively. Since then, these laser sources have continuously attracted much attention both in industry and in research [131-140]. This is due to their unique features such as low power consumption, high-speed modulation with low drive currents, wavelength tuneability thus allowing for integration in WDM systems, large scale two dimension array, narrow circular beam for direct fibre coupling, low cost and small packaging, single longitudinal mode operation with vertical micro cavity, on wafer wavelength control and wafer level testing for low cost manufacturing [133, 141-146].

Gigabit Ethernets and fibre channels are currently major markets for VCSELs [137, 138]. Moreover, long wavelength VCSELs emitting at 1200-1330 nm and 1550 nm are commercially available for use in single mode fibre metropolitan area and wide area networks [144, 147-151]. 10 G Ethernet modules are now readily available for practical systems. Consequently, commercial 850 nm VCSELs have been well established for short reach applications. Majority of high-speed short-range optical links are implemented in the data centres. They have to be high-speed, densely packaged, and energy efficient [152-155].

There are several new standards that cover high-speed VCSEL links. IEEE 802.3bm aims at supporting 100 Gbps (4x25) using non return to zero (NRZ) [156]. Infiniband EDR suggests 1, 2, or 12 parallel lanes with 25 Gbps in each [157, 158]. Fibre channel 32GFC requires transceivers at 28 Gbps supporting 100 m [159]. VCSELs are also used as low-rate, low-cost antenna links. They feed the signal from a cell cabinet to the antenna. Antenna link capacities are standardized by LTE standard, i.e. the 43rd band of the LTE standard is defined as 1 Gbps at a 3.7 GHz carrier. In future, radio over fibre (RoF) systems will use higher carrier frequencies (starting with 5 GHz) to increase capacity [160].

4.1.1 VCSEL structure

Fig 4.1 shows an example of a single mode VCSEL structure. The structure has two electrical contacts: p-contact and n-contact as shown in fig 4.1. The active region is in between two distributed Bragg reflectors (top DBR and bottom DBR). DBRs are highly reflective mirrors used for current injection [161]. The mirrors provide optical feedback while the active region provides gain [133].

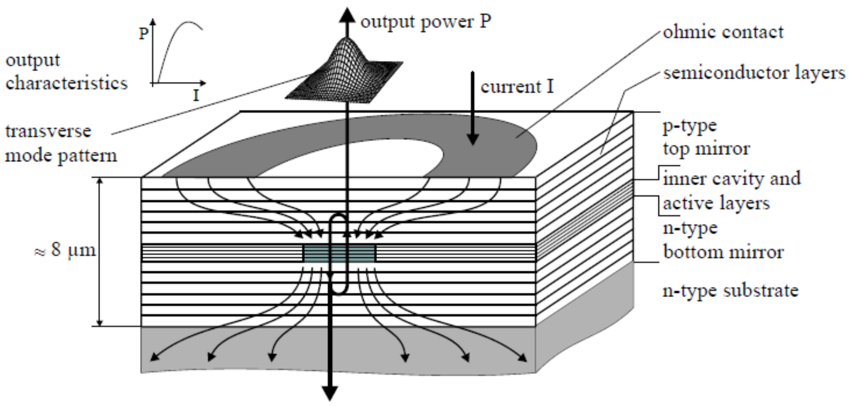

Fig 4.1: Schematic layer structure and operation principle of a VCSEL [133].

They include interchanging high and low refractive index layers where the light is partially reflected at each interface. Layers closest to the active region have a lower refractive index than that of the active region. DBRs vertically. The active region must provide gain sufficient to overcome optical losses in the medium and also sufficient power for lasing. It also consists of a Quantum well (QW) [162]. The carriers in QW are confined to one dimension and free in two other dimensions due to the quantum confinement effect [163]. Carriers are '*trapped'* in the lowest conduction and valence band states, and separated from each other by higher band states. This provides high carrier density. Typically, a VCSEL structure features multiple QWs to provide sufficient gain. The oxide layer is added in the structure to confine both optical modes and current in the transverse direction. The confinement current and modes are guided to the active region [164]. The cavity length of high-speed VCSELs is usually designed to be the shortest possible to increase the modulation bandwidth [133, 165].

4.1.2 Rate equations

The characteristic behavior of carriers and photons in semiconductor laser cavity can be described using a reservoir model as described in [166]. The reservoir model describes the intrinsic characteristic dynamics of semiconductor laser. According to the model, there are two reservoirs in the active region. The model describes that the number of carriers in the reservoir increases by $\frac{\eta_i I}{q}$ during laser current injection, where η_i is the current injection efficiency and $\frac{I}{q}$ is the number of carriers injected to the laser. The number of carriers decreases as a result of non-radiative recombination at the rate $R_{nr}V$, spontaneous emission recombination at the rate $R_{sp}V$ and stimulated emission recombination at the rate $R_{21}V$. The carrier number rate equation summarizes these processes in the carrier reservoir:

$$V\frac{dN}{dt} = \frac{\eta_i}{q} - \left(R_{sp} + R_{nr}\right)V - \left(R_{21} - R_{12}\right)V \qquad 4.1$$

The number of photons in the photon reservoir therefore increases due to stimulated emission recombination at the rate $R_{21}V$, and spontaneous emission at the rate $R_{sp}V$. The number of photons also decreases due to the photon absorption at the rate $R_{12}V$ and due to light emission. Photons escape the laser cavity at the rate $\frac{N_p V_p}{\tau_p}$ where τ_p is the photon life time. The photon rate equation summarizes processes in the photon reservoir:

$$V_p\frac{dN_p}{dt} = \left(R_{21} + R_{12}\right)V - \frac{N_p V_p}{\tau_p} + R'_{sp}V \qquad 4.2$$

Dividing equation 4.1 and 4.2 by carrier reservoir volume size V and replacing the terms $R_{21} - R_{12}$ by $v_g g N_p$ results in density rate equations;

$$\frac{dN}{dt} = \frac{\eta_i I}{qV} - \left(R_{sp} + R_{nr}\right) - v_g \alpha_r g N_p \qquad 4.3$$

$$\frac{dN}{dt} = \left(\alpha v_g \alpha_r g - \frac{1}{\tau_p} \right) N_p + \alpha R'_{sp} \qquad 4.4$$

Where $\alpha = \frac{V}{V_p}$ is the confinement factor, v_g is the group velocity, τ_p photon lifetime, N number density, N_p photon density, η_i internal quantum efficiency, V active region volume, q electric charge, $R_{sp} = \frac{N}{\tau}$ spontaneous emission rate, R_{nr} non-radiative recombination rate and R'_{sp} rate of photons emitted into mode of interest.

Optimization of parameters in the rate equation of semiconductor lasers are important in fitting laser models to the measured behavior. These parameters are vital in laser performance evaluation for ideal modulation.

4.1.3 Frequency response

The frequency response of laser (scattering parameter) can be measured using the small signal analysis. Photons are created as a result of stimulated emission. An in depth analysis of laser transfer function has been derived in [166], from the rate equation for photon and carriers density (equation 4.3 and equation 4.4) and has the form of a second order damped system as shown in equation 4.5

$$H_L(\omega) = \frac{\omega^2{}_r}{\omega_r^2 - \omega^2 + j\omega\gamma} \qquad 4.5$$

Where H_L is transient function of the laser, $\omega_r = 2\pi f_r$ and γ is the damping factor. Equation 4.5 describes the VCSEL frequency response considering only intrinsic effects of the laser. However, at high frequencies, VCSELs have parasitic resistance and capacitances that can reduce the modulation response. Moreover, additional poles need to be added to the equation to describe the extrinsic effects that include parasitic response [167]. These effects vary for different lasers and have to be defined separately based on the device design and electrical contact circuit as discussed in [166].

4.1.4 Static characterization

The operation range of most semiconductor lasers can be defined based on the laser's DC characterization. Injected carriers are utilized for spontaneous emission and non-radiative recombination under the small, below threshold, current condition. Under this current condition, the output is mainly as a result of spontaneous emission. Stimulated emission recombination only occurs when the number of injected carriers exceeds the spontaneous and non-radiative losses. The threshold I_{th} is the current level at which stimulated emission starts occurring. For currents higher than I_{th} carriers are mostly in the stimulated emission therefore the output power increases linearly with applied current. The steady state solution of the rate equations is used to describe the output power P_0 in the linear range as a function of the bias current [133]:

$$P_0 = \eta_d \frac{h\nu}{q}\left(I - I_{th}\right) \qquad 4.6$$

Where η_d is the quantum efficiency, $h\nu$ is the energy of photon and q is the elementary charge. From equation 4.6, the laser output power saturates towards higher bias current values due to thermal effects on the laser. DC characteristics allow choosing an optimum bias current for ideal modulation of the laser module. The perfect choice of ideal bias current is therefore in the middle of the linear range.

4.1.5 Optical spectrum

An optical spectrum is the optical power distribution over different wavelengths of a laser. The laser emission wavelength can be measured using an optical spectrum analyser (OSA). For VCSEL lasers, the emission wavelength increases with increase in bias current as a result of internal cavity heating [133, 165]. The spectral width of lasers is standardized using a root mean square (RMS) deviation. For single mode VCSELs, the RMS spectral width ranges up to 0.443 nm as reported in [168], while for multimode VCSELs the RMS spectral width ranges up to 1.04 nm [142, 168] due to multiple transverse modes. An increased laser spectral width makes it vulnerable to chromatic dispersion effects within the fibre. This therefore limits the maximum transmission reach as well as degrades the signal integrity. Fibre related effects will further be addressed in section 4.7.

4.2 Advanced modulation formats for VCSEL-based links

Fibre optic communication systems form the high capacity transport infrastructure that enables global broadband data services. The desire for higher per-fibre transport capacities and, at the same time, the drive for lower costs per end-to-end transmitted information bit has led to optical networks with high spectral efficiencies [169]. Among other enabling technologies, advanced optical modulation formats have become key to the design of modern fibre transmission systems [132, 169-172]. In this section, optical modulation formats in the broader context of spectral efficiencies in IM/DD VCSEL-based network links are presented.

4.2.1 State-of-the-art

To fulfil demands for developing ultrafast optical transmitters to solve the heavy data traffics in modern communication systems as standardized by IEEE P802.bs [156], the transmission capacity of laser diode modules have been up-scaled from 100 Gbps/module to 400 Gbps/module for applications such as cloud data centres based on the use of 8-channel VCSEL array transmitter with 50 Gbps channel capacity [173]. The IEEE 802.3bs 400 Gb/s Ethernet task force has worked on industry standards for intra-data centre interconnects with link distances of 500 m, 2 Km, and 10 Km over standard single mode fiber (SSMF). Intensity modulation and direct detection (IM/DD) links are preferred for its low cost and simplicity. Experimental demonstrations of e.g. 4×100 Gbps discrete multi-tone (DMT) signal transmission over 4 Km SSMF [174] and 2×56 Gbps 4-PAM signal over 10 Km SSMF [175] have been performed using offline digital signal processing (DSP). It has been shown that 56 Gbps IM/DD DMT on 8 channels can successfully bridge 240 Km of SMF [15]. However, all these demonstrations utilized offline DSP. Real-time PAM-4 transmission at 25 GBaud and at 56 GBaud has been demonstrated only for a single channel over up to 10 Km and 2 Km SMF, respectively and at high OSNR [176, 177].

At current stage, adoption of directly modulated VCSEL links in big data networks such as data centres has emerged as a cost-effective solution [139, 178, 179]. The well-known advantages of such links make VCSELs irreplaceable candidates for the aforementioned applications [180-182]. However, the allowable transmission data rate or distance is still limited by both the direct modulation bandwidth, and the inevitable chromatic dispersion in the transmission fibre [183]. In view of previous works with VCSELs, Chongjin, *et al*. in

2013 successfully implemented a 3-PAM 1550 nm VCSEL coherent transmission link at 105.7 Gbps over 960 Km SMF with FEC threshold at a BER of $1.5\text{x}10^{-2}$ [184]. Tan *et al* designed a photonic crystal structure to achieve single mode emission in the VCSEL transmitter for 25 Gbps data over 1Km in 2013 [185]. In 2014, Safaisini *et al*. integrated a mode filter generated with surface relief to realize a SM VCSEL transmitter for delivering 20 Gbps data through a 2 Km link [186]. In the same year, Chongjin, *et al* reported on a 400 Gbps polarization division multiplexed (PDM) and WDM 4-PAM using 2x4 PDM/WDM monolithic VCSEL array and successfully transmitted over 400 Km of standard single mode fibre using digital coherent detection [187].

For practical application, several studies of the VCSEL with various data formats for high data rate links such as intra-data center networks have also been illustrated. Recently, Kuchta *et al*. used VCSEL to carry non-return-to-zero on-off-keying (NRZ-OOK) data at 71 Gbps over 7 m [188]. A comparison of MM, FM and SM VCSELs on carrying NRZ-OOK data format for back-to-back transmission was reported in [189]. However, the low spectral usage efficiency of the NRZ-OOK makes the VCSEL require large modulation bandwidth for encoding [190]. To achieve the same data rate, 4-PAM data is an alternative approach for decoding the VCSEL, since it only needs half of modulation bandwidth when comparing with NRZ-OOK data [191, 192]. In 2016, encoding PAM-4 onto an unpackaged VCSEL to achieve 100 Gbps over 100 m with a pre-emphasis filter technology was proposed [193]. Therein the pre-emphasis filter is a digital filter embedded in the arbitrary waveform generator (AWG), which can pre-distort the transmitted signal to compensate the signal degradation during channel transmission for improving the transmission performance. In 2017, Kottke *et al*. recently demonstrated a DMT link over 500 m MMF at the rate up to 135 Gbps by using an 850 nm VCSEL with the assistance of the Volterra based pre-equalizer [194]. A summary of state-of-the-art VCSEL-based transmission experiments is shown in table 4.1.

Table 4.1: Summary of transmission experiments with VCSELs.

Reference	Bit rate achieved/ λ	Modulation format used	Detection technique	Distance attained	Transmission Wavelength
[195]	25 Gbps	OOK	DD	4.2 Km SMF	1550 nm

[184]	88 Gbps	3-PAM	Coherent	960 Km SMF	1550 nm
[187]	100 Gbps	4-PAM	Coherent	400 Km SMF	1550 nm
[196]	100 Gbps	DMT	DD	4 Km SMF	1550 nm
[197]	100 Gbps	4-PAM	DD	100 m SMF	1550 nm
[198]	56 Gbps	4-PAM	DD	2 Km SMF	1550 nm
[199]	50 Gbps	4-PAM	Equalization and FEC	100 Km SMF	1550 nm
[135]	28 Gbps	OOK	DD	500 m MMF	1060 nm
[62]	50 Gbps	4-PAM	DD	200 m MMF	1060 nm
[200]	30 Gbps	4-PAM	DD	200 m MMF	850 nm
[201]	40 Gbps	OOK	DD	3 m MMF	850 nm
[141]	40 Gbps	OOK	DD	B2B	850 nm
[202]	56 Gbps	DMT	DD	100 m MMF	850 nm
[203]	60 Gbps	4-PAM	DD	2 m MMF	850 nm
[181]	64 Gbps	OOK	DD	57 m MMF	850 nm
[204]	70 Gbps	4-PAM	DD	50 m MMF	850 nm
[205]	44 Gbps	OOK	DD	2 m MMF	980 nm
This work chapter 4 [151, 206]	10 Gbps	NRZ	DD	24.75 Km SMF	1550 nm
This work chapter 6 [207]	Simultaneous 10 Gbps and Polarization-based PPS clock signal	DM and polarization modulation	DD with DSP assisted receiver	11 Km SMF	1310 nm

4.3 Intensity modulation with direct detection

In high-speed optical fibre communication, intensity modulation (IM) using directly modulated lasers (DMLs) with direct detection (DD) is the most preferred modulation/demodulation technique due to its simplicity and effectiveness. These two processes take place in a laser and a photodiode (PD), respectively. As the transmitted electrical data is superimposed to the laser bias current, the variation of the current driving the laser directly modulates the output power of the laser. The simplest way to produce intensity modulated signal is shown in fig 4.2 [208].

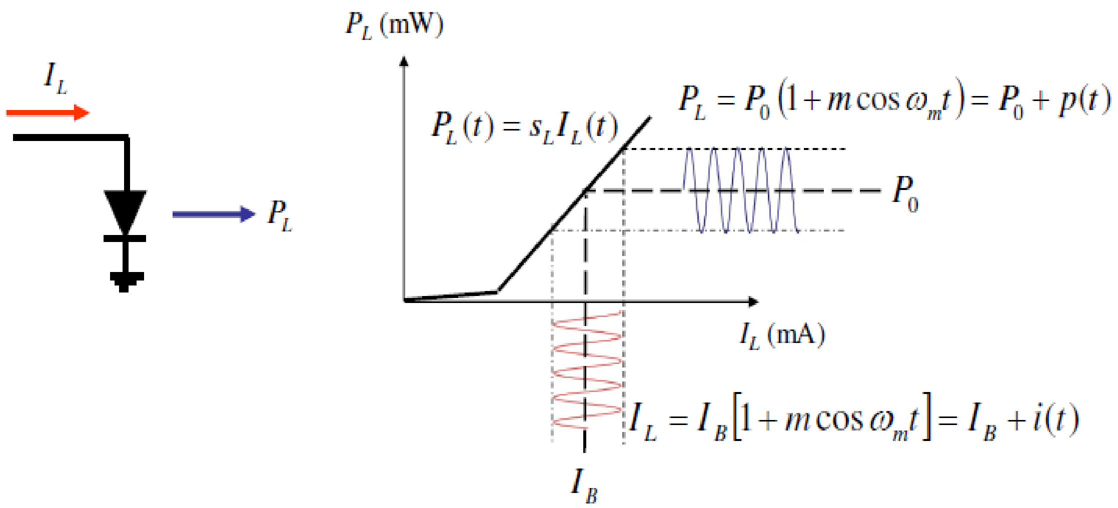

Fig 4.2: Intensity modulated signal using a DML [209].

At the PD, intensity of optical wave is converted to electrical current based on square-law detection of the PD. IM also can be done using external modulators. A laser emits continuous wave (CW) light and the modulation is done afterwards by an external optical modulator [210]. Electro-absorption modulator (EAM) and Mach-Zehnder modulator (MZM) are two external modulators commonly used today in optical communication systems. External modulators offer much higher modulation bandwidth (up to 60 GHz) than DMLs. This is due to the independence between light generation and modulation thus providing better signal quality. A MZM-based IQ modulator can be used to generated advanced modulation formats such as quadrature phase shift keying (QPSK). However, as an additional device is required, external modulation results in a more expensive system. The applications of different modulation methods and optical modulators is presented in Fig 4.3 [209].

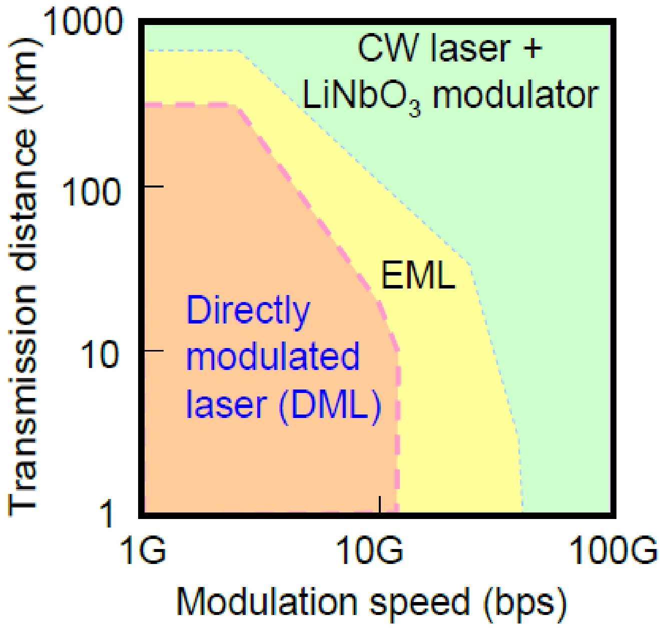

Fig 4.3: Transmitters for optical fibre communication links [209].

For short-range and access networks, due to strict requirement for the cost of the whole system, intensity modulation using a DML such as distributed feedback laser (DFB) or VCSELs is preferred.

4.4 Non-return-to-zero (NRZ)

Non-return-to-zero (NRZ) is a two dimensional modulation technique that carries one bit per symbol and has two signal levels ('0' level and '1' level). Currently, it is the most preferred modulation format used in commercially available transceivers. Its implementation is simple and therefore power efficient. The capacity of the NRZ links has grown through the recent years with the increasingly improved VCSEL structures and, therefore, their higher bandwidths. However, the achievable distance for the high-speed VCSELs is limited by the fibre bandwidth. This is due to combined effects of VCSEL's intrinsic or extrinsic behavior and chromatic dispersion [211]. The highest reported bitrates with NRZ modulation are 71 Gbps and 60 Gbps [211, 212] using MMF over 7 m and 100 m fibre lengths respectively. Part of this PhD project utilized the NRZ modulation format [150, 151, 206, 207].

4.5 Four level pulse amplitude modulation (4-PAM)

Different advanced modulation techniques have been proposed for application in high speed optical communication systems [169-172]. They can be multi-level and multi-dimensional. The most popular one is Pulse amplitude modulation (PAM) e.g. 4-PAM, 8-PAM. In PAM systems, multiple amplitude levels are used. For instance, in 4-PAM, four levels are utilized thus doubling the capacity of the link as opposed to the one-dimensional NRZ. A summary of state-of-the-art 4-PAM short-range transmission experiments as reported in literature is shown in table 4.2.

Table 4.2: State-of-the-art 4-PAM advanced modulation formats applied in high-speed optical communication links.

Reference	Data rate	Format	DSP (Tx/Rx)	Distance
[198]	56 Gbps	4-PAM	None/FFE and MLSE	2 Km
[213]	56 Gbps	4-PAM	4-tap FFE/none	B2B
[214]	56 Gbps	4-PAM	3-tap FFE/21-tap FFE	15 Km
[214]	84 Gbps	4-PAM	3-tap FFE/21-tap FFE	1 Km
[215]	84 Gbps	4-PAM	3-tap FFE/FFE, NLVE & MLSE	1.6 Km
[198]	56 Gbps	4-PAM	DD	2 Km
[199]	50 Gbps	4-PAM	Equalization and FEC	100 Km
[187]	100 Gbps	4-PAM	Coherent	400 Km

This work chapter 8 [216]	20 Gbps	4-PAM	DSP assisted receiver	3.21 Km SMF
This work chapter 8 [217]	Simultaneous 20 Gbps data and 2 GHz RF clock signal	4-PAM and phase modulation	DSP assisted receiver	B2B
This work chapter 8 [218]	Simultaneous 20 Gbps data and 2 GHz RF clock signal	4-PAM and phase modulation	DSP assisted receiver	3.21 Km SMF
This work chapter 8 [217]	Simultaneous 20 Gbps data and polarization PPS clock signal	4-PAM and polarization modulation	DSP assisted receiver	3.21 Km SMF

- MLSE = maximum likelihood sequence estimation
- NLVE = nonlinear Volterra equalizer

4.5.1 Realization of 4-PAM

The limited bandwidth of NRZ links led to high capacity short-range communication community to focus on advanced modulation formats to support higher bit rates. 4-PAM doubles the network capacity compared to NRZ with the same bandwidth. It is the least complex of the advanced modulation schemes. 4-PAM has four amplitude levels. Two additional voltage levels are introduced in between the maximum and minimum levels of the NRZ. This results in reduced spacing between the levels and the twofold increase of the signal capacity. Grey coding, which has 1 bit difference between adjacent levels, is typically used to encode 4-PAM signals. A possibly simple ways to realize 4-PAM is to couple together two de-correlated binary signals, one of them attenuated. 4-PAM demodulation is achieved by decoding the signal amplitude, and using three decision thresholds to distinguish the symbols. A full demonstration of 4-PAM signals modulation/demodulation and derivation of all associated equations is demonstrated in our contribution in [218, 219]. All 4-PAM implementation examples presented in table 4.2 required the FEC overhead and equalization. However our 4-PAM modulation approach in chapter 8 and other subsequent chapters is simple to implement as it does not use energy consuming and complex FEC overhead circuits and equalization mechanisms.

The main advantage of 4-PAM modulation technique is the doubled spectral efficiency as compared to NRZ. 4-PAM also reduces the bandwidth requirement and potentially extends the maximum attainable reach over fibre. However, 4-PAM modulation formats are limited by tripled requirement on SNR that comes with closer spaced levels. This, in turn, puts a more stringent requirement on VCSEL's RIN and other noise sources in the transmission link. With an increased number of levels, the ISI penalty also increases together with the eye closure penalty [204, 220, 221]. This therefore calls for 4-PAM transceivers to incorporate FEC and equalization circuits, thus more complexity and energy consuming as opposed to NRZ transceivers [146].

4.6 VCSEL polarization modulation

A unique feature that differentiates VCSELs from conventional edge emitting semiconductor lasers is their polarization characteristics [222-229]. VCSELs usually emit linearly polarized light oriented in a specific crystallographic direction due to their cylindrical symmetry, direction of lasing, and carrier injection. The carrier injection is always perpendicular to the active layer and along the axis of cylindrical symmetry. However, during the VCSEL's manufacturing process, some inherent birefringence caused by stresses unintentionally induced my lead to polarization dependency [222]. Effective control of VCSEL's polarization property is a necessity if it is to be used in polarization sensitive applications such as coherent detection systems and magneto-optic recording [133, 223, 229]. The difference in a VCSEL's geometry can also lead to polarization of emitted laser light that is not well balanced. Polarization dependency in VCSELs has been studied particularly in applications where well-stabilized polarization is required [230-233]. The linear polarized light emitted from VCSEL laser has been observed to switch between two orthogonal states [224, 225, 234, 235]. Mechanisms leading to polarization switching in VCSELs have been reported [226, 227]. Different models to attain VCSEL polarization switching for polarization modulation have been proposed and associated derivative equations expressed explicitly in [207, 222, 223, 225-232, 234-238].

VCSEL polarization switching was exploited to realize the first ever reported simultaneous transmission of directly modulated data signal and polarization-based pulse-per-second (PPS) clock signal as reported in chapter 6 and in chapter 9. A single mode 10 GHz bandwidth VCSEL carrier at 1310 nm was used and a maximum transmission reach of 11 Km of G 652 fibre attained.

4.7 Fibre impairments in optical communication links

Optical signals transmitted over optical fibre medium suffer from fibre impairments, which cause degradation of original signals. These impairments can be divided into linear impairments, and nonlinear impairments [239-242]. When the launched level power into the fibre is moderate (mW range), optical communication systems experience linear effects: attenuation and fibre dispersion. Fibre dispersion includes chromatic dispersion, polarization-mode dispersion (PMD) and modal dispersion. Increasing the launched power can lead to nonlinear effects in the fibre. Nonlinear effects in optical fibres originate from the intensity dependence of the refractive index and stimulated inelastic scattering including self-phase modulation, cross-phase modulation, four-wave mixing, stimulated Raman scattering, and stimulated Brillion scattering. Besides attenuation, fibre dispersion is the most important linear impairment that limits the performance of signals.

4.7.1 Attenuation

The propagation of an optical pulse inside an optical fibre medium suffers from power loss leading to a decreased output power. Attenuation limits the overall transmission distance because of receiver sensitivity, i.e. the minimum power required at the receiver for it to recover the signal correctly. The relationship between the average input power P_{in} and the output power P_{out} of the fibre with length L is governed by Beer's law [243, 244], and is given as:

$$P_{out} = P_{in}.e^{-\alpha L} \qquad 4.1$$

Where α is the attenuation coefficient commonly measured in dB/km. Fig 3.1 shows the loss spectrum $\alpha(\lambda)$ of a single mode fibre (SMF) [244].

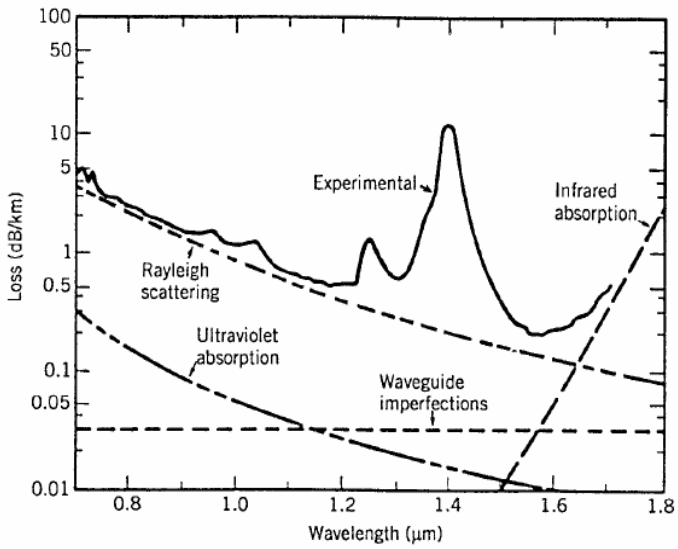

Fig 4.4: Loss spectrum of a single mode fibre (SMF) [244].

The attenuation coefficient depends on the transmitted wavelength, increasing towards the shorter wavelength. A typical attenuation of silica at 1550 nm equals to 0.2 dB/km. The maximum loss for standard SMFs used in today's applications is standardized as about 0.5 dB/km for 1310 nm sources, 0.4 dB/km for 1550 nm sources and 2.89 dB/km for 850 nm sources [245].

4.7.2 Chromatic dispersion in single mode fibres

Chromatic dispersion causes the group velocity of the mode to be frequency dependent. This therefore implies that different spectral pulse component will travel with different group velocities therefore resulting to a pulse spread. This effect is known as chromatic dispersion. Pulse broadening is proportional to the length of the fibre and generates inter-symbol interference (ISI) in time domain at the fibre output. If $\Delta\lambda$ is the spectral width of the pulse, extend of pulse broadening over a fibre of length L is dictated by:

$$\Delta T = \frac{d}{d\lambda}\left(\frac{L}{\upsilon_g}\right)\Delta\lambda = DL\Delta\lambda \qquad 4.2$$

Where

$$\upsilon_g = \left(\frac{d\beta}{d\omega}\right)^{-1}, \text{ and } D = \frac{d}{d\lambda}\left(\frac{1}{\upsilon_g}\right) = -\frac{2\pi c}{\lambda^2}\beta \qquad 4.3$$

υ_g, is the group velocity, D is the dispersion parameter expressed as ps/Km/nm.

4.7.3 Modal dispersion

Multimode fibres (MMFs) experience dispersion effect as a result of chromatic dispersion and modal dispersion. Usually, modal dispersion strongly dominates over chromatic dispersion. The many modes are excited and propagated through the fibre with different propagation delays, which cause modal dispersion. When propagating along the fibre, mode group mixing between mode groups occurs. Each output mode is contributed by all input mode groups [140].

4.7.4 Polarization mode dispersion (PMD)

Optical fibres offer superior performance over their other counterparts. However, polarization effects can affect optical signal performance at higher data rates and/ over longer transmission reach [246, 247]. In single mode fibres the fundamental mode is composed of two orthogonal axis; fast and the slow axis. In a hypothetical scenario, these axises have exactly the same propagation speed therefore no differential delay phenomenon. However, due to birefringence in optical fibres, the two have different propagation velocities therefore resulting to a differential group delay (DGD) [246, 248]. Birefringence results from imperfections within the fibre geometry as well as external mechanical disturbances such as pressure, temperature, bending twisting etc. Fig 4.5 illustrates the fast and the slow axis resulting to DGD due to birefringence for optical fibre with no coupling.

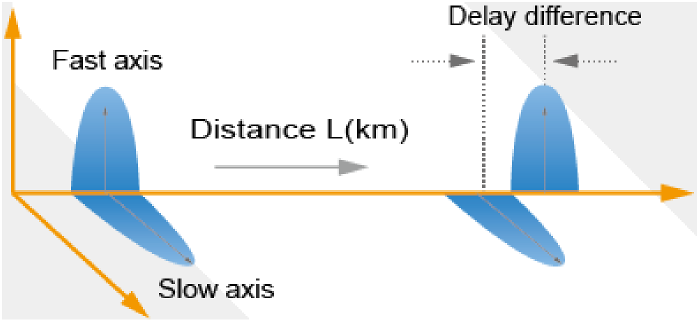

Fig 4.5: Illustration of fast and slow axis due to birefringence and pulse differential group delay (DGD) for optical fibre with no coupling [249].

It should be noted that for real optical fibre network systems, the resultant DGD is proportional to the square root of the total fibre length.

In practice, fibre birefringence varies in both magnitude and orientation randomly along the fibre length. Due to its frequency dependence, fibre birefringence also depolarizes relative states of polarization (SOPs) among optical waves of different frequencies [250, 251]. Burying optical fibre cables is a viable technique to minimize changes in the SOP of the optical signal and therefore limits polarization effects on the transmitted signal.

4.8 Summary

This chapter has presented several high capacity data transmission techniques exploiting VCSEL technology. This included, advanced modulation formats for VCSEL-based links as well as fibre impairments in optical fibre communication links such as attenuation, chromatic dispersion, modal dispersion and polarization mode dispersion. The next chapter begins with experimental demonstration of high-speed vertical cavity surface emitting lasers (VCSELs) in optical fibre networks. Result into simultaneous data and reference frequency (RF) clock signal transmission over a single optical fibre for adoption in next generation telescope array networks are also presented. This chapter ends by drawing the relevance of simultaneous data and reference clock signal transmission over a single optical fibre to telescope array networks.

Chapter 5

Simultaneous data and reference frequency clock signal transmission over one single mode optical fibre line for telescope array networks

This chapter experimentally demonstrates VCSEL technology as an ideal candidate for next-generation high-speed optical communication networks. The use of VCSELs for simultaneous data and reference frequency (RF) clock signal transmission in next-generation telescope array networks is proposed and experimentally demonstrated. We present on the potential of 10 Gbps VCSEL carriers in simultaneous transmission of data and RF clock signal over a single optical fibre for cost effective and reliable next-generation telescope array networks. Performance of the simultaneously transmitted data and RF clock signals are reported using bit-error-ratio (BER) measurement and eye diagram representation for the data signal, and phase noise measurement and jitter analysis curves for RF clock signal respectively. The transmission performance analysis of simultaneously transmitted data and RF clock signal is performed at different channel spacing and different direction of propagation. The relevance of simultaneous data and RF clock signal transmission over a single optical fibre to telescope array networks is presented.

5.1 Vertical cavity surface emitting laser (VCSEL) technology in optical fibre networks

The following subsequent sections demonstrates VCSEL transmission performance for adoption in next-generation high speed optical fibre networks. This is due to their attractive potentials discussed in chapter 4. VCSEL static characterization and optimization for direct data modulation as well as wavelength tuneability for adoption and integration into simultaneous data and reference frequency clock signal transmission over a single optical fibre are experimentally demonstrated.

5.1.1 VCSEL static performance

The static characterization and ability to tune the central emission wavelength of a 10 Gbps VCSEL used in this study was demonstrated experimentally as shown in fig 5.1. A 10 Gbps 1550 nm VCSEL was biased by changing the input current from 0 mA – 9.8 mA, while measuring the respective output optical power (mW).

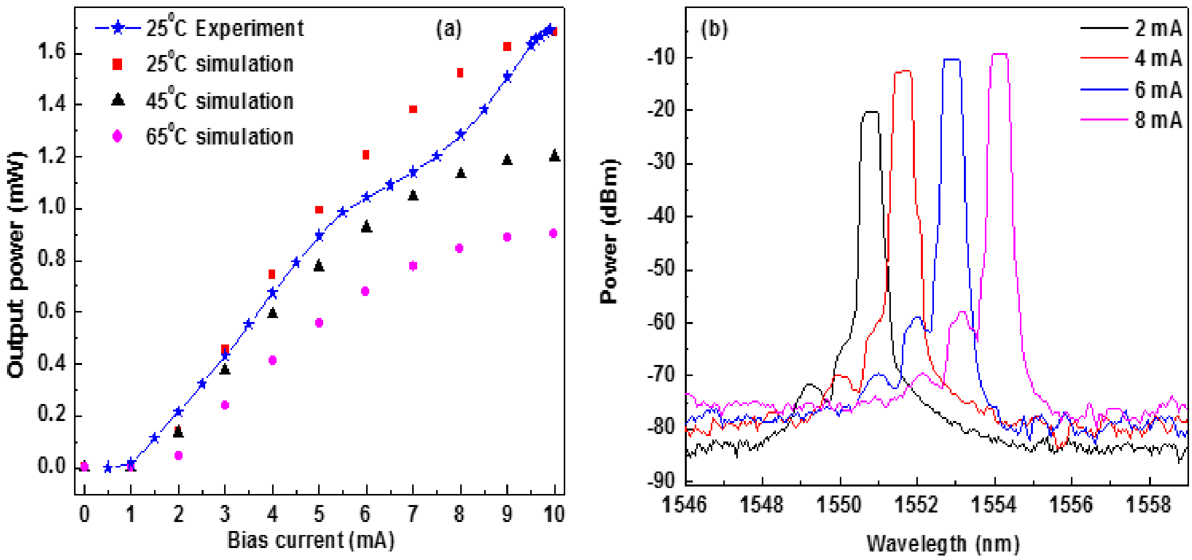

Fig 5.1: Experimentally measured VCSEL static performance, (a) LI characteristics curve, (b) experimentally measured wavelength tuneability.

The experimentally measured output power variation with bias current is shown in fig 5.1(a). From the curve in fig 5.1(a), it was observed that the small volume of the VCSEL resonator allowed for a small threshold current of 1.03 mA. It was also noted that this laser source operated at low drive current range (mA range), a key requirement for power efficient optical fibre networks. This was due to the differential resistance of the VCSEL laser, which is 50 Ω under steady lasing conditions therefore limiting the driving current to remain below 10 mA [252]. The good energy efficiency of the VCSEL together with its small form makes it an ideal candidate for energy sensitive applications such as fibre-to-the-home (FTTH) and densely data centre networks among many other optical applications.

The impact of temperature variation on VCSEL transmitter performance was investigated at different operating temperatures as shown in fig 5.1(a). South Africa weather condition varies from summer to winter [253]. This weather variation is associated with drastic temperature fluctuations, where temperatures might rise to 45^{0} C during summer and drop to almost freezing point during winter [253]. To demonstrate the impact of temperature variation on VCSEL transmission performance of the VCSEL, a VCSEL LI characteristics curve was simulated at different resonator cavity temperatures as shown in fig 5.1(a) using Optisystem software. It was noted that an increase in cavity temperature caused the laser output power to saturate at much lower current level known as thermal rollover current as shown in fig 5.1(a). A thermal rollover current of 8.98 mA, 8.02 mA and 7.24 mA was attained under simulations for 25° C, 45° C and 65° C respectively. It should be noted that a lower thermal rollover current affects the modulation performance of VCSELs. It is therefore, recommended to employ an external cooling mechanism to the device if it is to be used at higher environmental temperature conditions.

VCSEL wavelength tuneability with varying bias current was investigated as shown in fig 5.1(b). A wide bandwidth of approximately. 3.71 nm (from 1550.61 nm to 1554.32 nm) was attained for a 10 Gbps 1550 nm VCSEL used in this study. This was achieved by varying the bias current from 2 mA to 8 mA. The ability of a VCSEL to vary its central emission wavelength with changing bias current provides a great potential for its adoption in wavelength division multiplexing (WDM) applications and in systems where wavelength tuning is required to achieve simultaneous transmission of signals [254, 255]. In this study, the VCSEL wavelength tuneability property was used to attain different channel spacing between the data channel and the RF clock signal channel for simultaneous data and clock signal transmission over a single optical fibre discussed in subsequent sections.

5.1.2 Experimental performance evaluation of VCSEL transmission

Transmission capability of a 10 Gbps 1550 nm high-speed VCSEL was experimentally demonstrated as shown in fig 5.2. A 10 Gbps VCSEL with an emission wavelength of 1552.30 nm at a bias current of 7 mA was modulated with a 10 Gbps pseudorandom binary sequence (PRBS) data signal of pattern length 2^7-1 from a programmable pattern generator (PPG). The VCSEL was biased at 5.54 mA and the RF modulation voltage adjusted to 0.224 V_{RMS} by attenuating the electrical RF signal voltage with 9 dB electrical attenuator for optimum modulation of the VCSEL laser. The modulated data signal was transmitted over a G. 655 single mode reduced slope fibre (SMF-RS) of length 24.75 Km. OFS true wave RS low water peak (LWP) fibre is a non-zero dispersion fibre (NZDF) that provides extraordinary performance for optical transmission systems.

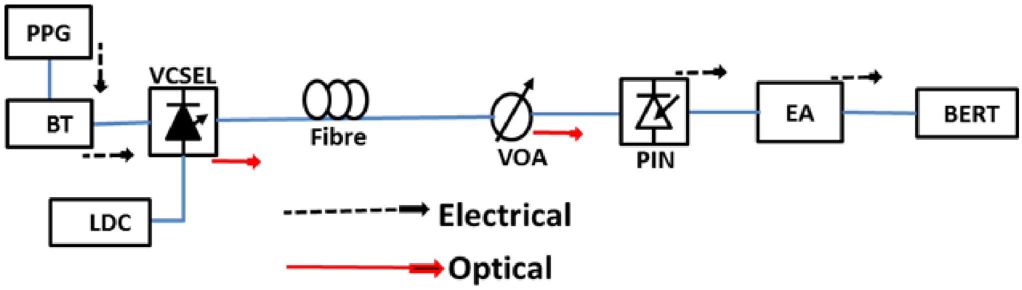

Fig 5.2: VCSEL transmission experimental set-up: PPG-programmable pattern generator, BT-bias tee, LDC-laser diode controller, VOA-variable optical attenuator, PIN-photodiode detector, EA-electrical linear amplifier, BERT-bit-error-ratio tester.

The low dispersion slope of this fibre enables for more uniform performance across the entire C-band (1530 nm – 1565 nm) and L-band (1565 nm – 1625 nm) respectively therefore an ideal fibre for simultaneous data and RF transmission systems [256]. At the receiver end, the optical power getting to the positive intrinsic negative (PIN) photodiode was varied using a variable optical attenuator (VOA). This emulated optical power losses that could be encountered in our proposed optical fibre network.

The measured BER curves for back-to-back (B2B) analysis and 24.75 Km fibre transmission are shown in fig 5.3. A receiver sensitivity of -19.95 dBm was attained experimentally at B2B analysis. After a 24.75 Km fibre transmission, the receiver sensitivity reduced to -19.04 dBm as shown in fig 5.3. This fibre transmission length introduced a transmission penalty of 0.91 dB as shown in fig 5.3.

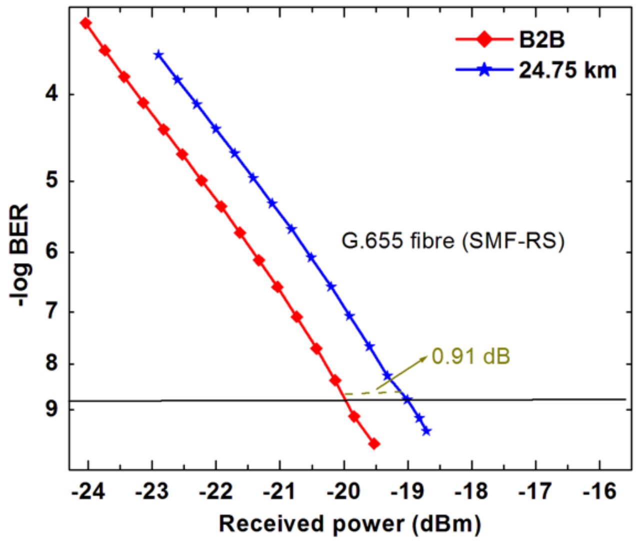

Fig 5.3: Experimental BER curves for 10 Gbps 1550 nm VCSEL transmission on G. 655 fibre of length 24.75 Km.

The respective eye diagrams for back-to-back analysis (red) and 24.75 Km fibre transmission (blue) are shown in fig 5.4. These measurement were collected at a communication threshold of BER=10^{-9}. As seen in fig 5.4, the eye power (in mW) reduced after a fibre transmission. This implied that the eye opening also reduced with a fibre transmission, but remained clearly open at B2B analysis and after 24.75 Km of fibre transmission. A clear, wide and open eye implies a successful error free transmission. This also implies that the PIN receiver could clearly distinguish between the ‘1’ and the ‘0’ bits therefore minimizing bit errors.

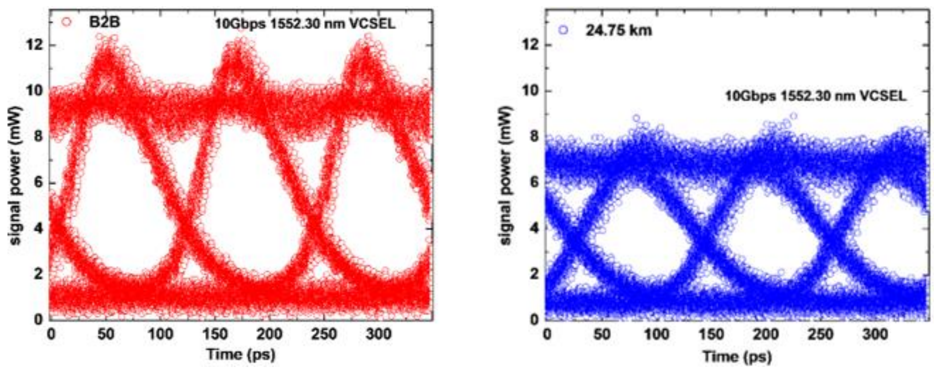

Fig 5.4: Experimentally measured eye diagrams for 10 Gbps 1550 nm VCSEL transmission at back-to-back (red) and 24.75 Km fibre length (blue).

5.2 Experimental demonstration of simultaneous data and reference frequency clock signal transmission over a single optical fibre

Simultaneous data and reference frequency (RF) clock signal transmission over a single optical fibre was experimentally demonstrated at different channel spacing using an array of two VCSELs as shown in fig 5.5. VCSEL 2 was modulated with a 10 Gbps data signal under optimized modulation voltage and biased at 8.60 mA. The emission wavelength of VCSEL 2 was set to 1550.79 nm. The transmission of VCSEL 2 represented the upstream transmission link of the network (from the user end to a central processor center) as shown in fig 5.5. At the central processor center part of the network, a 1.712 GHz (L-band) RF clock signal generated using R&S® SMB100A RF and Microwave signal generator from Rohde & Schwarz company was used to modulate VCSEL 1 with an RF clock signal to make the downstream transmission link of the network as shown in fig 5.5. A suitable RF clock modulation depth was achieved by setting the RF- level of the electrical signal generator to 0.30 mV. Optical isolators were used on both VCSEL transmitters to maintain the optical signal in a forward direction therefore protecting the laser sources from a counter-propagating optical light source. The bias current of VCSEL 1 was varied from 8.25 mA to 8.73 mA to attain different emission wavelengths (1551.18 nm, 1551.38 nm and 1551.58 nm) used in this study.

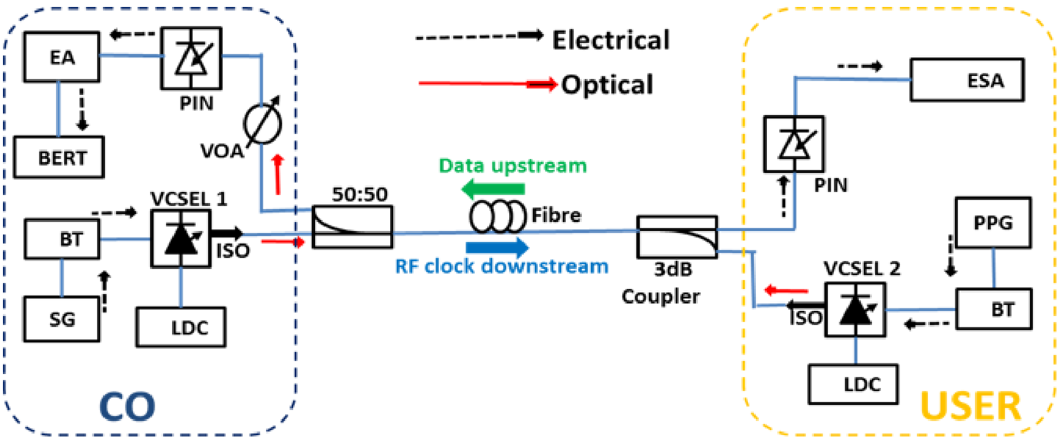

Fig 5.5: Experimental set-up for simultaneous data and reference frequency clock signal transmission over a single optical fibre: PPG-programmable pattern generator, BT-bias tee, LDC-laser diode controller, VOA-variable optical attenuator, PIN-photodiode detector, EA-

electrical linear amplifier, SG-signal generator, ESA-electrical spectrum analyzer, BERT-bit-error-ratio tester.

The two simultaneously transmitted signals (upstream data and downstream RF clock) were coupled onto a single mode fibre of length 24.75 Km using an optical 3 dB coupler. A DSC-R402 10 GHz bandwidth linear PIN-TIA optical receiver with a sensitivity of – 9 dBm was used to simultaneously recover the optical data and RF clock signals for simultaneous analysis. For the data signal, the power getting to the PIN photodiode was varied using a variable optical attenuator and its transmission performance analyzed through BER curve measurement and eye diagram analysis. Consequently, the RF clock signal stability was simultaneously analyzed through phase noise and clock jitter measurement. The effect of simultaneous data and RF clock signal transmission over a single optical fibre was done at 0.4 nm, 0.6 nm and 0.8 nm channel spacing between the data and clock signal respectively.

5.2.1 Experimental analysis of effects of reference frequency clock signal on data transmission at different channel spacing

To study the effect of reference frequency (RF) clock signal on data transmission at different channel spacing as reported in our previous work in [206], two VCSELs transmitting in an opposite direction of propagation were used as shown in fig 5.5. A non-filter based wavelength division multiplexer (WDM) coupler was used to combine the data channel and the RF clock channel to allow for inter-spectrum interaction. The resultant optical spectrum of the inter-channel (data channel and RF clock channel) interaction at different channel spacing is shown in fig 5.6. VCSEL wavelength tuneability with changing bias current was exploited to achieve the different channel spacing.

The data spectrum shown in fig 5.6 (red) was noted to have a distinct spectrum. However, after coupling the data and the RF spectrum channels over a transmission fibre, the resultant spectra were a comprised band overlap of the data and the RF clock spectrum. The spectra overlap was noted to reduce with increase in channel spacing as shown in fig 5.6.

The measured BER curves for VCSEL-based simultaneously 10 Gbps data and 1.712 GHz RF clock signal transmission over a single 24.75 Km of G. 655 SMF-RS fibre transmission is shown in fig 5.7. A receiver sensitivity of -19.26 dBm was attained for the B2B analysis of data signal alone. However, after coupling the data signal with a 1.712 GHz RF clock signal at 0.8 nm, 0.6 nm and 0.4 nm channel spacing, the attained receiver sensitivity was - 19.23 dBm, -19.22 dBm and -19.19 dBm respectively. As depicted in fig 5.7, no remarkable RF clock signal interference effect on the data signal was noted at B2B analysis. A 24.75 Km fibre transmission was noted to introduce a transmission penalty of 0.71 dB when only the 10 Gbps data signal was considered for transmission without any interference from the RF clock signal.

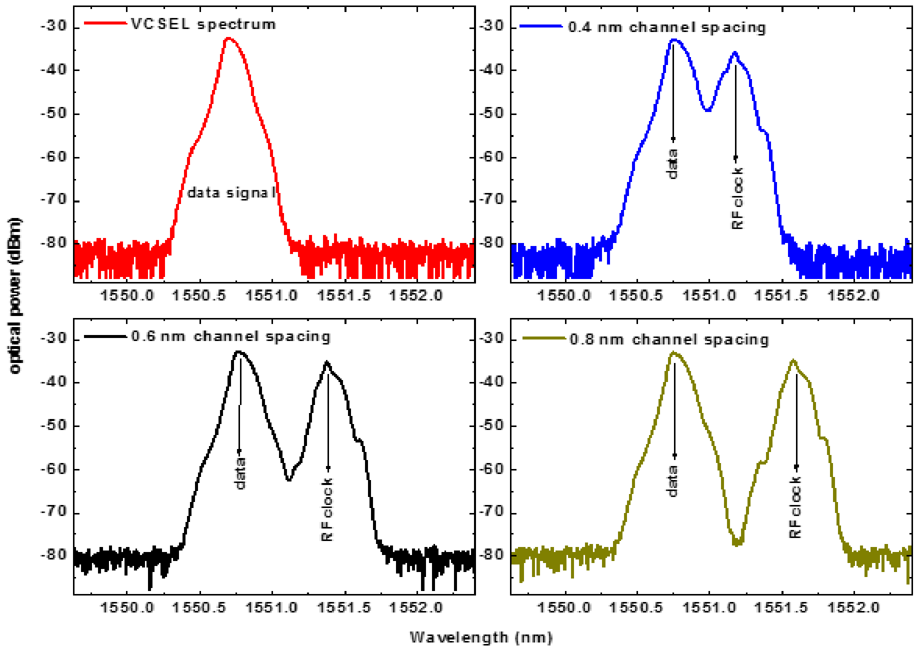

Fig 5.6: Resultant optical spectrum for data signal (red), data and RF clock signals at 0.4 nm (blue), 0.6 nm (black) and 0.8 nm (green) channel spacing respectively.

However, by introducing simultaneous data and RF signal transmission over this fibre length, a penalty of 0.78 dB, 0.91 dB and 1.15 dB was incurred for 0.8 nm, 0.6 nm and 0.4 nm channel spacing respectively. This penalty was a combined effect of transmission penalty due to the fibre length, and the RF clock signal interference penalty on the data signal. The receiver sensitivity was noted to reduce with a decrease in channel spacing over a fibre transmission as shown in fig 5.7. This was due to the fact that as the channel spacing is reduced, the data and RF clock signal channel overlap more as shown in fig 5.6. This therefore leads to more interaction between the transmitted data and RF clock signal over a fibre transmission length, thus resulting to RF clock signal interference effect on the data signal. The resultant interference degraded the quality of the data signal as it resulted to error-bits close to the BERT decision level of the data bits thus accounting for the degraded performance observed at 0.4 nm channel spacing as shown in fig 5.7 [257-262].

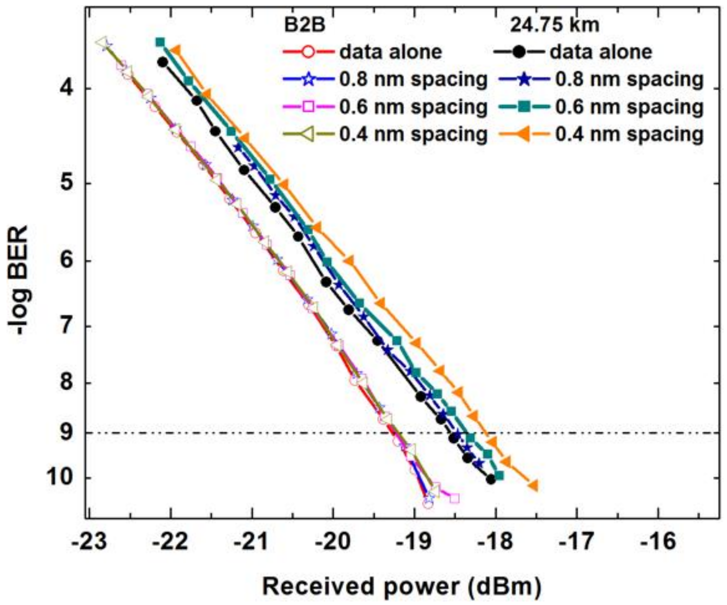

Fig 5.7: BER curves for simultaneous data and RF clock signal transmission at B2B analysis and 24.75 Km transmission length of G. 655 SMF-RS fibre at 0.4 nm, 0.6 nm and 0.8 nm channel spacing respectively.

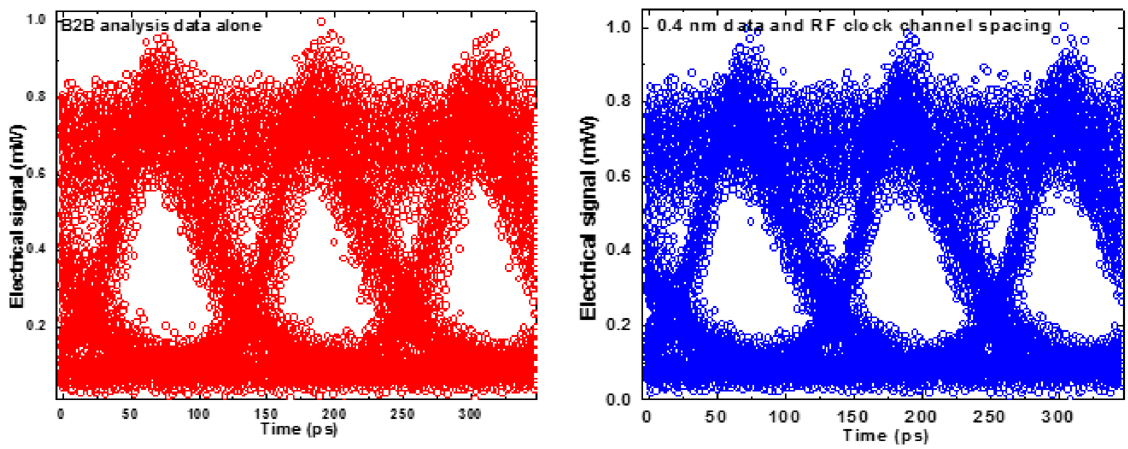

Fig 5.8: The B2B eye diagrams for data channel alone (red), coupled data and RF clock channels at 0.4 nm channel spacing.

The back-to-back eye diagram for 10 Gbps data signal without RF clock signal interference (red) and with RF clock signal interference (blue) at 0.4 nm channel spacing is shown in fig 5.8. Both eyes (with and without adjacent interfering RF clock signal) were noted to be clear and wide open, implying an error-free transmission.

5.2.2 Experimental analysis of effects of data signal on reference clock tone distribution at different channel spacing

The impact of simultaneous 10 Gbps data transmission on the stability of 1.712 GHz RF clock was analyzed experimentally through phase noise and clock jitter measurement as reported in our work in [151]. This was achieved using a direct method with a Rohde & Schwarz spectrum analyzer [115, 263]. Clock jitter and phase noise measurement were taken over a resolution bandwidth of 1 Hz to 1 MHz. Short term optical reference clock signal stability (Jitter) is key in telescope array networks, for proper control performance of signal to noise degradation during data digitization process. Long term stability on the other hand is mostly vital for applications such as very large baseline interferometry (VLBI) and certain kinds of astronomical observation such as pulsar work. VLBI involves simultaneous synchronization of various remote receptors in telescope array networks [3].

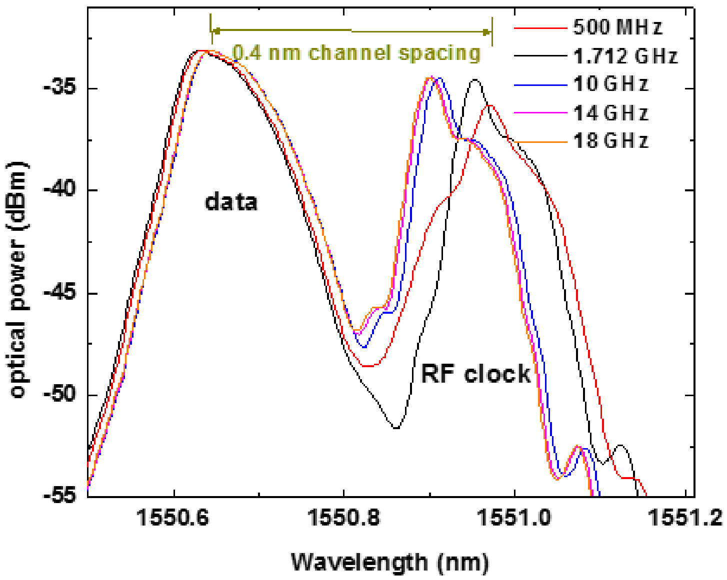

Fig 5.9: Resultant optical spectrum for data and RF clock signal at 0.4 nm channel spacing for different RF clock frequencies.

Fig 5.9 shows the resultant data and RF spectrum channels after coupling at 500 MHz, 1.712 GHz, 10 GHz, 14 GHz and 18 GHz RF modulation frequencies respectively. The resultant spectra band overlap in fig 5.9 was noted to reduce with an increase in modulation RF clock frequency. The higher the modulation clock frequency, the higher the spectrum usage and the more the data and RF clock spectra band overlap.

The power spectrum analysis plot used to characterize the effect of 10 Gbps data transmission on phase noise performance of a 1.712 GHz RF clock signal at 0.4 nm - 0.8 nm for back to back (B2B) analysis is shown in fig 5.10. All the power spectrums (0.4 nm – 0.8 nm) were noted to have a similar characteristics appearance as shown in fig 5.10. The spectrum peak was noted to be at 1.712 GHz which was the nominal modulation frequency used.

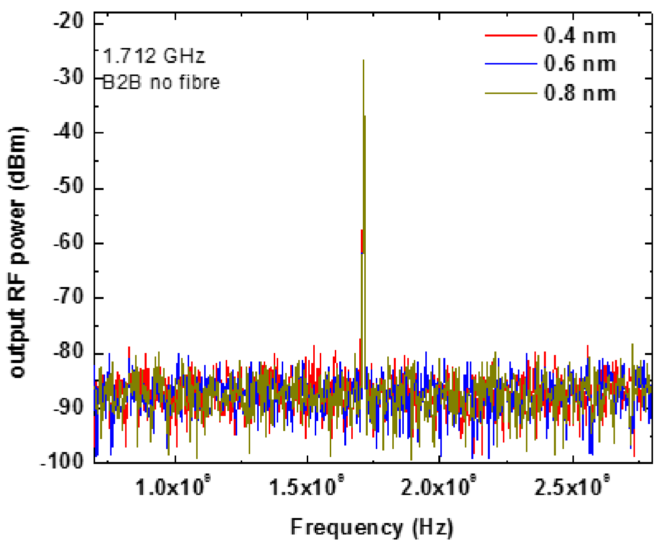

Fig 5.10: Power spectrum for simultaneous 1.712 GHz RF clock signal and data transmission for B2B analysis at 0.4 nm, 0.6 nm and 0.8 nm channel spacing.

The graphed log-log plot of single side band (SSB) phase noise of amplitude versus frequency offset as measured from an electrical spectrum analyzer for 0.4 nm - 0.8 nm is shown in fig 5.11. A simultaneous transmission over a 24.75 Km fibre length of G. 655 SMF-RS fibre was experimentally attained in this study. The vertical axis is an amplitude relative to the carrier (which is not shown), while the horizontal is the frequency offset from the carrier. A SSB phase noise of -120.98 dBc/Hz was attained for B2B analysis without data signal interference at a frequency offset frequency of 10 KHz. However, with the introduction of an interfering data signal, the attained SSB phase noise increased to - 121.18dBc/Hz, -20.64 dBc/Hz and -120.15 dBc/Hz for 0.8 nm, 0.6 nm and 0.4 nm channel spacing respectively at the same frequency offset. The introduction of a 24.75 Km simultaneous RF clock signal and data transmission degraded the measured phase noise to -117.69 dBc/Hz, -115.52 dBc/Hz and -113.57 dBc/Hz respectively at a frequency offset of 10 KHz for 0.8 nm, 0.6 nm and 0.4 nm channel spacing as shown in fig 5.11.

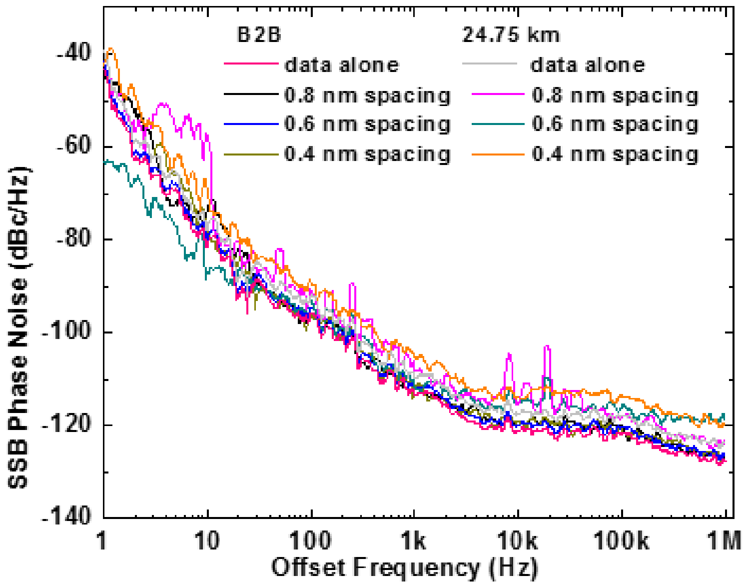

Fig 5.11: Single side band phase noise (SSB) for simultaneous RF clock and data signal transmission at B2B analysis and 24.75 Km of G. 655 SMF-RS fibre length at different 0.4 nm, 0.6 nm and 0.8 nm channel spacing.

Different characteristic regions were observed on the SSB phase noise plot shown in fig 5.11. These regions arise from different sources of oscillator noise contribution. Very close to the carrier frequency is predominated with random noise. This noise usually relates to the oscillator physical working environment. If the oscillator is affected by mechanical shocks, vibration, temperature or other environmental effects, then random noise will remarkably increase close to the carrier frequency [115, 264].

Flicker phase noise was seen to dominate between 1 Hz and 10 KHz. Flicker phase noise may be related to the physical resonance mechanism of an oscillator, choice of parts used for the electronics design of the oscillator, but it is usually added by noisy electronics. This noise type is present even in the best quality oscillators because to bring the signal amplitude up to a usable level, amplifiers are employed immediately after the signal source [264]. This therefore may introduce flicker noise in these stages. This noise can also be introduced if frequency multipliers are employed to attain higher frequencies. However, flicker phase noise can be minimized by a good quality low-noise amplifier design, and other electronic components [115, 263, 265].

White phase noise on the other hand is a broadband phase noise and has little to do with the resonance mechanism. This noise is random and has a constant power spectral density. It is probably produced by similar phenomena as flicker phase noise. Different stages of amplification are usually responsible for white phase noise accumulation. This noise can also be minimized through good quality amplifier design or increasing the power of the primary frequency source to avoid unnecessary amplification.

The measured RF clock signal jitter performance with received optical power at 0.4 nm, 0.6 nm and 0.8 nm channel spacing for B2B analysis is shown in fig 5.12. The RF clock jitter was noted to decrease while holding the general shape of the curve as the separation wavelength was increased from 0.4 nm to 0.8 nm. A 0.4 nm channel spacing showed a maximum jitter performance of 272 fs at -18 dBm received optical power. For the 0.6 nm and 0.8 nm channel spacing, a jitter of 266 fs and 263 fs was measured at the same optical power respectively as shown in fig 5.12. This corresponded to a data interference jitter penalty of 25 fs, 19 fs and 16 fs for 0.4 nm, 0.6 nm and 0.8 nm channel spacing respectively at a received optical power of -18 dBm.

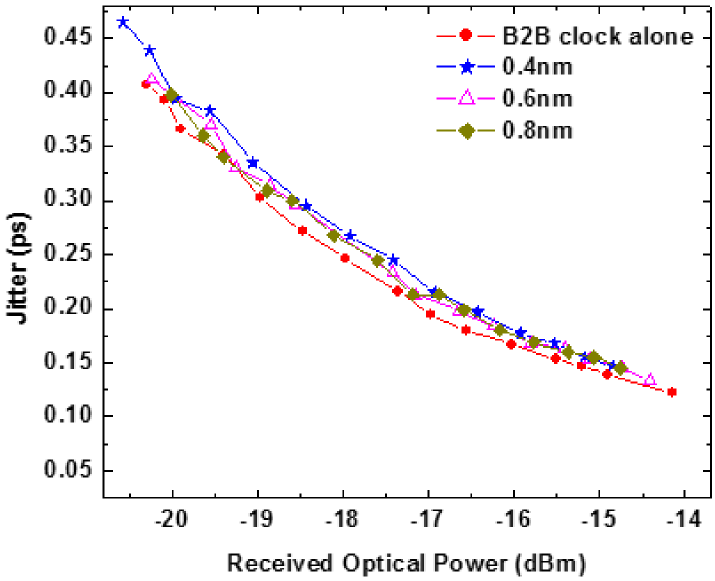

Fig 5.12: Experimentally measured RF clock jitter with received optical power at B2B analysis.

After experimentally analyzing the effect of a 10 Gbps data signal on the jitter performance of a 1.712 GHz RF clock signal at different channel spacing, a 0.4 nm channel spacing was considered for transmission. Fig 5.13 shows the experimentally measured RF jitter performance at B2B analysis and 24.75 Km fibre transmission.

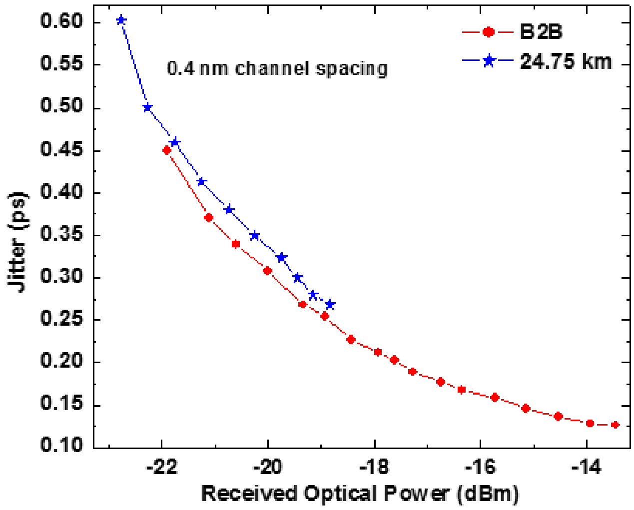

Fig 5.13: Measured RF clock jitter with received optical power at B2B analysis and over 24.75 Km of G. 655 SMF-RS fibre transmission.

A 24.75 Km fibre transmission introduced a jitter penalty of 0.02 ps at -19 dBm received power. The corresponding RF clock signal expressed in the time domain as a normalized sine wave for B2B and 24.75 Km fibre transmission is shown in fig 5.14. The sine wave remained undistorted at B2B analysis and after 24.75 Km transmission implying a successful RF clock signal distribution over fibre.

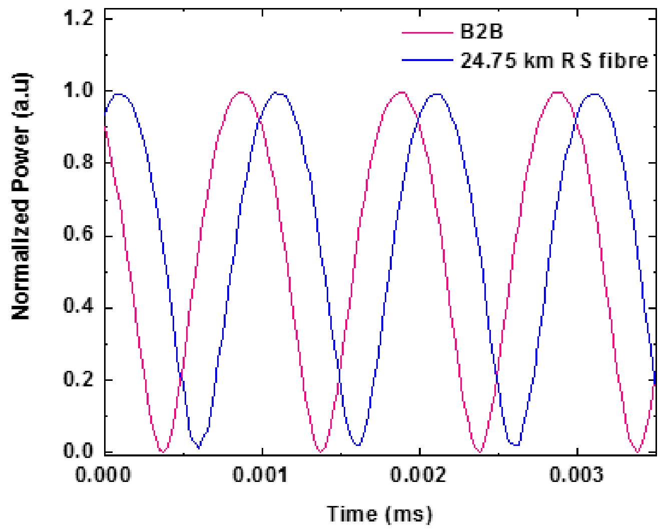

Fig 5.14: Experimentally measured 1.712 GHz RF clock signal sine wave at B2B analysis and 24.75 Km fibre transmission.

5.2.3 Experimental demonstration of simultaneous data and reference clock signal transmission over a single optical fibre at different propagation direction

After experimentally analyzing the performance of simultaneous data and RF clock signal transmission over a single optical fibre at various channel spacing, the link performance was optimized for simultaneous data and RF clock signal transmission at different directions of propagation. A 0.4 nm channel spacing was considered for co-propagation and counter propagation schemes for efficient utilization of the available bandwidth. In this section and other subsequent sections, the word co-propagation is used to imply a transmission scenario where a data signal and a reference clock signal are simultaneously propagating in the same direction.

On the other hand, counter propagation is used to refer to a scenario where the data signal is simultaneously propagated in a direction opposite to that of the RF clock signal. In the co-propagation scheme, VCSEL 1 and VCSEL 2 were directly modulated with a 1.712 GHz RF clock signal and 10 Gbps data signal respectively from the same side of the transmission link as shown in fig 5.15. A 0.4 nm channel spacing was considered in this demonstration. The two signals (10 Gbps data and 1.712 GHz RF clock) were allowed to interact by coupling them together into a signal fibre of length 24.75 Km using a 3 dB coupler. At the receiver end, an optical filter was used to separate the data signal channel from the RF clock channel for simultaneous analysis as shown in fig 5.15.

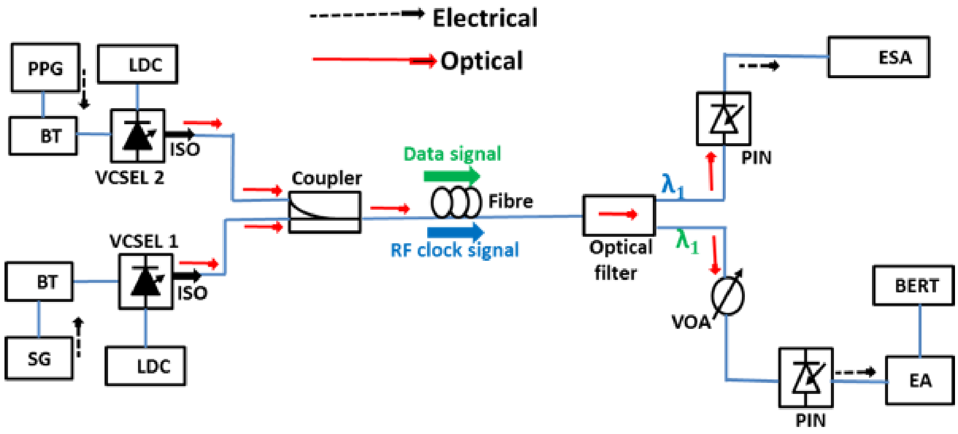

Fig 5.15: Experimental setup for co-propagating simultaneous data and RF clock signal transmission at 0.4 nm channel spacing over a single optical fibre.

For the case of a counter propagation scheme, the experimental setup in fig 5.5 was used, with the channel spacing between the data channel and RF clock signal channel restricted to 0.4 nm.

5.2.4 Experimental analysis of effects of reference clock tone on data transmission at different propagation direction

Fig 5.16 shows the resultant optically filtered and unfiltered B2B 10 Gbps data patterns for simultaneous data and RF clock signal transmission at 0.4 nm channel spacing. A co-propagation scheme was used to collect results in fig 5.16. The received unfiltered PRBS data signal was overlapped and superimposed with the RF clock signal resulting to error bits during its detection as shown by the blue plots of fig 5.16. Overlapping and superimposing of the RF clock signal on the unfiltered data signal resulted to receiver blinding by the high optical intensity of the RF clock signal channel therefore making it difficult for the PIN receiver to effectively distinguish between the ‘1’ and ‘0’ bits. However, when an optical filter was introduced to separate the RF clock signal wavelength from the data signal channel, the receiver could now distinguish clearly between the 1 and the 0 bits therefore minimizing errors as can be seen in the filtered pattern (red) in fig 5.16. Results in fig 5.16 imply that if simultaneous data and RF clock signals are to be transmitted in a co-propagating network scenario, a WDM filter should be used to separate the data channel from the RF clock signal channel before its detection to avoid errors due to receiver blinding.

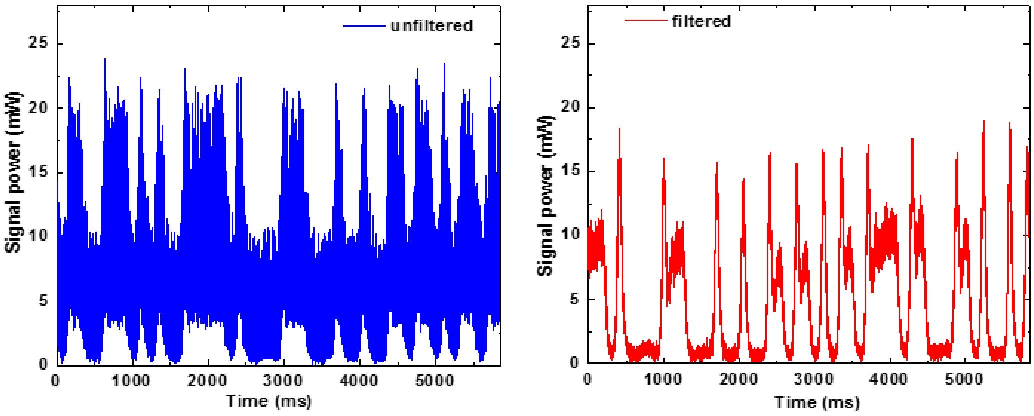

Fig 5.16: B2B simultaneous data and clock signal transmission analysis of unfiltered (blue) and filtered (red) Non-return-to-zero PRBS patterns for the co-propagation scheme.

Simultaneous data and RF clock signal transmission performance at 0.4 nm channel spacing over a single optical fibre at counter and co-propagation schemes was also studied as shown in fig 5.17. A receiver sensitivity of -19.19 dBm was attained experimentally for data channel alone without any inference. A counter propagating scheme was noted to have a superior performance compared to the co-propagating scheme as shown in fig 5.17. Receiver blinding due to the interfering channel was a key contributing factor to the performance degradation of the co-propagating scheme as shown in fig 5.17. A counter propagation scheme was noted to suffer a transmission penalty of 1.07 dB over a 24.75 Km fibre length. However, this penalty increased to 1.63 dB when a co-propagation scheme was considered for analysis.

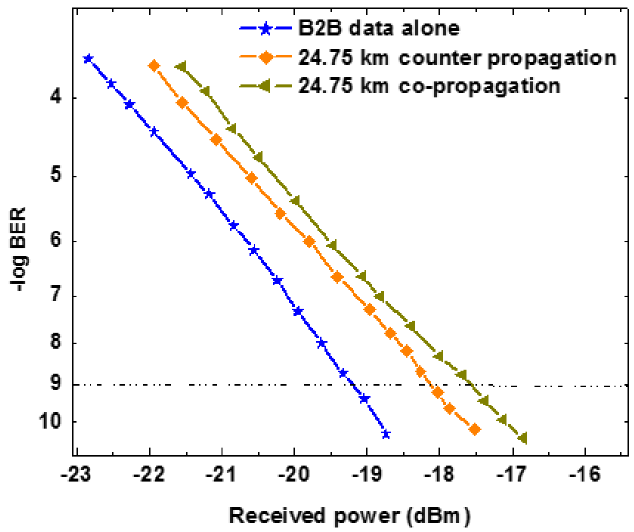

Fig 5.17: Simultaneous data and RF clock signal transmission performance at 0.4 nm channel spacing over a single 24.75 Km optical fibre at counter and co-propagation schemes.

5.3 Relevance of simultaneous data and reference clock signal transmission over a single optical fibre to telescope array networks

A fundamental scientific objective of telescope array networks such as the SKA telescope array is the need to transmit extreme amount of astronomical data at phenomenal bitrates. Optical fibre technology is the only possible solution for handling such tremendous data volumes. Moreover, distribution of reference frequency timing signals from the central science processor station over optical fibre to each of the antenna array is of extreme importance to telescope array networks. Fig 18(a), shows a typical telescope array network. Typical telescope array networks such as the SKA distributes clock tones to different digitizers mounted on remote antennae over optical fibres. The collected science data from these remote antennae is transmitted over separate optical fibres back to the processor centre as shown in fig 18(a).

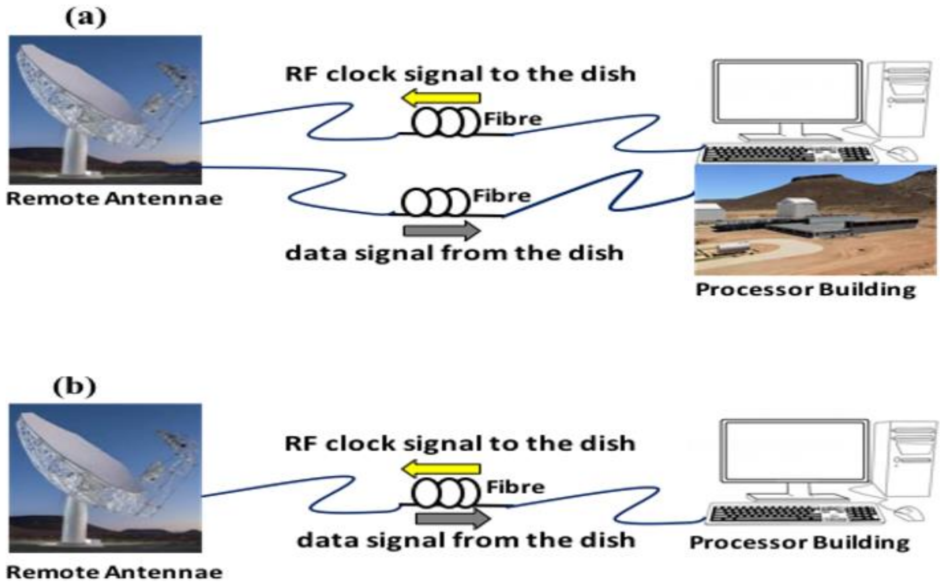

Fig 5.18: Data signal and RF clock signal transport in (a) typical telescope array network, (b) proposed next-generation telescope array network.

This type of network design approach is limited with some drawbacks such as increased complexity of the entire telescope array network. The optical fibre deployment cost of the network also increases due to large amounts of optical fibres required in such a telescope array network. For instance, it is estimated in [3, 8] that the SKA telescope array network will use enough fibres to wrap around the world twice upon its completion. A project of this magnitude therefore calls for intelligent technological design selection if its observational science objectives are to be achieved. The schematic representation of our proposed next-generation telescope array network is shown in fig 18(b). In our approach, a cost effective bidirectional VCSEL-based clock tone distribution and data transmission over a single optical fibre for next-generation telescope array networks is experimentally proposed. Our proposed telescope array network shown in fig 18(b) comes with a number of attractive benefits. First this type of network reduces network complexity therefore easing network maintenance as well as administrative and monitoring control functions. Secondly, the initial installation cost of the network is significantly reduced due to shared optical fibre infrastructure in data and clock signal distribution within the network. Moreover, the shared infrastructure allows for effective employment of corrective mechanisms within the network such as chromatic dispersion management and compensation. This study therefore proves a key concept for adoption in cost effective high-speed next-generation telescope array networks and other big science projects as well as terrestrial optical fibre networks of similar scientific objectives.

5.4 Summary

In this chapter, the use of high-speed vertical cavity surface emitting lasers (VCSELs) in optical fibre networks has experimentally been demonstrated. We have experimentally demonstrated simultaneous data and reference frequency (RF) clock signal transmission over a single optical fibre for adoption in next generation telescope array networks. The quality of the simultaneously transmitted data and RF clock signal have experimentally been analyzed simultaneously at different channel spacing, and different direction of propagation. The relevance of simultaneous data and reference clock signal transmission over a single optical fibre to telescope array networks has been presented.

The next chapter presents a novel technique of modulating a single mode 10 GHz bandwidth VCSEL in simultaneous transmission of directly modulated data signal and polarization-based pulse-per-second (PPS) clock signal. VCSEL polarization switching is experimentally demonstrated and the technique adopted by exploiting the VCSEL polarization switching with change in bias current to realize the first reported simultaneous directly modulated 10 Gbps data and polarization based Pulse-Per-Second (PPS) clock signal transmission using a single mode 10 GHz bandwidth VCSEL carrier at 1310 nm.

Chapter 6

Polarization modulation in VCSELs for simultaneous data and Pulse-Per-Second (PPS) clock signal transmission

This chapter reports on a novel modulation technique for simultaneous data and polarization-based PPS clock signal transmission using a single mode 10 GHz bandwidth VCSEL carrier. Experimental investigation into polarization-resolved light-current characteristics of a single mode VCSEL carrier is first presented. VCSEL polarization switching is experimentally demonstrated and the technique adopted to realize the first reported simultaneous directly modulated 10 Gbps data and polarization based Pulse-Per-Second (PPS) clock signal transmission using a single mode 10 GHz bandwidth VCSEL carrier at 1310 nm. Data transmission and PPS timing clock performance are simultaneously evaluated through BER measurement and statistical analysis respectively.

6.1 Experimental demonstration of polarization switching in VCSELs

VCSEL polarization dynamics is demonstrated by investigating the polarization-resolved light-current characteristics of a single mode VCSEL carrier. This was achieved by experimentally demonstrating polarization resolved light output of a VCSEL carrier. VCSEL polarization dynamic measurements were performed on a single mode commercial 10 GHz bandwidth VCSEL transmitter from RayCan Company designed for high-speed performance (data rates up to 10 Gbps). Polarization-independent parameters of a similar device have already been reported in [266]. The VCSEL device under test had an emission wavelength of 1307.05 nm at I_{bias}= 7.01 mA and a threshold current of 1.53 mA.

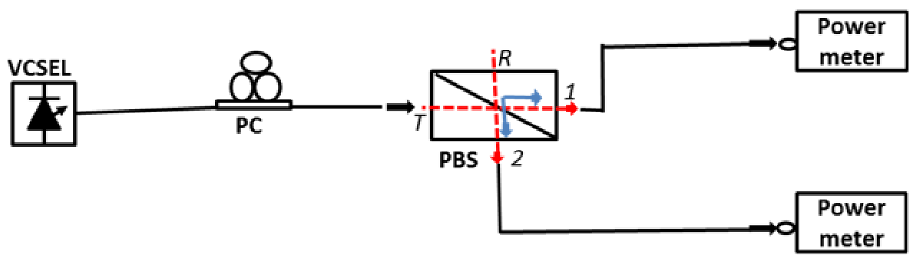

Fig 6.1: VCSEL polarization dynamic experimental set-up: PC- polarization controller, PBS- polarization beam splitter.

Fig 6.1 shows an experimental setup used to demonstrate VCSEL polarization dynamics. The optical light output from the VCSEL under test was connected into an input port of a polarization beam splitter from OZ Optics. A picture of the polarization beam splitter used in this study is shown in fig 6.2.

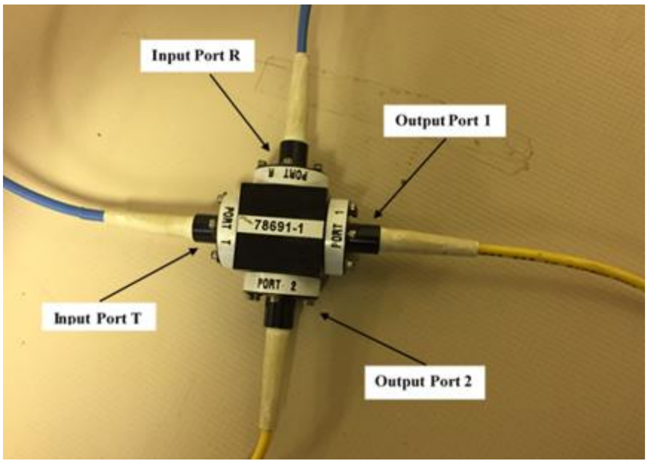

Fig 6.2: Picture of a polarization beam splitter.

The polarization beam splitter shown in fig 6.2 was used to separate the incoming VCSEL light wave into its respective orthogonal states. A Thorlabs polarization controller model number FBR05 was used to align the states of polarization (SOP) orientation of the incoming VCSEL light wave to ensure that the SOP of the incoming light wave was a resultant of the two orthogonal states of polarization. This was enabled by monitoring the output power of the two optical power meters (GFHP-B) while turning the polarization controller, until the reading on the two power meters was at the same level. It should be noted that when using polarization beam splitters with polarization maintaining fibres, it is important that one understands how the polarization axises are aligned on each port. Each input signal will transmit along a different output polarization axis as shown in fig 6.1.

Light launched along the slow axis of input port T will be transmitted along the slow axis of output port 1 and measured using power meter 1 as shown in fig 6.1 consequently, light launched along the fast axis of input port T will be transmitted along the slow axis of output port 2 and measured with power meter 2. Polarization maintaining fibres were used to connect output 1 and 2 to their respective power meters to maintain their SOPs. The VCSEL polarization-resolved light-current measurements were taken by varying the bias current from 1 mA to 9.97 mA while recording the respective output power (μW). When performing polarization-resolved light-current characterization of laser sources, it is important to only consider polarization splitters that can prevent polarized light intended for port 1 from reaching port 2 or vice versa.

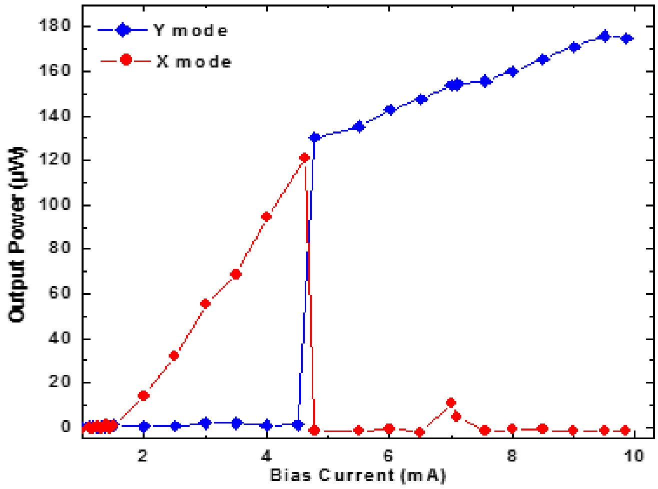

Fig 6.3: Experimentally measured polarization-resolved light-current characteristics of a free running VCSEL.

The measured polarization-resolved light current curves of a free running VCSEL are shown in fig 6.3. A polarization switch from the high-frequency (Y-mode) to the low-frequency (X-mode) polarization mode was observed near 4.68 mA bias current value. The X-mode and the Y-mode were orthogonal to each other. No appreciable hysteresis was observed. At this polarization switch point (4.68 mA), no drop of the total output power was observed. Results in fig 6.3 proves a key polarization dynamic ability of the VCSEL laser. From these polarization-resolved light-current measurements, VCSEL polarization switching between two orthogonal state of polarization was achieved at 4.68 mA bias current as shown in fig 6.3. In this experimental demonstration, the external temperature of the free running VCSEL was maintained at room temperature (Approx. 25° C) using a TEC controller circuit so that temperature effects could not come into play.

6.2 Experimental demonstration of VCSEL polarization modulation with a Pulse-Per Second (PPS) clock signal

Experimental realization of simultaneously 10 Gbps data and polarization-based pulse per second (PPS) clock signal modulation on a single mode 10 GHz bandwidth VCSEL carrier is demonstrated in this section. A 10 Gbps 1310 nm VCSEL with a bias current threshold of 1.53 mA was used in this study. To experimentally realize VCSEL polarization modulation, VCSEL polarization switching between two orthogonal states of polarization should first be achieved as reported in our earlier contribution in [207].

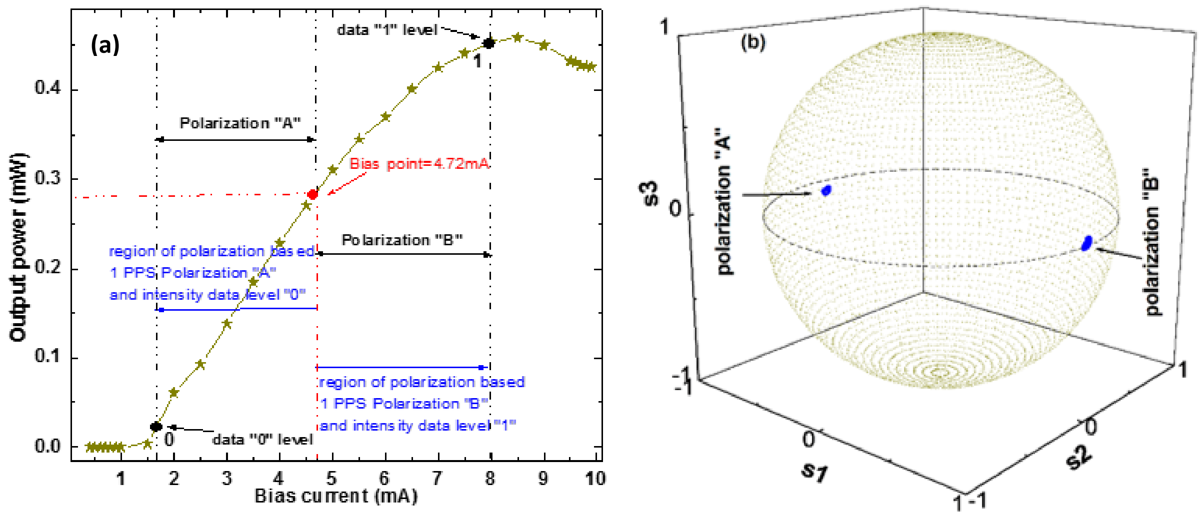

Fig 6.4: VCSEL bias characteristics curve showing the current settings used (a). Poincare sphere showing the two orthogonal polarization states of a VCSEL due to polarization switching after polarization modulated with a pulse per second signal (b).

The VCSEL was biased around its switching current region point as demonstrated in section 6.1. This biasing point was carefully selected so that any slight increase or decrease in current could result to a switch in states of polarization of the VCSEL from polarization region "A", to polarization region "B" and vice-versa as shown in fig 6.4(a). At a bias current of exactly 4.72 mA, the VCSEL was noted to be lasing at polarization state "A", as shown in the fig 6.4(a). However, a 0.2 mA increase in bias current was noted to translate to a polarization switch from polarization state "A" to polarization state "B" as shown in fig 6.4(b), therefore achieving VCSEL polarization switching. A polarization analyzer was used to monitor the polarization characteristics of the VCSEL under test thus collecting polarization results plotted and shown in fig 6.4 (b).

This mechanism was then adopted to realize the first reported VCSEL polarization modulation using a pulse-per-second (PPS) clock signal as reported in our previous contributions in [207] and [267]. A Rubidium frequency standard model FS725 was adopted to generate 1 PPS electrical clock signal of pulse width 10 μs used in this contribution. The electrical 1 PPS signal voltage was attenuated by effectively using electrical attenuators. This attenuation was meant to ensure sufficient voltage needed to induce VCSEL polarization switching due to current heating. The 1 PPS signal was therefore supposed to induce sufficient current heating to the VCSEL laser cavity upon its modulation thus leading to a switch in the VCSEL polarization state each time a pulse voltage is output (i.e. every 1 second). The pulse width of 1 PPS electrical signal used was also sufficiently enough for the realization VCSEL polarization switching. This is because the 10 μs PPS pulse width was just enough to ensure that the VCSEL laser was driven with an electrical pulse shorter than its thermal relaxation time [223, 226, 229, 231, 235].

6.3 Experimental implementation of simultaneous data and polarization-based PPS clock transmission using a single VCSEL carrier

PPS timing clock signals have vastly been used for time keeping in optical communication networks such as banking and data centres [268]. For instance, clocks on networked devices such as servers, racks/pod should be in sync to avoid loss of vital corporate data. Simultaneous distribution of data and timing clock signals over shared network infrastructure is thus preferable in such systems.

The experimental setup in fig 6.5 was used to demonstrate simultaneous data and PPS clock signal transmission using a single VCSEL carrier. A programmable pattern generator was used to generate a 10 Gbps pseudo random bit sequence electrical data signal of pattern length 2^7-1 used to directly modulate the VCSEL carrier through its bias-tee. A second signal, a PPS clock signal was simultaneously modulated onto the polarization states of the VCSEL carrier through the laser diode controller input to achieve polarization modulation as described in section 6.2. Therefore, a 10 Gbps data signal and a polarization-based PPS clock signal were simultaneously modulated on a single mode 10 GHz bandwidth VCSEL carrier. After simultaneously modulating a single VCSEL carrier with an intensity based 10 Gbps data and polarization-based pulse per second clock signal, transmission and signal recovery over an 11 Km G.652 fibre link was successfully demonstrated. At the receiver end, the optical signal after transmission was split using an optical splitter, for simultaneous analysis of the 10 Gbps data and polarization-based PPS clock signal as shown in fig 6.5.

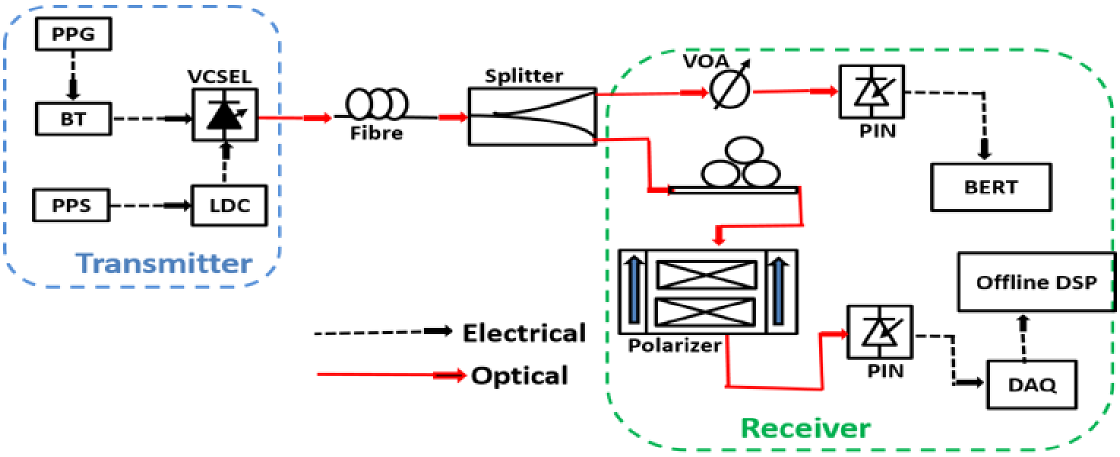

Fig 6.5: Experimental setup for simultaneous 10 Gbps data and polarization-based pulse-per-second clock transmission using a single VCSEL: VOA-variable optical attenuator, PIN-positive intrinsic negative photodiode, PPG- Programmable pattern generator, LDC- laser diode controller, BT-bias Tee, PC-polarization controller, BERT-bit error rate tester and PPS-pulse per second.

For qualitative analysis of the directly modulated 10 Gbps data signal, the optical power getting into the positive intrinsic negative (PIN) photodiode after the splitter was varied using a variable optical attenuator. This was meant to emulate optical losses incurred in a real deployed optical fibre network. In optical fibre networks, the optical signal power degrades exponentially with increase in fibre transmission length due to signal attenuation within the optical fibre medium. A PIN photodiode was used to recover the transmitted data signal and the recovered signal quality analyzed through bit error measurement (BER) and eye diagram representation using a bit error rate tester and a sampling oscilloscope respectively.

6.3.1 Recovery of polarization-based PPS clock signal using a polarizer

Due to unavailability of a polarization sensitive photodiode in our laboratory, it was important to develop a reliable technique that could be used to recover the polarization-based PPS clock signal from the polarization states of the VCSEL carrier to its intensity attribute, to enable its detection with an intensity sensitive PIN photo receiver that was readily available in the laboratory. To achieve this, an optical polarizer was used as shown in fig 6.6. Polarizers are optical filters that allow incoming light wave of a specific state of polarization to pass through and blocks light waves of other states of polarization orientation. Polarizers can convert a beam of light of defined or mixed polarization into a beam of well-defined polarization, which is polarized light. Common used types of polarizers are the linear and circular polarizers. In this work, a linear polarizer was used due to its availability.

Firstly, it is important to note that optical fibres are expected to maintain the same state of polarization of the input light wave throughout their transmission lengths. However, due to birefringence and mode coupling arising from different affecting conditions within the optical fibre link, the polarization stability of the optical light is altered.

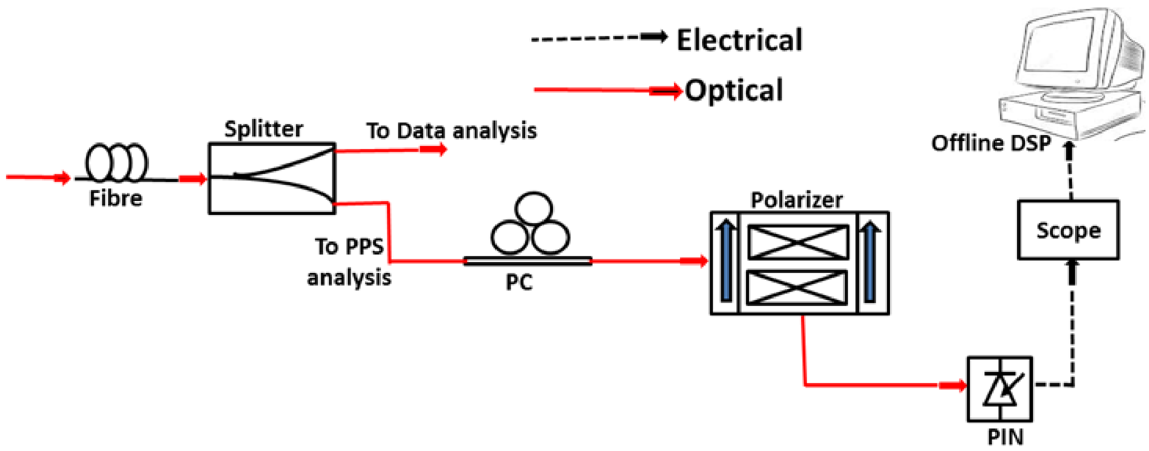

Fig 6.6: Experimental setup used to recover polarization-based PPS clock signal.

It is for this reason that polarization controllers were used to re-align the polarization states of the VCSEL light wave to match with that of the linear polarizer. As described in section 6.2, VCSEL polarization modulation with PPS clock signal brings about an output light wave switching between two orthogonal states of polarization. A polarization controller was therefore used to align one of these polarization states to match that of the linear polarizer used. This therefore ensured that a linearly polarized optical light wave passed though the polarizer each time a PPS signal was in this state of polarization and minimal light to pass when in the orthogonal polarization state. This therefore led to a high voltage detection on by the PIN receiver each time the PPS signal was in this state of on polarization and vice versa. This therefore ensured recovery of PPS from VCSEL polarization states back to intensity for detection with our PIN photodiode. The received PPS electrical signal was then captured using an Agilent sampling scope for offline statistical analysis.

6.3.2 Statistical analysis of simultaneous modulated polarization-based PPS clock signal transmission

In this section, statistical analysis measurement of the received polarization based PPS clock signal after its transmission over 11 Km of G. 652 optical fibre are presented. The measure PPS pulse width results are shown in fig 6.7.

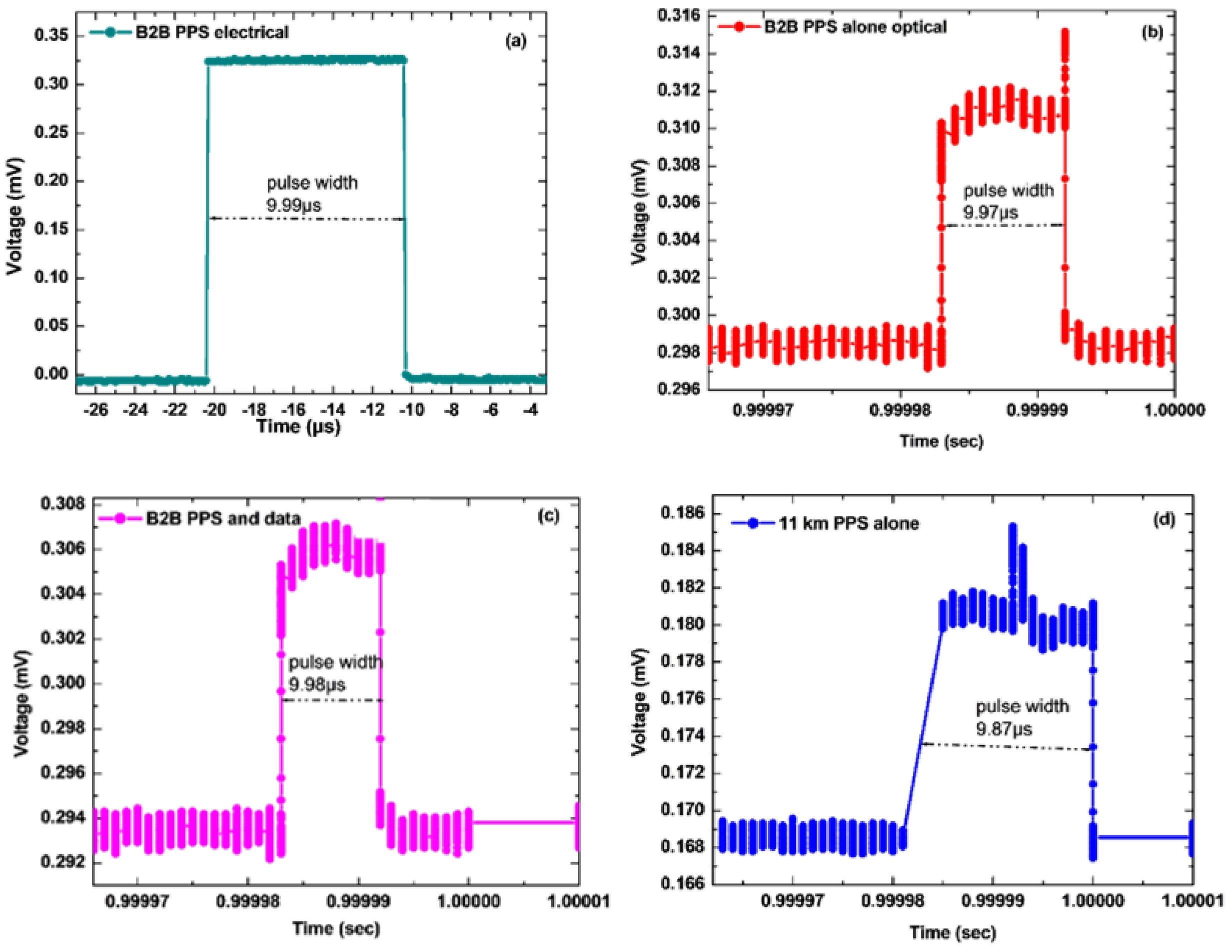

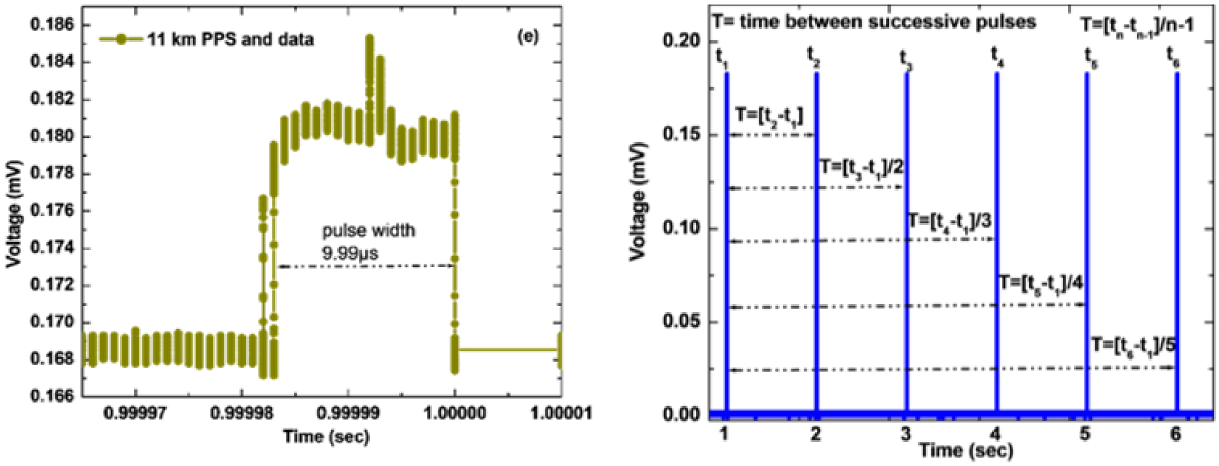

Fig 6.7: PPS measured pulse width for (a) B2B electrical, (b) B2B optical polarization based PPS modulation, (c) B2B simultaneous intensity 10 Gbps data and polarization based PPS modulation, (d) polarization based PPS modulation after 11 Km of G. 652 fibre transmission, (e) 11 Km fibre transmission of simultaneous intensity 10 Gbps data and polarization based PPS signal, (f) Time distribution measurement between successive pulses.

The pulse width was measured by taking the time difference between the pulse rising edge and falling edge of individual received PPS electrical pulse signals, at full width at half maximum (FWHM). A PPS pulse width of 9.99 µs, 9.97 µs, 9.98 µs, 9.87 µs and 9.99 µs was experimentally measured at B2B electrical signal, B2B optical polarization based PPS modulation, B2B simultaneous intensity 10 Gbps data and polarization based PPS modulation, polarization based PPS modulation after 11 Km of G. 652 fibre transmission, and 11 Km fibre transmission of simultaneous intensity 10 Gbps data and polarization based PPS signal respectively. This corresponded to a deviation of -0.01 µs, -0.03 µs, -0.02 µs, -0.13 µs, and -0.01 µs respectively, from the 1 PPS actual pulse width of 10.00 µs as stated in [269]. These deviations may have been contributed by the cumulative equipment error. It was noted that the PPS pulse peak appeared slightly distorted upon its detection. This might be due to chirping property of the VCSEL laser source [270-272]. However, this did not affect the integrity of the rising and falling edges of the PPS clock signal as seen in fig 6.7. This is the key requirement for timing clock signals, in time and frequency reference application systems.

A frequency count distribution of the measured time between successive pulses is presented in fig 6.8. Results in fig 6.8 were obtained by taking the time difference between the rising edge of the first pulse and that of each successive pulse as shown in fig 6.7(f). The formulae $T = \frac{[t_n - t_1]}{n-1}$ was applied, where T is the time between the rising edges of successive pulses, t is time in seconds for individual pulses and n is an integer number of pulses considered for analysis. In our analysis, a total of 60 pulses were consider. Their respective frequency count distribution over time are shown in fig 6.8. From results in fig 6.8, a maximum count was seen at 1 sec for all experimental scenarios considered. This implied that the PPS clock signal retained its timing property (a pulse every second) even after simultaneous transmission with intensity based data signal over a fibre length.

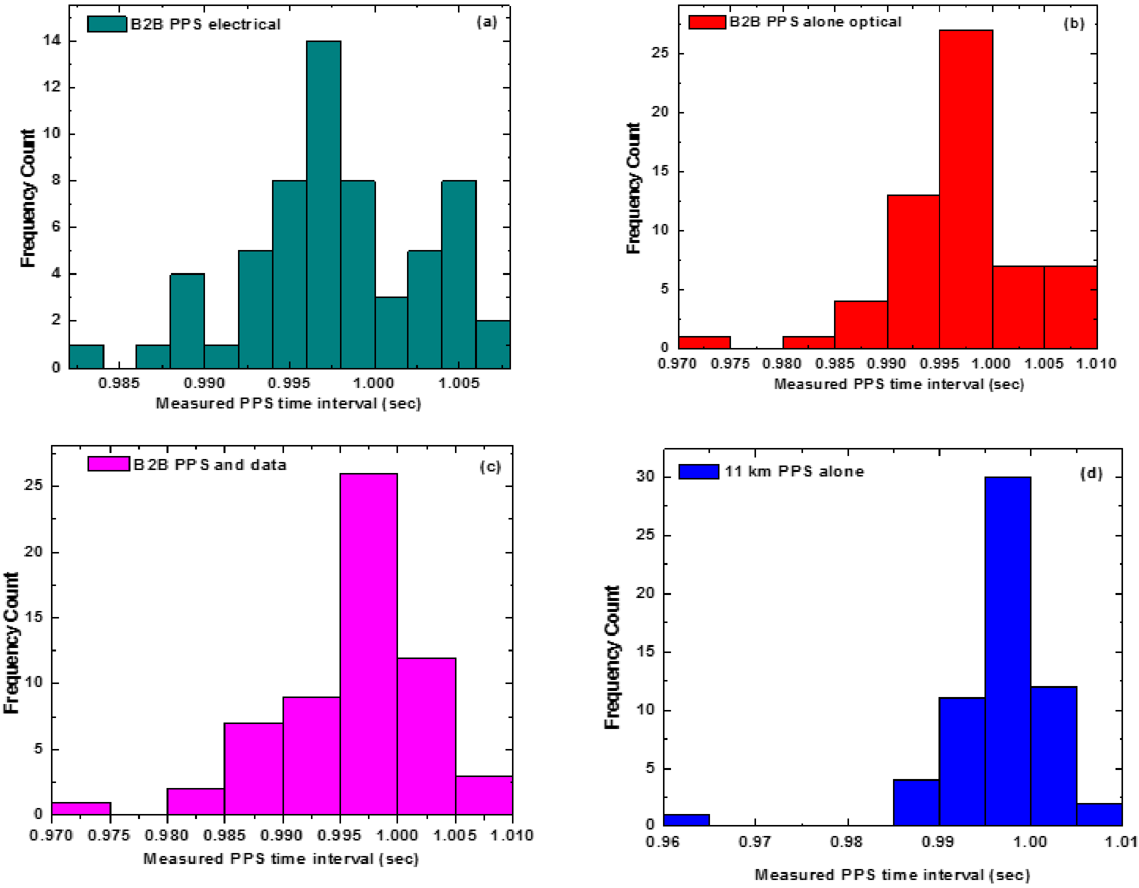

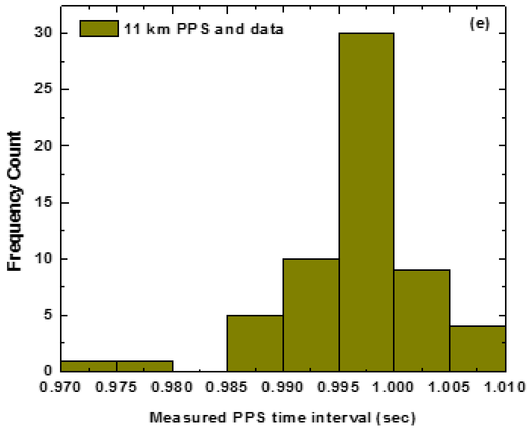

Fig 6.8: Time frequency count measurement (a) B2B electrical, (b) B2B optical polarization-based PPS modulation, (c) B2B simultaneous intensity 10 Gbps data and polarization-based PPS modulation, (d) polarization-based PPS modulation after 11 Km of G. 652 fibre transmission, (e) 11 Km fibre transmission of simultaneous intensity 10 Gbps data and polarization-based PPS signal.

6.3.3 Transmission performance of simultaneous directly modulated 10 Gbps data signal

This section presents the transmission performance of a 10 Gbps data signal simultaneously modulated with a polarization-based PPS on a single 1310 nm VCSEL laser source and transmitted for 11 Km of G. 652 optical fibre. Fig 6.9 shows experimental BER measurement for simultaneous 10 Gbps VCSEL data transmission with a polarization based PPS over 11 Km of G. 652 fibre. A receiver sensitivity of -16.27 dBm was experimentally measured for B2B analysis without polarization-based PPS clock signal. From results in Fig 6.9, a 10 Gbps VCSEL transmission with polarization-based PPS clock signal introduced a transmission penalty of 0.52 dB over 11 Km fibre length. The contribution of polarization-based PPS clock signal to this penalty was found to be 0.08 dB, indicating that the added PPS transmission using polarization has a negligible impact on the co-transmitted intensity modulated signal under stable polarization conditions.

Fig 6.10 shows respective eye diagrams for 10 Gbps 1310 nm VCSEL transmission at both back-to-back and 11 Km fibre without (red) and with (green) polarization-based PPS clock signal. As depicted in fig 6.10, both back-to-back and 11 Km G. 652 fibre transmission without and with polarization-based PPS clock signal had a clearly open eye. A clearly open eye imply that the receiver could clearly distinguish between the “1” and “0” levels of the data signal. A clear eye opening also signifies signal clarity. The clearer the eye opening, the better the quality of the transmitted signal implying minimal data error bits received. However, the eye sizes for back-to-back and 11 Km transmission had different intensities due to signal attenuation which increases exponentially with fibre length [241, 242].

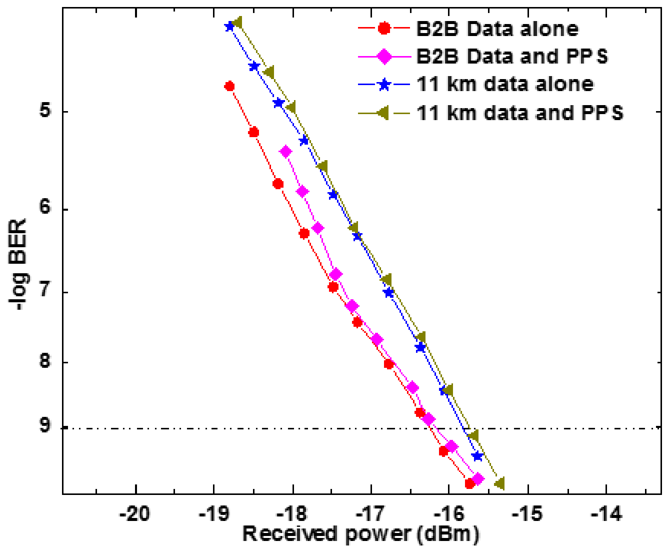

Fig 6.9: Experimental BER measurement of VCSEL data transmission with polarization-based PPS clock signal.

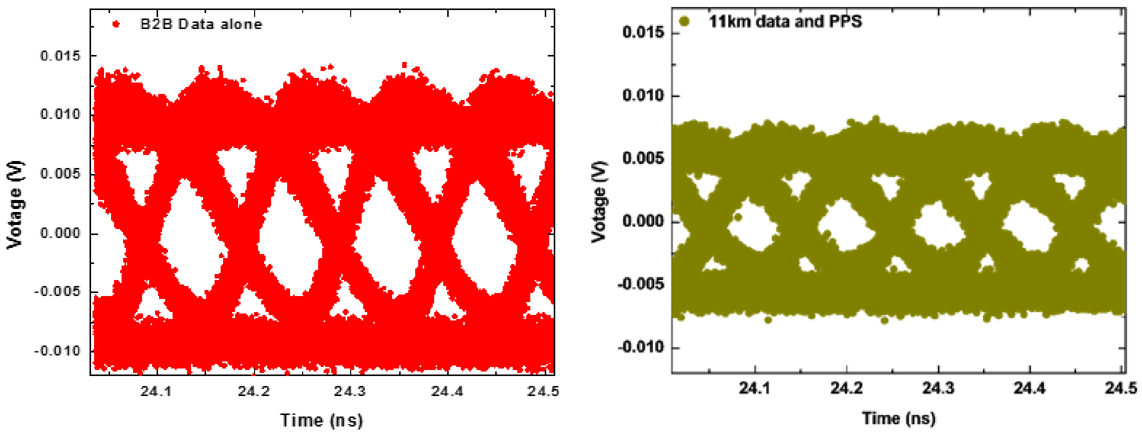

Fig 6.10: Experimentally measured eye diagrams corresponding to back-to-back (red) and 11Km (green) of G.652 fibre transmission.

6.4 Summary

In this chapter, VCSEL polarization dynamics characterization have experimentally been demonstrated and investigation into polarization-resolved light-current characteristics of a single mode VCSEL carrier discussed. VCSEL polarization switching has also been achieved experimentally. VCSEL polarization switching has been adopted to realize a novel multi-signal modulation technique reported in this chapter. Simultaneous directly modulated 10 Gbps data and polarization-based Pulse-Per-Second clock signal transmission using a single mode 10 GHz bandwidth VCSEL carrier at 1310 nm has experimentally been demonstrated and 11 Km of G 652 single mode fibre transmission achieved.

The next chapter presents some exciting alternative techniques for capacity, efficiency and flexibility upgrade in terrestrial optical fibre transmission systems like telescope array networks. This includes implementation of simultaneous data and reference frequency (RF) signal transmission in wavelength division multiplexing (WDM) systems, optical reference frequency clock signal recovery using the delay line interferometric technique, transmission performance of simultaneous 30 Gbps (3×10 Gbps) WDM data signal, stability analysis of simultaneous 12 GHz (3×4 GHz) WDM RF clock signal, simulation demonstration of 625 Gbps (25×25 Gbps) DWDM data transmission and the relevance of WDM and simultaneous data and RF clock signal transmission to telescope array networks.

Chapter 7

Simultaneous data and reference frequency clock transmission in Wavelength Division Multiplexing (WDM) solutions

This chapter, demonstrates simultaneous directly modulated data and phase modulated reference clock signal transmission over a single wavelength in WDM solutions. Three WDM channels are multiplexed at 100 GHz channel spacing and a total capacity of 30 Gbps (3×10 bps) data and 12 GHz (3×4 GHz) reference clock signal simultaneously transmitted over a single mode fibre of length 24.73 Km. A differential delay line interferometry technique is developed and used to recovery the simultaneous phase modulated RF clock signal. Data transmission and RF clock stability performance of the multiplexed channels are individually analyzed simultaneously through BER, phase noise and Allan variance measurements respectively. A 625 Gbps (25×25 Gbps) dense wavelength division multiplexing (DWDM) data transmission system is implemented in simulation by multiplexing 25 channels at 25 Gbps per channel using 50 GHz channel spacing. The relevance of WDM solutions for simultaneous data and RF clock signal transmission in telescope array networks is reported.

7.1 Experimental implementation of simultaneous data and reference frequency signal transmission in WDM systems

The experimental setup used to demonstrate simultaneous 30 Gbps (3×10 Gbps) directly modulated data and 12 GHz (3×4 GHz) phase modulated reference frequency (RF) clock signal transmission over a single optical fibre is shown in fig 7.1. Three channels each with simultaneous 10 Gbps intensity modulated data and 4 GHz phase modulated RF clock signal were multiplexed at 100 GHz spacing and directed into a single fibre strand of length 24.73 Km as shown in fig 7.1. The experimentally demonstrated multiplexed channel spacing of 100 GHz as well as the simultaneous cumulative data and reference frequency signals achieved in this section were limited by the availability of multiplexing/demultiplexing and modulating/demodulating components in our laboratory. However, much higher data rates multiplexed at more spectral efficient channel spacing that could not be achieved experimentally were simulated as demonstrated in section 7.2.

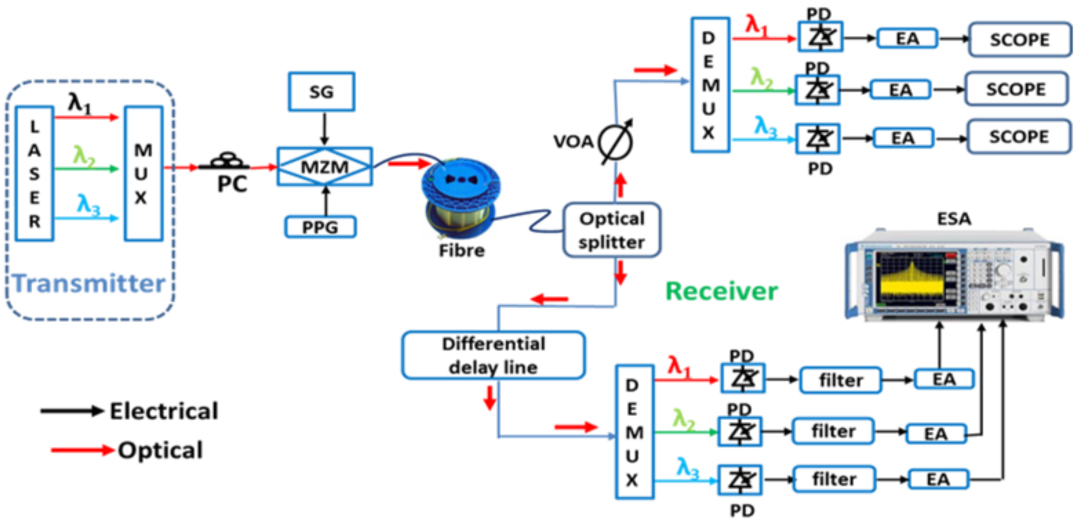

Fig 7.1: Experimental illustration of wavelength division multiplexing (WDM) optical link for simultaneous 30 Gbps (3×10 Gbps) directly modulated data and 12 GHz (3×4 GHz) phase modulated RF clock signal transmission over a single 24.73 Km fibre strand: PC-polarization controller, SG-signal generator, MZM-Mach-Zehder modulator, PPG- Programmable pattern generator, VOA-variable optical attenuator, PD- Photodiode (positive intrinsic negative photodiode), EA-electrical linear amplifier and ESA-electrical spectrum analyser.

A PRO 8000 WDM laser source from THORLABS shown in fig 7.2 was used as a transmitter source. Three channels, (channel 8, channel 6 and channel 5) at emission wavelengths of 1550.12 nm, 1550.92 nm and 1551.72 nm respectively were multiplexed using a 100 GHz 8 channel WDM multiplexer from oemarket.com. Channels 8, 6 and 5 of the WDM laser source were matched and connected to channels 34, 33 and 32 of the WDM multiplexer respectively. The multiplexed signals were forwarded into a single line output and connected to a 40 G $LiNbO_3$ Mach-Zehnder modulator (MZM) [273].

A polarization controller was first placed before the input of the modulator to ensure that the incoming light wave to the modulator chip achieves a desired orientation for its optimum modulation. This is because the $LiNbO_3$ amplitude and phase Mach-Zehnder modulator used for this experiment is highly polarization sensitive. The $LiNbO_3$ material in the Mach-Zehnder modulator is birefringent and since the electric field is applied along one direction only by the electrodes, the incoming light must therefore be launched in the waveguide along a specific direction as accurately as possible [274, 275].

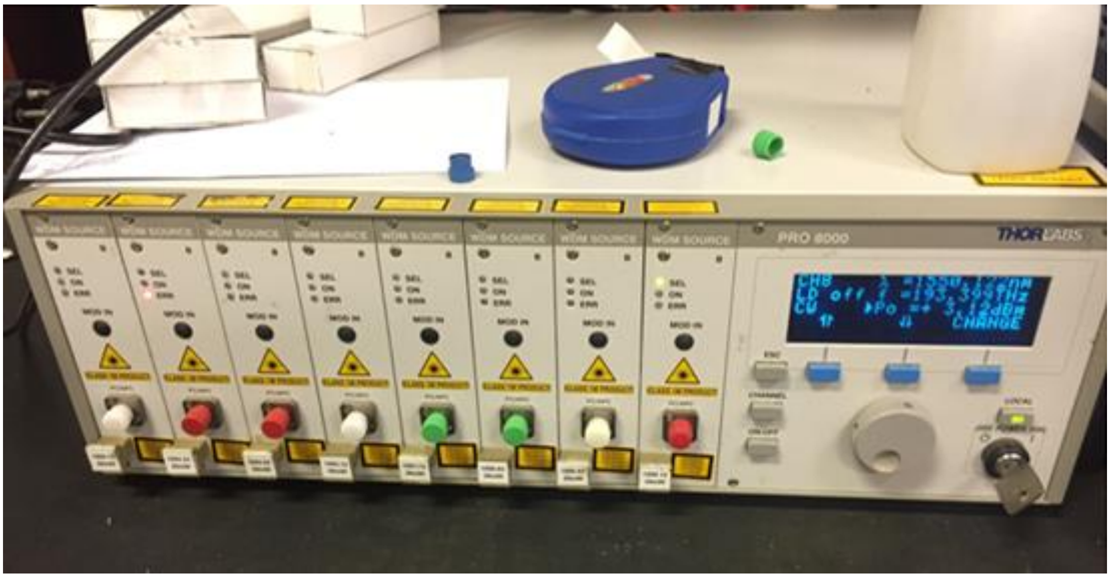

Fig 7.2: A PRO 8000 WDM laser transmitter source from THORLABS showing the different transmitter channels.

The Mach-Zehnder amplitude and phase modulator was simultaneously driven by a 10 Gbps, 2^7-1 NRZ pseudo-random bit sequence data on the amplitude modulation input port, and a 4 GHz RF clock signal from a signal generator on the phase modulation input port. The three multiplexed wavelengths therefore shared the same Mach-Zehnder modulator infrastructure for simultaneous data and RF clock signal modulation. This alone came with a benefit of cutting down the number of modulators required in the optical fibre network, thus reducing the power consumption and initial installation cost of the fibre network infrastructure. The three multiplexed channels were launched into a standard 24.73 Km SMF-RS fibre. An aggregated bit rate of 30 Gbps data and 12 GHz RF clock signal was transmitted over the fibre. At the receiver end, an optical splitter was used to divide the incoming optical signal into two for simultaneous recovery and analysis of the individual intensity modulated data and phase modulated data and RF clock signals respectively. A 100 GHz 8 channel WDM de-multiplexer was placed on each splitter end to separate the incoming light source into respective channels for performance analysis. Transmission performance of the intensity modulated 10 Gbps data signal per channel was analyzed through BER curves and eye diagram representation for the three channels. Stability of the simultaneously phase modulated 4 GHz RF clock signal per channel was also analyzed simultaneously through phase noise measurement and Allan variance representation.

7.1.1 Experimental demonstration of RF clock signal recovery using delay line interferometry technique

Due to unavailability of a phase sensitive photodiode in our laboratory, it was important to develop a reliable technique that will be used to recover the phase modulated reference frequency clock signal from the phase attribute of the VCSEL carrier to its intensity attribute, to enable its detection with an intensity sensitive PIN photo receiver that was readily available in the laboratory. To achieve this, a differential delay interferometric technique was adopted using an optical differential delay line as shown in fig 7.3. It is important to note that optical fibres are expected to maintain the same state of polarization of the input light wave throughout their transmission lengths. However, due to birefringence and mode coupling arising from different affecting conditions within the optical fibre link, the polarization stability of the optical light is altered.

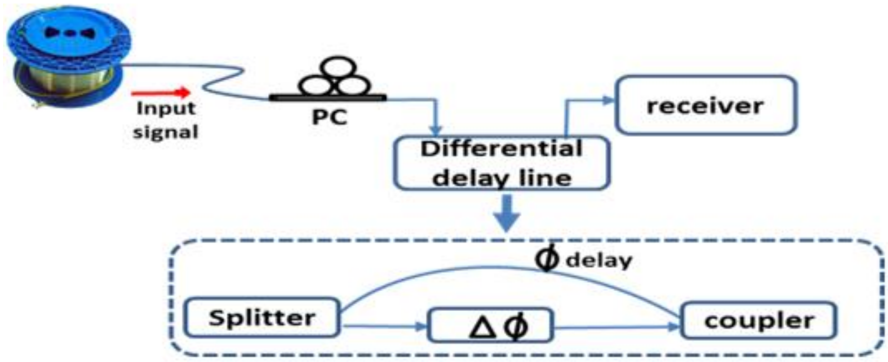

Fig 7.3: Optical demodulation of 4 GHz phase modulated RF clock signal with a differential delay interferometry.

It is for this reason that a polarization controller was placed just before the differential delay line to convert the arbitrary polarizations from the input fibre into polarizations corresponding to the orthogonal polarization controlled by the differential delay line. The differential delay line splits an incoming light wave into orthogonal states of polarization, and then actively varies the time that one polarization state travels compared to the other polarization before combining the two polarization states. Using this technique, a 7.16 picoseconds (1 bit delay) differential time delay was used therefore allowing the phase modulated RF signal to interfere both constructively and destructively upon coupling. This led to a sinusoidal wave with high and low voltage, detectable by an intensity sensitive PIN photodiode. A 3500-4500 MHz bandpass filter model number VBFZ-4000+ from Mini-Circuits company was used to filter out the RF clock signal from the data signal. The bandpass filter had a central frequency of 4000 MHz and a passband loss of < 2.4 dB. A 0.1-18 GHz wideband electrical linear amplifier model number ZVA-183W+ from Mini-Circuits company was used to boost the filtered electrical signal before its stability performance analysis. This amplifier had a typical high flat gain of 27 dB and a high output power of 26 dB. The stability of the received RF clock signal was analyzed through phase noise and Allan variance measurement using a direct and frequency count method by a spectrum analyzer respectively.

7.1.2 Transmission performance analysis of simultaneous 30 Gbps (3×10 Gbps) WDM data signal

The optical signal spectrum at the output of the transmitter side is shown in fig 7.4(a). As can be seen, all the 3 channels are well separated with no spectral distortion observed. The signal spectrum optical power was found to be well equalized over 1.6 nm (from 1550.12 nm to 1551.72 nm). After successful multiplexing and simultaneous modulation of the 3 channels with a 10 Gbps intensity-based data signal and a 4 GHz phase modulated RF clock signal per multiplexed channel, the bit-error-ratio (BER) performance of individual channels was analyzed at back-to-back as shown in fig 7.4(b). BER is defined as the probability of the decision circuit of the receiver to incorrectly identify a bit, i.e. it is the sum of the probabilities of bit ‘1’ being identified as bit ‘0’ and vice versa. In digital communication, a transmission link is typically characterized by BER as a function of the minimum average power required at the receiver, in comparison with the case where the laser is tested directly without the link (back-to-back). If for instance more power is required due to the insertion of the fibre and other link components, the additional power required by the receiver is called the power penalty. Power penalty maybe caused by fibre dispersion, laser frequency chirping, jitter, extinction ratio, laser noise or other optical elements in each link [241, 276]. Therefore, a thorough BER characterization is very important in any digital communication link.

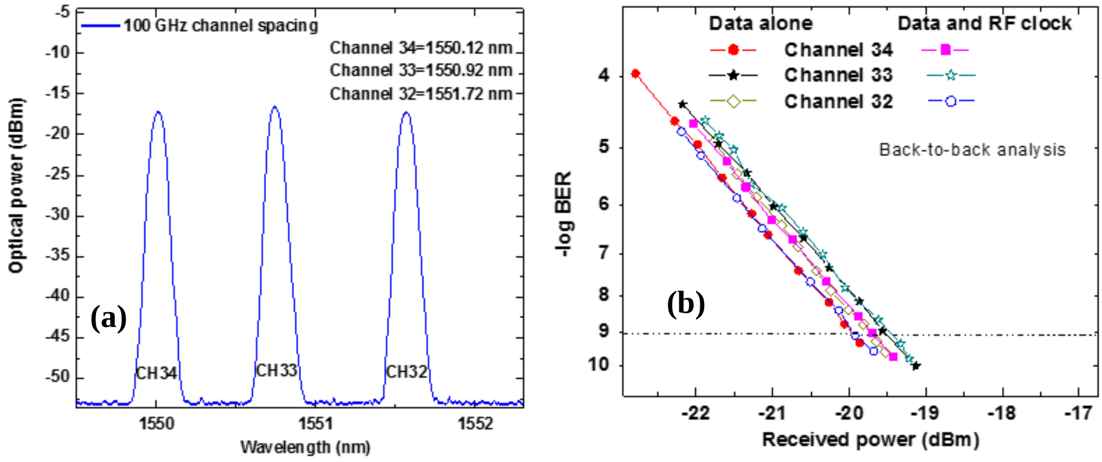

Fig 7.4: (a) optical signal spectrum at the transmitter side, (b) BER data analysis of WDM channels 34, 33, and 32 with and without reference clock signal at back-to-back analysis.

A receiver sensitivity of -19.95 dBm, -19.71 dBm and -19.52 dBm was attained for channels 34, 33 and 32 respectively without the phase modulated RF clock signal. This corresponded to a degradation penalty of 0.24 dB and 0.43 dB for channels 32 and 33 respectively. The receiver sensitivity values were measured at a threshold of BER= 10^{-9} for all the 3 multiplexed channels. The 4 GHz phase modulated RF clock signal per channel was noted to have no significant impact on quality performance of the 10 Gbps intensity modulated data signal, for all the channels analyzed as depicted in fig 7.4(b). These signals (10 Gbps data and 4 GHz reference frequency) were simultaneously modulated on two district attributes of the carrier signal (intensity and phase respectively) therefore no interference between the two modulated signals was expected.

The investigated channels also showed similar BER data performance trend, with and without the phase modulated RF clock signal. However, there was a slight performance degradation between the channels with channel 33 suffering the worst case. This performance degradation observed in channels 33 and 32 at the edge of the WDM de-multiplexed is attributed by several factors. Firstly, the in-passband insertion loss (dB) for the three investigated channels was not the same. The 8 channel WDM de-multiplexer had a passband insertion loss of 1.13 dB, 1.39 dB and 1.29 dB for channels 34, 33 and 32 respectively. In addition, channel 33 had an additional splice with a loss of 0.01 dB. This splice might have disoriented other key parameter of the channel i.e. polarization dependent loss and its return loss therefore contributing to its overall performance degradation compared to other channels. The respectively eye diagrams are shown in fig 7.5. A clear open eye was achieved for all the three channels. Eye clarity shows error free transmission.

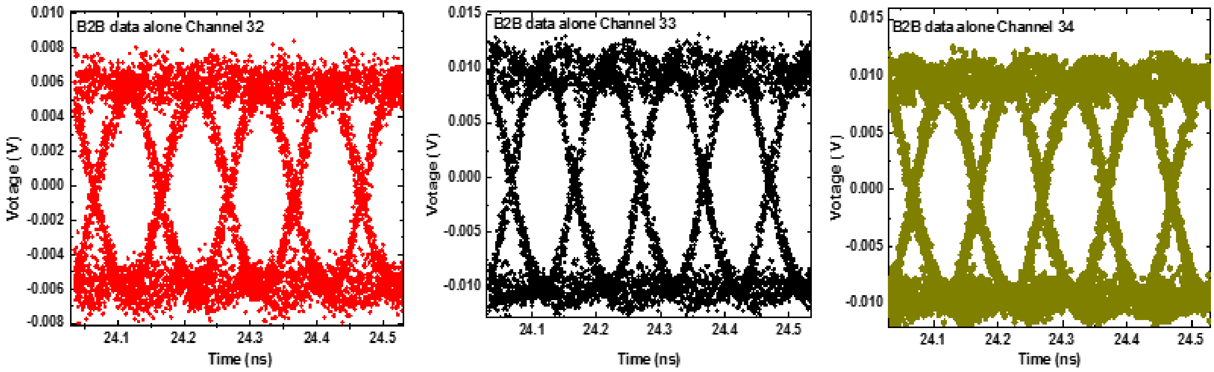

Fig 7.5: Back-to-back eye diagram for channels 32 (red), 33 (black) and 34 (green) respectively.

After a successful multiplex and modulation of the 3 channels at 100 GHz channel spacing to achieve simultaneous 30 Gbps data and 12 GHz reference frequency clock signal transmission, the link performance was analysed through BER measurement and eye diagram representation as depicted in fig 7.6. This can be regarded as a cost effective and efficient network upgrade scenario where a single Mach-Zehnder modulator is utilized to modulate several incoming wavelengths with a data and RF signals simultaneously and output into a single line, therefore increasing the network capacity and flexibility.

A 24.73 Km of SMF-RS fibre transmission length was experimentally achieved as shown in fig 7.6. OFS True Wave® RS low water peak (LWP) is a non-zero dispersion shifted fibre (NZDSF) optimised for 1550 nm transmission window that provides exceptional performance for dense wavelength division multiplexing (DWDM) used in optical transmission systems [256]. A transmission penalty of 0.18 dB, 0.25 dB and 0.20 dB was encountered on channels 34, 33 and 32 respectively over a 24.73 Km fibre transmission. An eye diagram for channel 32 is shown in the insert of fig 7.6. For demonstration purposes, only the eye diagram for channel 32 is shown. The eye diagrams remained clearly open at B2B analysis and 24.73 Km fibre transmission implying a successful transmission. The eye clarity was due to the high extinction ratio (ER) of the Mach-Zehnder modulator. The Mach-Zehnder modulator used in this study had an ER of 27 dB. ER is the ratio of the average power on the '0' and '1' levels of the eye diagram as measured by the values obtained from the spectrum analyser. The larger the ER, the wider the eye opening and the higher the quality of signal (QoS).

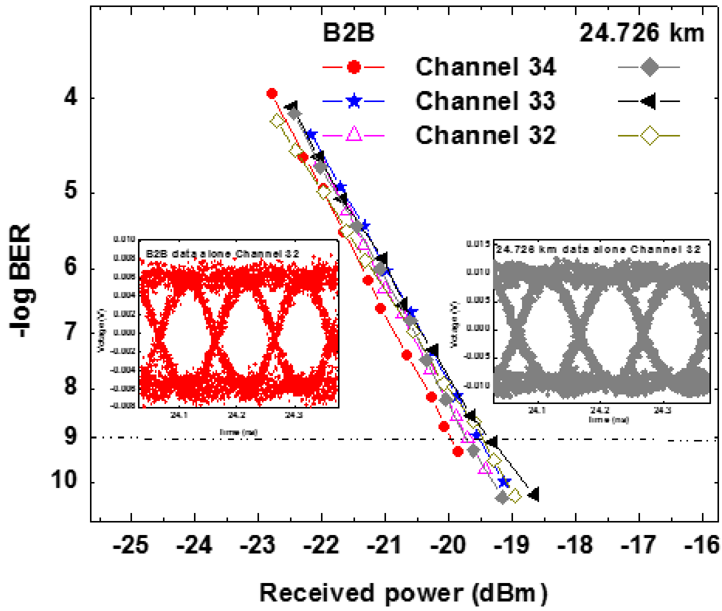

Fig 7.6: BER transmission curves for WDM channels 34, 33, and 32. Insert: Respective eye diagram for channel 32.

7.1.3 Stability performance analysis of simultaneous 12 GHz (3×4 GHz) WDM RF clock signal

The power spectrum analysis plot used for stability analysis of a 4 GHz phase modulated clock signals after successful multiplexing and modulation of the 3 channels (34, 33 and 32) at 100 GHz channel spacing to achieve simultaneous 30 Gbps (3×10 Gbps) data and 12 GHz (3×4 GHz) RF clock signal transmission is shown in fig 7.7(a). The power spectrum measurement in fig 7.7(a) were analyzed at back-to-back (B2B). A normal waveform from a signal generator with a nominal frequency of 4 GHz was modulated onto the phase of each multiplexed wavelengths and recovered using optical differential delay interferometry technique as discussed in section 7.1.1. A VBFZ-2000+ bandpass filter was used to filter out the electrical RF clock signal from the data signal before analysis of the individual channels.

This filter had a central frequency at 4000 MHz, and a passband of 3730-4270 MHz with an insertion loss of 2.3 dB. All the three channels had a similar power spectrum characteristic as shown in fig 7.7(a). The power spectrums in fig 7.7(a) showed a maximum peak at the nominal frequency of 4 GHz for all the channels. The central RF peak power for channels 34, 33 and 32 was -27.18 dBm, -31.71 dBm and -29.39 dBm respectively.

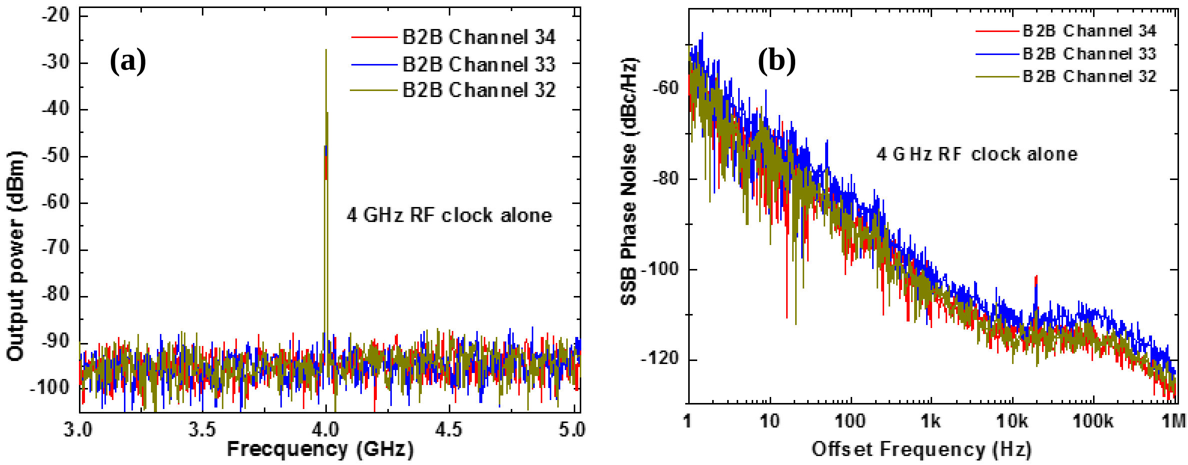

Fig 7.7: (a) Power spectrums for a phase modulated 4 GHz RF clock signal at B2B analysis, (b) single side phase noise (SSB) for a phase modulated 4 GHz RF-signal at B2B for channels 34 (red), 33 (blue) and 32 (green) respectively.

The corresponding phase noise plots for channels 34, 33 and 32 at B2B analysis are shown in fig 7.7(b). Phase noise is the most generic method of expressing frequency instability of an oscillator [263, 277]. The carrier frequency instability is expressed by deriving the average carrier frequency and then measuring the power at various offsets from the carrier frequency in a defined bandwidth. The result is then expressed as a logarithmic ratio compared to the total carrier power i.e. dBc/Hz. The power ratio is usually normalized to be the equivalent signal power present in a measurement bandwidth of 1 Hz. From results in fig 7.7(b), channels 34, 33 and 32 showed similar phase noise characteristics. The phase noise performance for channels 34, 33 and 32 had a smooth profile with very gradual change of slope with increasing offset frequency. At an offset of 100 Hz, a phase noise of -89.43 Bc/Hz, -83.36 dBc/Hz and -86.20 dBc/Hz was measured for channels 34, 33 and 32 respectively.

Fig 7.8(a) shows the corresponding phase noise plots at B2B analysis and after a successful 24.73 Km fibre transmission. For demonstration purpose, only channels 34 was considered for analysis. The phase noise levels after fibre transmission were generally higher than the

B2B, as would be expected due to the noise contribution of the fibre. As expected, the 10 Gbps per channel intensity modulated data signal was noted to have no significant impact on the phase noise of the 4 GHz per channel phase modulated RF clock signal as depicted by the phase noise plots in fig 7.8(a). These signals were simultaneously modulated on two distinct attributes of the carrier signal (intensity and phase respectively) therefore no interference between the two modulated signals was expected. Moreover, a bandpass filter with a passband of 3730-4270 MHz was used to filter out the data signal from the 4 GHz RF clock signal prior to its analysis.

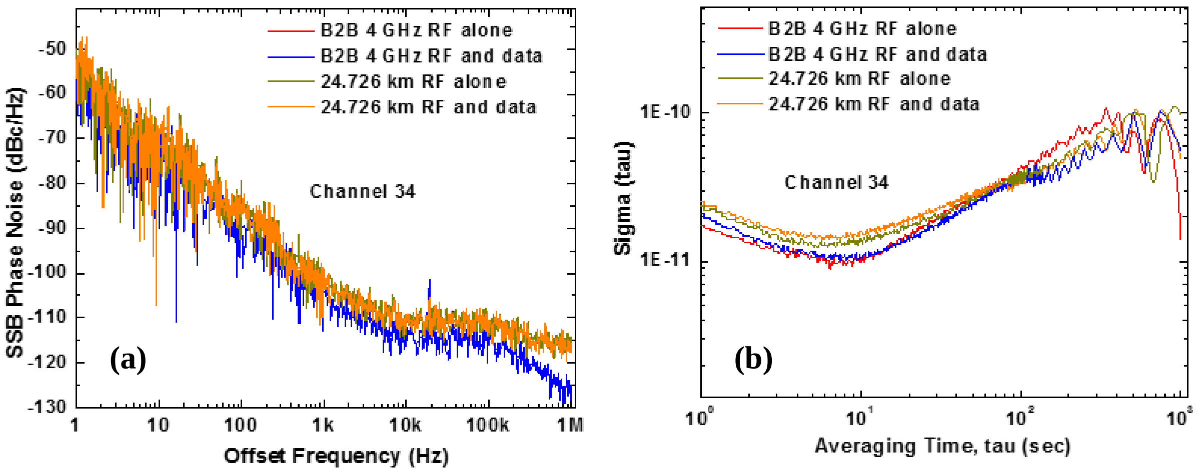

Fig 7.8: (a) Single side phase noise (SSB) for a phase modulated 4 GHz RF-signal for channel 34, (b) Allan deviation for a phase modulated 4 GHz RF-signal for channel 34.

The long-term stability measurement of the RF clock signal was analyzed and expressed using Allan deviation. Fig 7.8(b) shows the log-log plot of Allan deviation as a function of averaging time (sigma-tau) for channel 34. An Allan deviation of 1.0×10^{-11} and 1.08×10^{-11} was attained for B2B without and with intensity modulated data at 100 sec averaging time respectively. After a 24.73 Km fibre transmission, an Allan deviation of 1.4×10^{-11} and 1.53×10^{-11} was obtained without and with intensity modulated data at the same averaging time. The stability curves in Fig 7.8(b) also showed different slopes implying different noise sources cumulatively contributing to the overall instability of the RF signal. As depicted in Fig 7.8(b), the noise contribution over the first 100 secs of averaging time was different from the noise contribution after the first 100 secs. This can be seen clearly with the difference in gradient experienced between the two averaging time regions. At the first 100 secs of averaging time, the instability of the oscillator could be due to white noise. White noise has a slope τ^{-1} and is common in passive resonance mechanism of the oscillator. After the first 100 secs, random walk off noise with a slope of a τ^{1} dominated the noise contribution in this region. Random walk off noise is associated with the physical environment of the oscillator (vibrations, mechanical effect and temperature variation).

7.2 Simulation demonstration of 625 Gbps (25×25 Gbps) DWDM data transmission

Due to the need to demonstrate higher transmission data rates at much smaller channel spacing to maximize the optical fibre network capacity, OptiSytem simulations were used. A 25 Gbps data rate per channel and a total of 25 channels dense wavelength division multiplexing (DWDM) components at 50 GHz channel spacing which were not available for experimental demonstration were simulated.

7.2.1 Performance evaluation of 625 Gbps (25×25 Gbps) WDM Data signal

The simulation setup used to demonstrate 625 Gbps 25 channels DWDM data transmission is shown in fig 7.9. OptiSytem is a comprehensive software that enables its users to plan, test and simulate optical links in the transmission layer of modern optical networks [278]. A DWDM transmitter module was used to emulate the Agilent WDM laser source used in the experimental analysis demonstrated in section 7.1. The central frequency of the DWDM laser module was set at 1555 nm, channel number set to 25 while the channel spacing was adjusted to 50 GHz. The bitrate was set to 25 Gbps from the global parameters. This therefore created 25 channels starting from 1554.94–1546.11 nm, each of spacing 50 GHz and transmitting at 25 Gbps, therefore achieving a total multiplexed capacity of 625 Gbps. An extinction ratio of 30 dB was selected to emulate the high extinction ratio attained by the $LiNbO_3$ Mach-Zehnder modulator used in the experimental setup in section 7.1. The transmitter output optical power was set to 7 dBm. An ideal mux module with 25 ports was used to combine the different wavelengths into a single output and channeled into 18 Km of standard single mode fibre. The parameters of the fibre module (attenuation, dispersion, PMD coefficient and nonlinear effects) were adjusted to match those of the SMF-RS fibre used in the experimental demonstration.

At the receiver end, a variable optical attenuator module was used to vary the optical power leading to the de-multiplexer therefore emulating the optical losses within a deployed fibre network. A de-multiplexer module with 25 channels was used to separate the incoming light source into 25 respective separate channels for simultaneous performance analysis. An optical receiver module with complete photodiode (PIN), low pass filter and an electrical amplifier was attached to each channel, and a BER analyzer module attached to each optical receiver module for simultaneous individual BER performance analysis of all the 25 channels. For demonstration purposes, only channel 1 and 25 were considered for BER and eye diagram analysis.

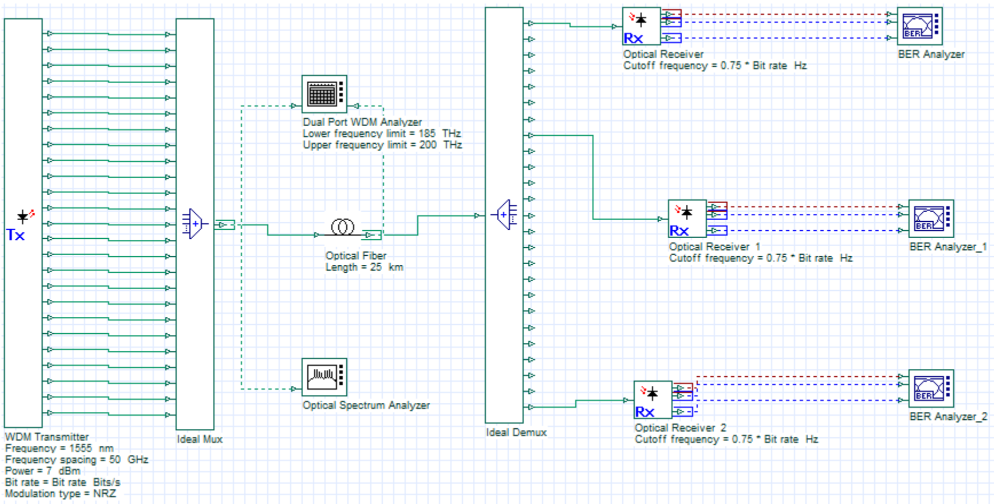

Fig 7.9: Simulation setup for 625 Gbps 25 channels DWDM data transmission system.

Fig 7.10(a) shows the simulated optical signal spectrum of the 25 multiplexed DWDM channels at the transmitter side. The 25 DWDM channels were spaced from 1545.38 nm to 1554.99 nm at 50 GHz spacing. Fig 7.10(b) shows BER curves for the simulated 625 Gbps 25 channels DWDM data transmission over 18 Km fibre length. For demonstration purposes, only channel 1 and channel 25 were considered for analysis. A receiver sensitivity of -23.19 dBm and -22.92 dBm was achieved for channels 1 and 25 respectively in this simulation. An 18 Km fibre transmission introduced a penalty of 1. 83 dB for channel 25. The difference in transmission performance between channel 1 and channel 25 is due to chromatic dispersion. Different wavelengths travel at different speeds within the optical fibre medium. Longer wavelengths travel faster that shorter wavelengths. This therefore spreads the pulse thus accounting for the penalty observed for channel 25 as depicted in fig 7.10(b). The respective eye diagrams for channels 1 and 25 at B2B and after 18 Km fibre transmission are shown in fig 7.11.

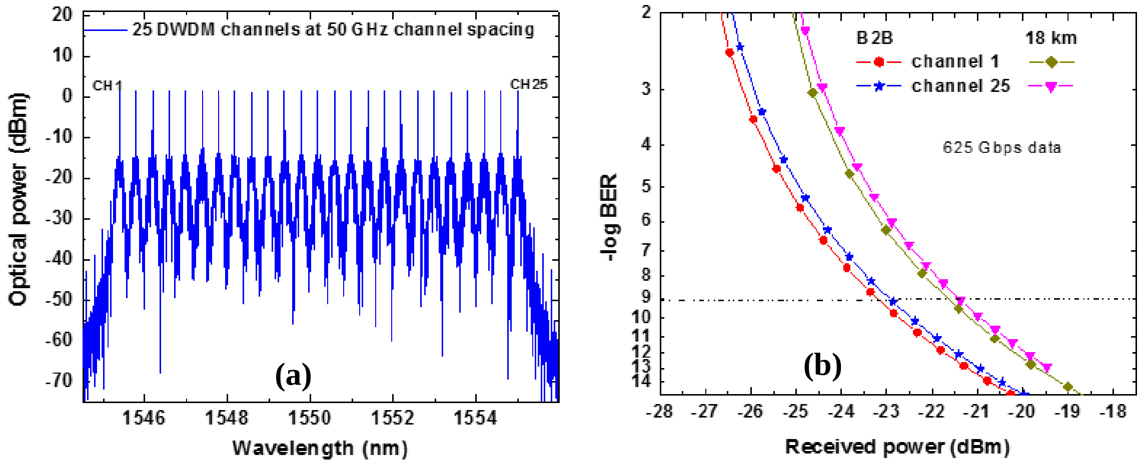

Fig 7.10: (a) optical signal spectrum of 25 channel DWDM transmitter, (b) BER curve for channels 1 and 25 at back-to-back and 18 Km.

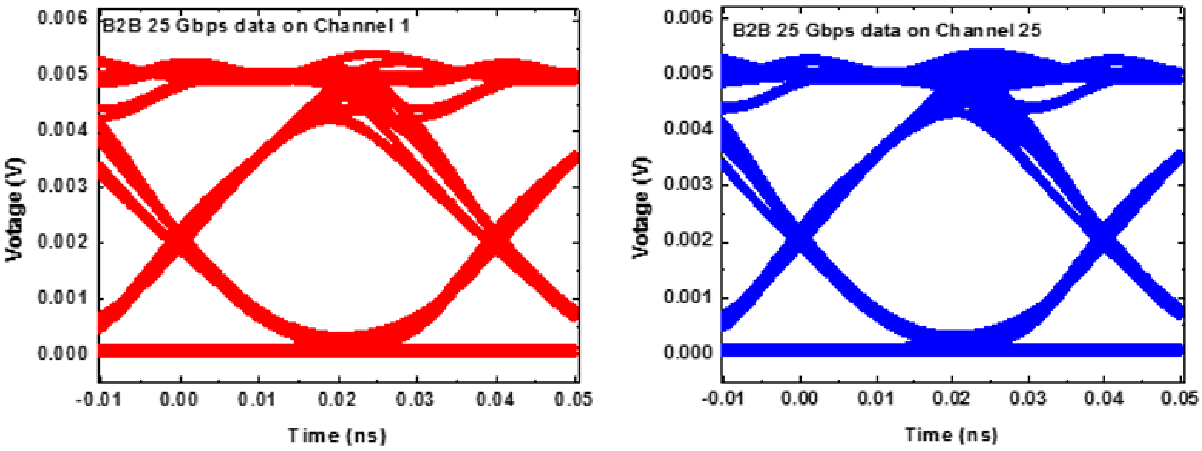

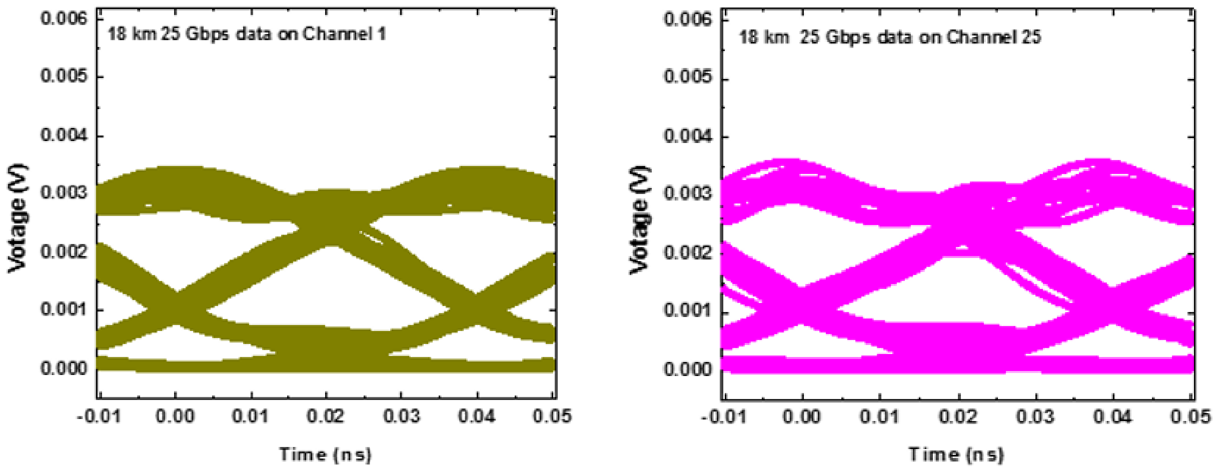

Fig 7.11: Eye diagrams of 25 Gbps data for channels 1 and 25 at B2B and after 18 Km fibre transmission.

7.3 Relevance of WDM and simultaneous data and reference clock signal transmission to telescope array networks

This section draws the relevance of simultaneous data and RF clock transmission in wavelength division multiplexing (WDM) solutions to astronomical telescope array networks such as the square kilometre telescope array network (SKA). Typical astronomical telescope array network resembles a point-to-point (P2P) passive optical network (PON). The SKA telescope array network is not an exception. Most commercially available WDM PON network are bidirectional point to multi-point (P2MP), supporting upstream and downstream simultaneous data transmission to and from the central office (CO) and the optical network units (ONUs) respectively. Upstream here refers to the connection and transmission from individual end users to the CO, while downstream refers to the transmission from the CO through the OLT to several end users at the ONU. An optical line terminal (OLT) is a single fibre span connecting the CO to the ONU. With the adoption of WDM, several channels can be multiplexed and transmitted in the OLT and de-multiplexed to serve multiples ONUs using combined WDM de-multiplexes and multiple optical splitters per channel. The multiple splitters per channel supports several ONUs ranging from 1: 8 up to 1:128 depending on the end-user demand. This therefore slices the available bandwidth to ensure network scalability and capacity upgrade.

SKA phase 1, the MeerKAT telescope array shares some similarities with a typical P2P PON network. The 64 receptor dishes can be equivalent of ONUs, while the CO replaced by the Karoo processing building (KAPB) at the Losberg site complex. The configuration of these receptors is dictated by the science observational objectives of the telescope [6, 28]. The core area of the MeerKAT is approximately 1 Km in diameter with 64 dishes concentration, therefore similar to a large short reach PON. The maximum baseline (longest distance between any two receptors) is 8 Km and the maximum length between KAPB and a single antenna is 12 Km. Fig 7.12 shows our proposed bidirectional WDM scheme for simultaneous data and RF clock transmission aimed at application in next-generation astronomical telescope array networks. As per our proposed scheme in fig 7.12, a single passive multiplexing/de-multiplexing device supporting up to 64 multiplexed channels can be installed in the middle of the core area of the SKA phase 1 telescope array to form a remote WDM multiplexing/de-multiplexing node as shown in fig 7.12. Each telescope element can then have a transmitting device (laser) to transmit the collected and digitized science data.

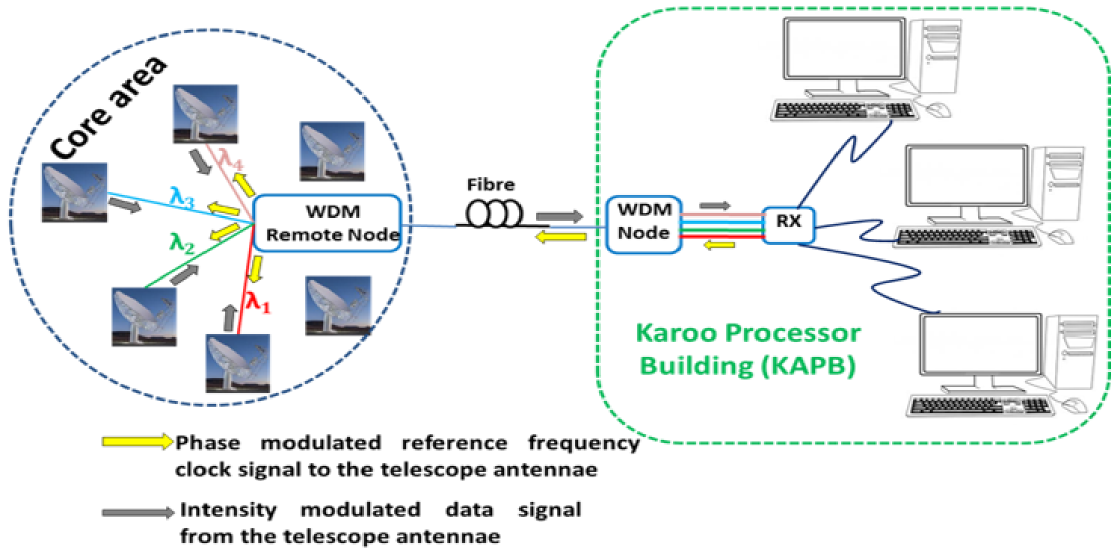

Fig 7.12: Illustration of a bidirectional WDM-based next-generation telescope array network.

The SKA phase 1 will collect up to 160 Gbps of science data per dish by 2018 [3, 28]. The lasers on each receptor can be intensity modulated with the science data and tuned to emit at different distinct wavelengths per receptor/dish. This will therefore allow each of the 64 antennae elements to act as distinct transmitters therefore transmitting the intensity modulated science data at distinct wavelengths. Each antennae element can be connected to a remote

WDM multiplexing/de-multiplexing node and assigned a distinct wavelength/channel based on the wavelength specification of its transmitting laser. This therefore will allow for convergence of science data from individual receptors at different wavelengths to be multiplexed and forwarded into a single output line. The individual multiplexed wavelengths can be transmitted over a single optical fibre to the KAPB for data storage and analysis. This will represent a downstream transmission over the OLT in typical PON systems. At the KAPB, individual channels can be de-multiplexed and intensity modulated science data from individual dishes retrieved for analysis and storage. At the KAPB, time and reference frequency clock signals can be simultaneously distributed to individual telescopes antennae elements. Time and reference frequency clock signals are important in the control and monitoring functions of the telescope. A single reference timing clock signal from the control unit at the KAPB can be broadcasted to the phase attribute of different transceiver modules at the WDM node located at KAPB. The RF timing clock to individual dishes can then be transmitted upstream to respective dishes thus allowing for bidirectional simultaneous science data and RF timing clock signal transmission in the SKA telescope network array as shown in fig 7.12.

Consideration of our proposed WDM-based scheme to achieve simultaneous bidirectional data and RF clock signal transmission in astronomical telescope array networks such as the SKA opens a new exciting field for concept generation and technology down selection. Our proposed technique allows several attractive features to next-generation telescope array networks. Firstly, reducing the number of fibres required in the telescope array network. Taking SKA phase 1 telescope array network for instance, a total of 170 Km of buried fibres will be required to connect different dishes to the KAPB individually. The scale of this project therefore poses a challenging task to the optical fibre communication community. However, with proper technological design to accommodate data and timing signal transmission through shared network infrastructure, the initial installation cost can be reduced significantly, reduce network complexity as well as increase the network efficiency, flexibility and capacity.

7.4 Summary

In this chapter, simultaneous data and reference frequency (RF) signal transmission in WDM systems for capacity and flexibility upgrade in terrestrial optical fibre systems like telescope array networks has been experimentally demonstrated. Simultaneous 30 Gbps (3×10 Gbps) WDM data transmission link with 12 GHz (3×4 GHz) phase modulated RF clock signal over a single mode optical fibre of length 24.73 Km has been achieved experimentally. A technique for RF clock signal recovery using a differential delay line interferometry has been demonstrated experimentally. Transmission and stability performance of the simultaneous 30 Gbps (3×10 Gbps) WDM data and 12 GHz (3×4 GHz) WDM phase modulated RF clock signal has been analyzed simultaneously through BER curves, phase noise measurement and Allan variance representation respectively. A 625 Gbps (25×25 Gbps) DWDM data transmission links has been developed in simulation and a fibre transmission length of 18 Km demonstrated. The relevance of WDM and simultaneous data and RF clock signal transmission to next-generation telescope array networks has been discussed.

The next chapter presents the first reported technique for capacity upgrade and spectral efficiency improvement in optical fibre networks we refer to as multi-signal modulation onto a single VCSEL carrier. A novel technique for maximizing carrier spectral efficiency through simultaneous 4-PAM data and phase modulated reference frequency (RF) clock signal transmission using a single mode 10 GHz bandwidth VCSEL carrier at 1310 nm is experimentally demonstrated. Data transmission and clock stability performance of the designed high spectral efficient VCSEL-based link network is evaluated through BER curve plots, phase noise measurement and Allan variance analysis respectively. A 120 Gbps 8-PAM data transmission link is simulated, and a 5 Km of single mode fibre transmission demonstrated.

Chapter 8

VCSEL-based multi-level pulse amplitude modulation (M-PAM) for simultaneous data and reference frequency clock signal transmission

To satisfy the ever-increasing needs of high capacity traffic, optical data communication systems based on vertical cavity surface emitting lasers (VCSELs) need to adopt more spectral efficient modulation formats. Over the recent past, different modulation techniques have been proposed for use with VCSELs [136, 143, 149, 165, 207, 279-281]. However, the high spectral efficiency of most of these higher order modulation formats come at a cost of increased complexity in receiver and transmitter architecture, higher requirements in signal-to-noise ratio as well as high power consumption due to increased receiver and transmitter circuit electronics. Four level pulse amplitude modulation (4-PAM) is a relatively simple, less complex higher order modulation format, where the network data rate is doubled by providing 2 transmitted bits per symbol [62, 191, 200, 202, 220, 281-289].

In this chapter, a 4-PAM data modulation format employing VCSELs is experimentally demonstrated for adoption in high bitrate optical communication systems such as big data science projects and as well as data Centre networks (DCNs). A digital signal processing (DSP) receiver is designed and implemented in MATLAB to recover the transmitted 4-PAM data signal cost effectively therefore avoiding costly receiver hardware. A novel technique for maximizing carrier spectral efficiency through simultaneous 20 Gbps 4-PAM data and phase modulated 2 GHz reference frequency (RF) clock signal transmission on a single mode 10 GHz bandwidth VCSEL carrier at 1310 nm is reported for the first time to the best of our knowledge. The quality of the transmitted data as well as clock stability performance of the designed high spectral efficient VCSEL-based link network is evaluated simultaneously through BER curve plots, phase noise measurement and Allan variance analysis respectively. A high capacity 120 Gbps 8-PAM data transmission link is further implemented in simulations using Optisystem software and a 5 Km fibre transmission reach attained.

8.1 Experimental demonstration of direct VCSEL Modulation with 20 Gbps 4-PAM data signals

The experimentally measured VCSEL bias characteristics curve for 4-PAM data signal modulation optimization is shown in fig 8.1. It was necessary to measure the bias characteristics of the VCSEL carrier prior to its modulation with a 4-PAM data signal to determine the ideal bias point of the laser. This was meant to ensure effective accommodation of all the four-level data signals for its ideal performance as shown in fig 8.1. When directly modulating a VCSEL carrier with 4-PAM data signals, the 1-level PAM symbol, is generated by biasing the VCSEL with current I_{bias} as shown in fig 8.1. It should be noted that if a VCSEL is modulated with a 4-PAM data signal and operated at a bias point too close to the threshold, unwanted chirp is introduced which can distort the signal through dispersion [149].

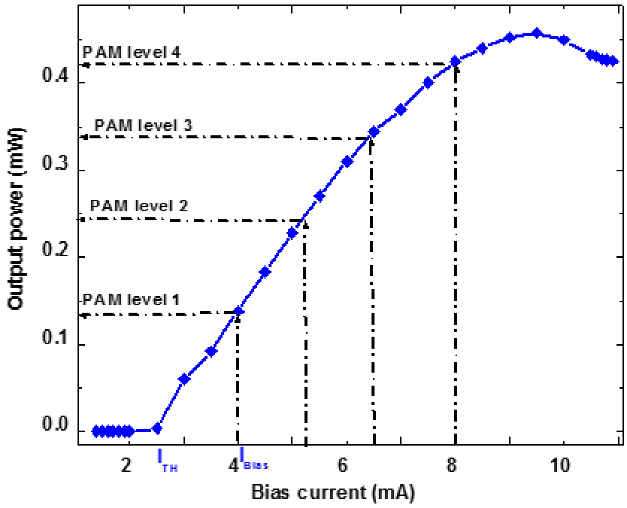

Fig 8.1: Experimentally measured VCSEL bias characteristics curve.

An experimentally measured eye diagram representation of a 20 Gbps 4-PAM data signal is shown in fig 8.2. Discrete data bits are encoded to the PAM symbol while ensuring that they do not differ by more than a bit period, therefore minimising errors. As shown in fig 8.2, individual PAM levels are generated by different drive voltages.

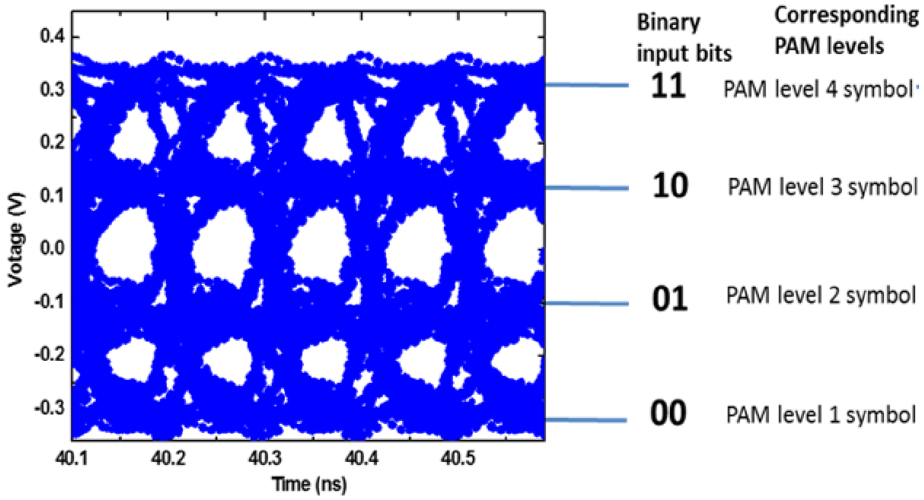

Fig 8.2: Experimentally measured electrical 20 Gbps 4-PAM eye diagrams.

8.2 Mach-Zehnder modulator (MZM) bias characteristics

An experimentally measured transfer function of a Mach-Zehnder Modulator (MZM) showing its static extinction characteristics at different wavelengths is shown in fig 8.3. The bias voltage control unit of the MZM device was changed from automatic mode to manual mode, to enable the bias voltage to be varied from -8 V to 8 V as the corresponding output power was measured using an optical power meter.

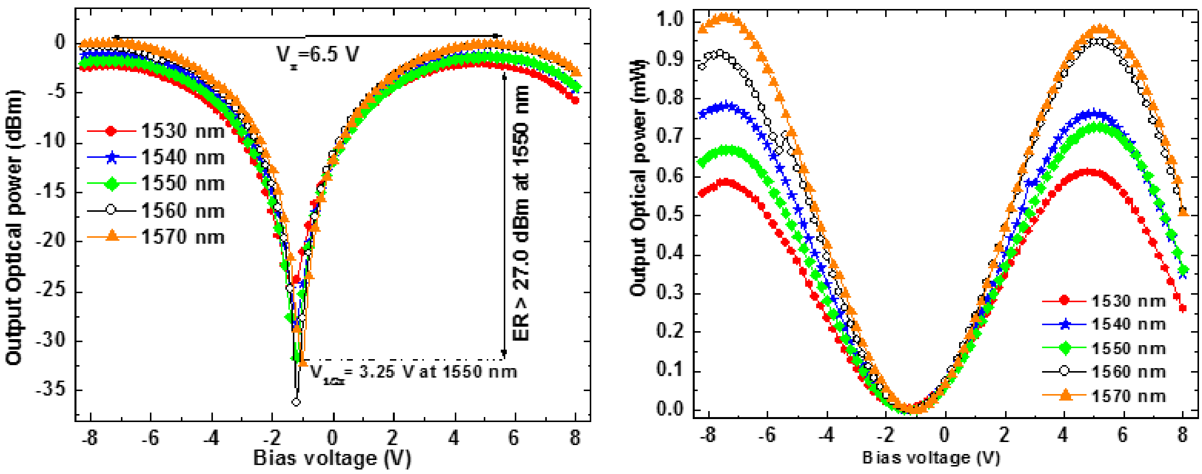

Fig 8.3: Experimentally measured transfer function of a Mach-Zehnder modulator showing static extinction characteristics at different wavelengths.

The MZM used in this work was a 40 G phase and amplitude lithium Niobate ($LiNbO_3$) modulator from Photline technologies company [290]. The measured output optical power with varying bias voltage was plotted for different input wavelengths from 1530 nm – 1570 nm as shown in fig 8.3.

We first examined the extinction characteristics of a MZM at different wavelengths as shown in fig 8.3. A half-wavelength voltage $V_{\pi/2}$ of approx. 3.25 V and a high extinction ratio (ER) of over 27 dB were experimentally attained for the entire C-band region (1530 nm – 1570 nm) when the applied dc voltage was about 8 V. As shown in fig 8.3, the extinction curves at different wavelengths were completely symmetrical and identical. These symmetrical characteristics indicate that the excess loss caused by voltage-induced absorption or electro absorption (which is wavelength dependent) was negligible [274, 275, 291].

Results in fig 8.3 reveal that the MZM device has satisfactory characteristics for use in advanced modulation formats such as optical duo binary and differential phase shift keying signals. Moreover, it is true that the $V_{\pi/2}$ value depends on both bias voltage and wavelength. This is because the change of refractive index of semiconductor material depends on the wavelength detuning between the bandgap wavelength and the input signal wavelength [292]. From fig 8.3, it is also true that an increase in the bias voltage resulted to the transfer function to move in a horizontal direction since a MZM is not perfectly balanced. Moreover, it is subject to drifts caused either by thermal changes, thermal inhomogeneity, aging, photo reflective effects and static electrical change accumulation [275]. This drift is the one responsible for the transfer function to move in a horizontal direction. The bias voltage applied to the MZM dc electrodes is supposed to select the desired operating point of the modulator, therefore compensating for the possible modulator drift and locking the device operating point to keep a stable operation conditions. This bias voltage can be supplied by a simple voltage source and manually adjusted so as the desired operating point is reached. However, in such a condition, the voltage must be readjusted manually in case of any drift of the modulator. However, for long-term operation and especially in all systems that must operate over changing environmental temperature conditions, the MZM should be operated in an automatic mode. In the automatic mode operation, an automatic bias control circuit permanently supplies the right dc voltage and locks the selected operating point. In this work, the MZM was operated in an automatic mode throughout the experiment.

8.3 Experimental demonstration of simultaneous 20 Gbps 4-PAM data and phase modulated 2 GHz clock signal transmission on a single VCSEL Carrier

A complete experimental setup used to demonstrate simultaneous 20 Gbps 4-PAM data and phase modulated 2 GHz RF clock signal modulation on a single mode 10 GHz bandwidth VCSEL carrier is shown in fig 8.4. The P and N electrical arms of the PPG were combined to generate a 20 Gbps pseudo random bit sequence (PRBS) 4-PAM level signal used to directly modulate the VCSEL through its bias-tee.

Different electrical attenuators were used on each electrical arm to ensure that the two data signals were at an appropriate modulation levels as shown in fig 8.4. The N data output arm was attenuated by 13 dB while the P electrical arm was attenuated by 6 dB using electrical attenuators, and delayed by one data bit period (100 ps) for correlation. The data signals from the two electrical arms (N and P) were then combined producing a 4-level PAM data sequence therefore doubling the data rate from 10 Gbps to 20 Gbps. The 20 Gbps 4-PAM transmitter therefore coded two bits per symbol prior to its modulation and transmission. A second signal, a 2 GHz RF clock signal from a signal generator was simultaneously modulated onto the phase attribute of the VCSEL carrier using a Mach-Zehnder modulator.

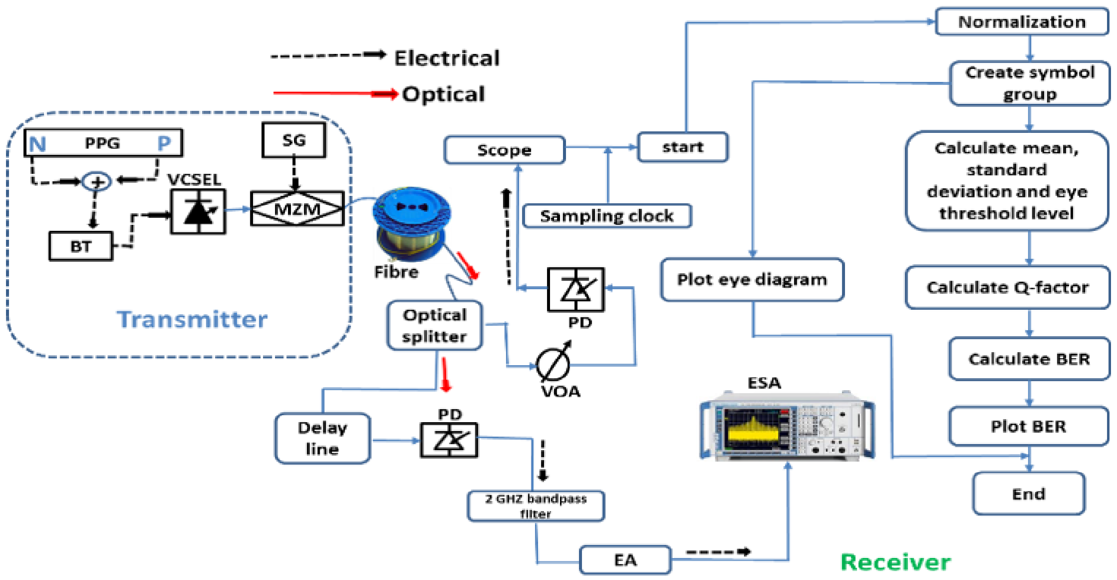

Fig 8.4: Experimental setup used to demonstrate simultaneous 4-PAM data and 2 GHz phase modulated clock signal over a single VCSEL carrier: VOA-variable optical attenuator, PIN-positive intrinsic negative photodiode, PPG- Programmable pattern generator, LDC- laser

diode controller, BT-bias Tee, MZM-MachZehder modulator, BERT-bit error rate tester and ESA-electrical spectrum analyser.

A single mode 10 GHz bandwidth VCSEL carrier at 1310 nm was therefore simultaneously modulated with a 20 Gbps 4-PAM data and phase-based 2 GHz RF clock signal. The simultaneously modulated 20 Gbps 4-PAM data and 2 GHz phase modulated RF clock signal were transmitted over a G. 652 single mode fibre of length 3.21 Km. At the receiver end, an optical signal splitter was used to split the incoming optical signal for simultaneous recovery and analysis of the transmitted 20 Gbps 4-PAM data and 2 GHz RF clock signals. To begin with, a variable optical attenuator was used after the splitter to vary the optical power received by the PIN photodiode for BER performance analysis of the direct modulated 20 Gbps 4-PAM data signal. The received 20 Gbps 4-PAM data signal was then captured by an Agilent sampling oscilloscope and analysed offline through digital signal processing (DSP) receiver circuits developed in MATLAB as reported in our recent contribution in [218], thus avoiding costly and power consuming receiver hardware.

Consequently, due to unavailability of a phase sensitive photodiode in our laboratory, it was necessary to develop a reliable technique that could recover the simultaneously phase modulated reference frequency clock tone from the phase attribute of the VCSEL carrier to intensity, for its detection with an intensity sensitive PIN photo receiver that was readily available in the laboratory. To achieve this, a differential delay interferometric technique was adopted using an optical differential delay line as discussed in chapter 7 section 7.1.1, and by our work in [293]. A 14.32 picosecond differential delay time was adopted using this technique.

This allowed for the phase modulated RF clock signal to interfere both constructively and destructively upon coupling, therefore leading to a sinusoidal wave with high and low voltage, detectable by an intensity sensitive PIN photodiode. A 1500-2500 MHz bandpass filter was used to separate the 2 GHz RF clock signal from the 20 Gbps 4-PAM data signal for its stability analysis. The bandpass filter had a central frequency of 2000 MHz and a passband loss of < 2.4 dB. A 0.1-18 GHz wideband electrical linear amplifier was used to boost the filtered electrical signal before its stability analysis. This amplifier had a typical high flat gain of 27 dB. A direct method using an electrical spectrum analyzer was adopted for RF clock stability measurement due to its low complexity, reproducibility and accuracy [294]. The stability of the received RF clock signal was analyzed through phase noise and Allan variance plots.

8.3.1 Maximizing carrier spectral efficiency

Next-generation high speed optical communication systems will require modulation techniques that will '*squeeze*' as much information as possible into least amount of spectrum possible. That objective is what is referred to as spectrum efficiency. Spectral efficiency is a measure of how fast information can be transmitted over an assigned bandwidth in a specific communication system. Several techniques have been proposed to maximize spectral efficient in communication systems [167]. The simplest of them all is the on-off keying (OOK) [295]. OOK has carrier waves with two amplitude levels represented as bits '0' and '1' of the modulation signal. However, the OOK modulation format is limited to a low spectral efficiency. OOK is only one-dimensional modulation scheme therefore provides a spectral efficiency of 1b/s/Hz only [282]. For instance, considering the 10 Gbps VCSEL carrier used in this work with a bandwidth of 10 GHz. If we directly modulated this VCSEL with a 10 Gbps data signal in the OOK modulation context, the pulse generated are '0' or '1', therefore 1 bit every pulse. Considering the bandwidth of the VCSEL carrier used the spectral efficiency ($\mathrm{SP_{eff\_OOK}}$) will be expressed:

$$\mathrm{SP_{eff\_OOK}} = \frac{1\mathrm{bit} \times 10\mathrm{Gbps}}{10\mathrm{GHz} \times 1\mathrm{sec}} = 1\mathrm{b/s/Hz} \qquad 8.1$$

Multilevel pulse amplitude modulation (N-PAM) modulation format is an upgrade version of OOK but with more than two amplitude levels. The extra levels therefore increase the carrier spectral efficiency significantly as more bits are coded per symbol. In N-PAM modulation technique where N is the number of signal levels, the number of bits coded per symbol is given as $N = 2^b$, where b is the number of bits coded per symbol (4-PAM = 2 bits/symbol, 8-PAM = 3 bits/symbol, 16-PAM = 4 bits/symbol). The spectral efficiency of N-PAM depends on the number of symbols coded. Spectral efficiency in N-PAM systems in given as:

$$SP_{eff\_4\text{-}PAM} = (\log_2 N)\frac{bits}{s}/Hz = 2b/s/Hz \qquad 8.2$$

In this work, two data bits per symbol were transmitted using the 4-PAM format and another 2 GHz reference clock signal simultaneously transmitted on the phase attribute of the VCSEL carrier. The overall aggregated spectral efficiency of our proposed scheme can be calculated as:

$$SP_{eff\_Total} = \left[(\log_2 4) \frac{bits}{s} /Hz \right] + \left[\frac{1bit \times 2Gbps}{10GHz \times 1\sec} \right] = 2.2b/s/Hz \qquad 8.3$$

The first part of equation (8.3) gives the spectral efficiency of the directly modulated 20 Gbps 4-PAM data signal, which was calculated to be 2 b/s/Hz. The second part of equation (8.3) shows that by modulation the phase attribute of the VCSEL carrier with a 2 GHz RF clock signal, a spectral efficiency of 0.2 b/s/Hz is attained. Therefore, by combining the two (4-PAM and phase modulation) to simultaneously transmit a 20 Gbps 4-PAM data and a 2 GHz phase modulated clock signal using a single VCSEL carrier as per our proposed scheme, the aggregated spectral efficiency per single channel is significantly upgraded to 2.2 b/s/Hz as reported in our contribution in [219].

8.3.2 Stability analysis of simultaneously modulated 2 GHz clock signal

The experimentally measured Allan deviation plots as a function of averaging time (sigma-tau) for simultaneous 2 GHz RF and 20 Gbps 4-PAM data signal at back-to-back analysis and 3.21 Km fibre transmission is shown in fig 8.5. An Allan deviation of 3.96×10^{-12} and 5.350×10^{-12} was attained for B2B without and with 20 Gbps 4-PAM data at 100 sec averaging time respectively as shown in fig 8.5. From the stability curves in fig 8.5, different slopes were noted implying different cumulative noise contributions arising from different sources as discussed in section 7.1.3 and in our contribution in [293]. The respective power spectrums are shown in fig 8.6.

Optical reference frequency signal stability is a key requirement in telescope array networks such as SKA. Short term reference clock stability is required for proper control performance of signal to noise degradation during data digitization process. Consequently, long term reference clock stability is a key requirement for applications such as very large baseline interferometry (VLBI) and certain kinds of astronomical observation such as pulsar work [3].

A complete table showing reference frequency requirements for different observational objective in the SKA telescope array is shown in table 2.1.

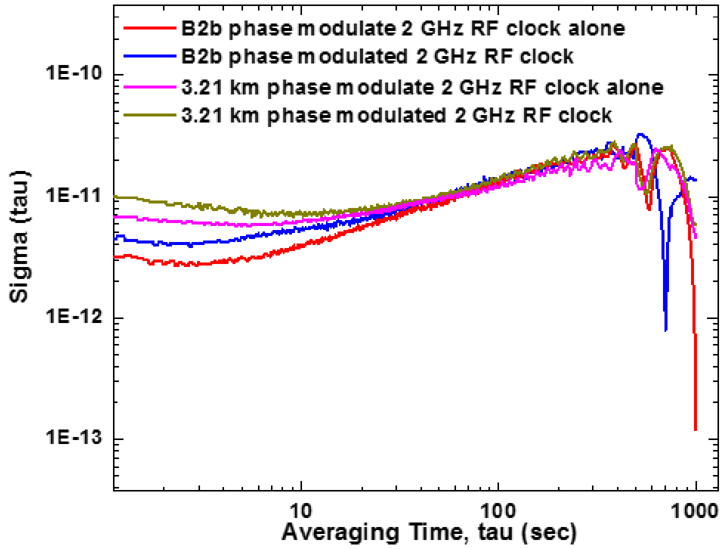

Fig 8.5: The measured fractional frequency stability of a 2 GHz phase modulated clock signal at B2B RF clock signal alone (red), B2B simultaneous RF signal and 4-PAM data(blue), 3.21 Km RF clock signal alone (magenta), 3.21 Km simultaneous RF clock signal alone.

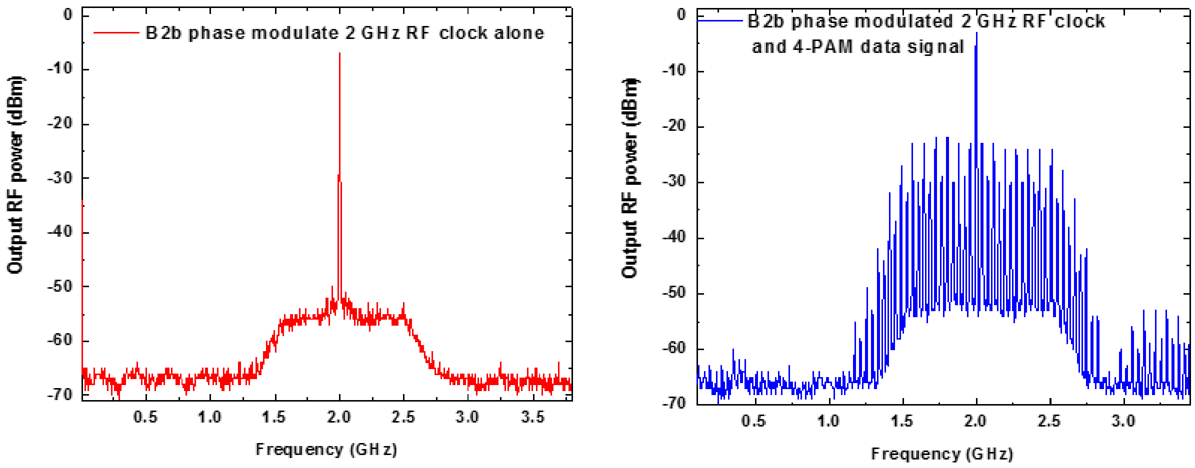

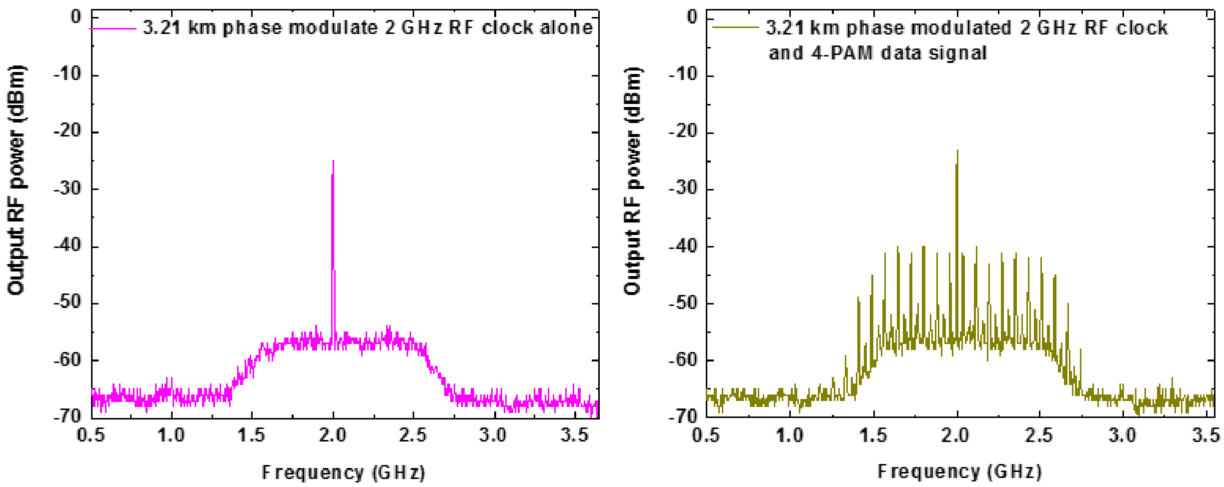

Fig 8.6: Power spectrums for a phase modulated 2 GHz RF clock signal at B2B RF clock signal alone (red), B2B simultaneous RF signal and 4-PAM data (blue), 3.21 Km RF clock signal alone (magenta), 3.21 Km simultaneous RF clock signal alone (green).

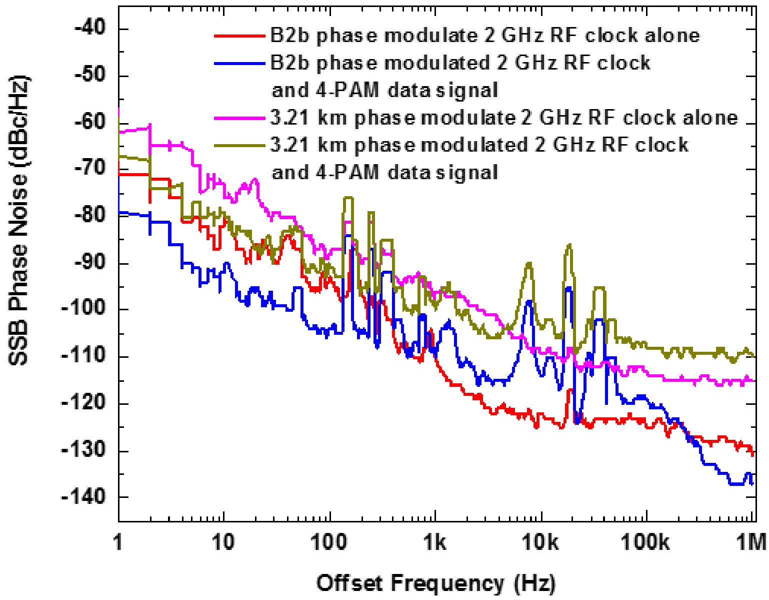

Fig 8.7: Single side phase noise (SSB) for a phase modulated 2 GHz RF-signal at B2B RF clock signal alone (red), B2B simultaneous RF signal and 4-PAM data(blue), 3.21 Km RF clock signal alone (magenta), 3.21 Km simultaneous RF clock signal alone (green).

The RF clock signal short term performance is shown in fig 8.7 as phase noise plots. The vertical axis is amplitude relative to the carrier (which is not shown), while the horizontal is frequency offset from the carrier. A single side band phase noise of -80.05 dBc/Hz,

-77.90 dBc/Hz, -76.05 dBc/Hz and -67.87 dBc/Hz was attained for back-to-back RF clock signal alone, back-to-back simultaneous RF clock signal and 4-PAM data, 3.21 Km RF clock signal alone and 3.21 Km simultaneous RF clock signal and 4-PAM data respectively as shown in fig 8.7. The single side phase noise results in fig 8.7 remained in the range of a few hundreds of decibels per hertz relative to the carrier frequency, for the different configurations demonstrated.

8.3.3 Transmission performance analysis of simultaneously modulated 20 Gbps 4-PAM data signal

Fig 8.8(a) shows the pattern of the two P and N arms of a pseudo-random pattern generator each with 10 Gbps data. As depicted in Fig 8.8(b), the two arms were attenuated differentially before combining to double the network data rate to from 10 Gbps to 20 Gbps as discussed in section 8.3. Fig 8.8(b) shows the resultant pattern of a 20 Gbps 4-level PAM data signal after combining the two data arms, and modulating the resultant 20 Gbps 4-PAM signal onto a VCSEL carrier. The generated 20 Gbps 4-PAM data signal comprised four symbols, each with two bits per symbol (0 0; 0 1; 1 0 and 1 1), therefore doubling the aggregated bit rate. The graph in fig 8.8(b) clearly shows that the combined 4-PAM signal (blue) was a result of the addition of the two individual signals (red and green).

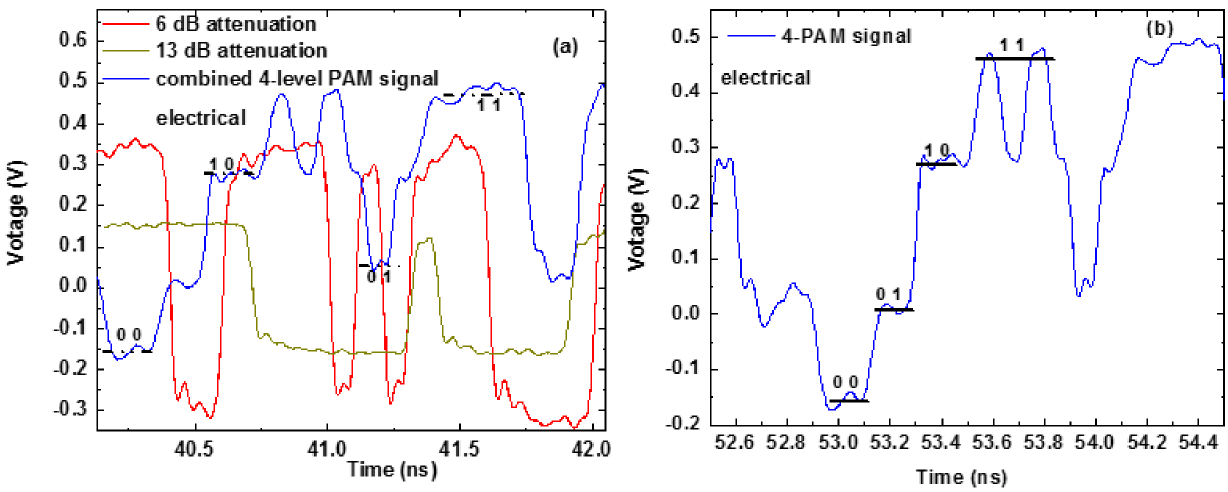

Fig 8.8: Experimentally measured electrical individual and combined waveforms of N and P arm data signals (a), experimentally measured electrical 4-level PAM data signal showing the four data levels of the signal.

After doubling the data rate of the VCSEL-based link using a 20 Gbps 4-PAM signal, the transmission link performance was analysed at back-to-back (B2B) and after 3.21 Km of G. 652 fibre transmission as depicted in fig 8.9.

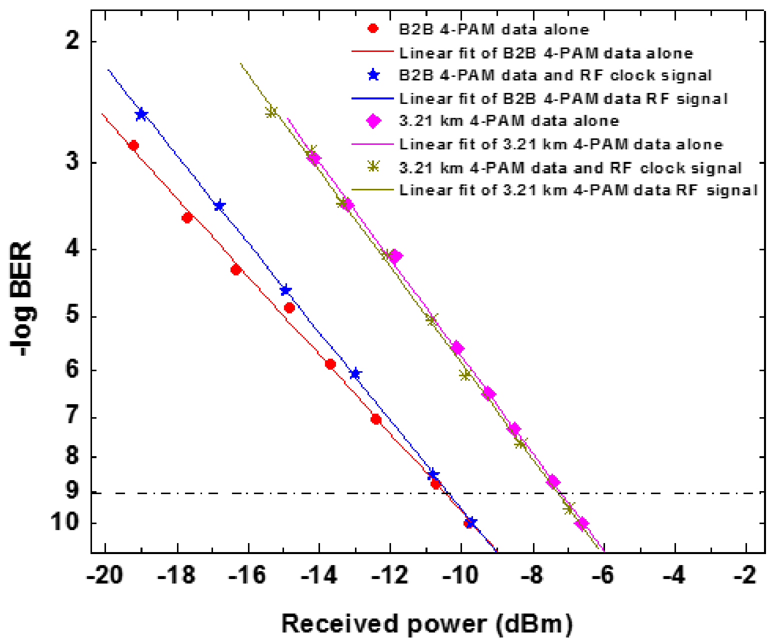

Fig 8.9: Bit error rate (BER) curve for VCSEL 20 Gbps 4-PAM data signal at B2B data signal alone (red), B2B simultaneous 4-PAM data 2 GHs RF clock signal (blue), 3.21 Km data signal alone (magenta), 3.21 Km simultaneous 4-PAM data 2 GHz RF clock signal (green).

This can be regarded as an upgrade scenario where a classical 10 Gbps on off keying (OOK) is upgraded to a 20 Gbps high-speed data transmission system using a 4-PAM system without replacing the VCSEL carrier. At a B2B analysis, a receiver sensitivity of -10.52 dBm and -10.34 dBm was attained without and with a 2 GHz phase modulated RF clock signal respectively as shown in fig 8.9. The receiver sensitivity value was measured at a communication threshold of BER= 10^{-9}. A 3.21 Km fibre transmission was noted to introduce a maximum penalty of 4.02 dB as shown in fig 8.9. This penalty was mainly due to the inter symbol interference (ISI) at such high bit rate. Though the ISI limited the attained transmission reach to 3.21 Km, this reach was still suitable for high-speed short reach optical fibre network applications. From results in fig 8.9, the 2 GHz phase modulated RF clock signal was noted to have no significant impact on the quality performance of the 20 Gbps 4-PAM directly modulated data signal as depicted in fig 8.9. This is because these signals (20 Gbps 4-PAM data and 2 GHz RF) were simultaneously modulated on two district attributes of the carrier (intensity and phase respectively), therefore no interference between the two modulated signals was expected.

The respective eye diagrams for the simultaneous 20 Gbps 4-PAM data and 2 GHz phase modulated RF clock signal are shown in fig 8.10.

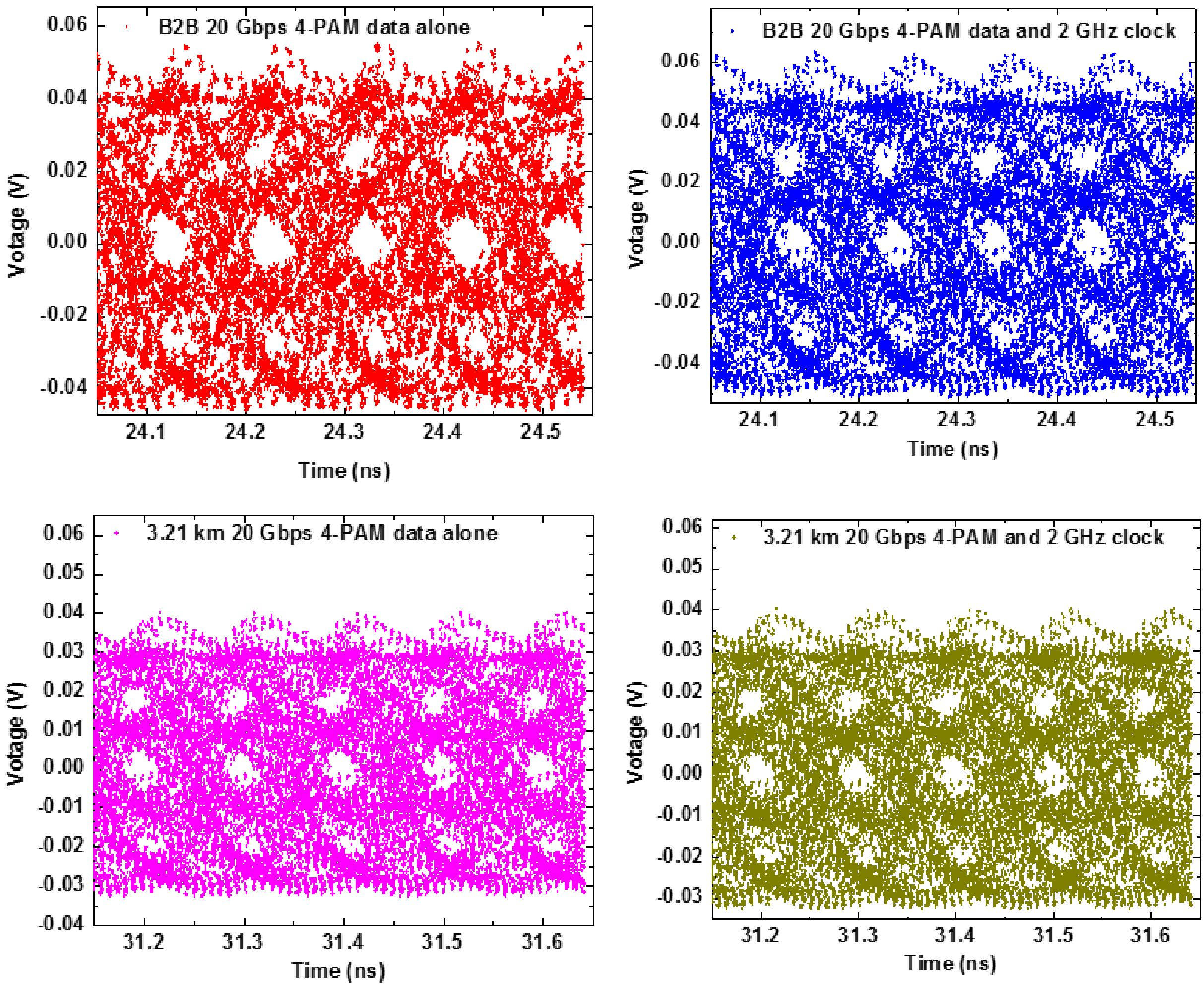

Fig 8.10: Eye diagram for VCSEL 20 Gbps 4-PAM data signal at B2B data signal alone (red), B2B simultaneous 4-PAM data 2 GHz RF clock signal (blue), 3.21 Km data signal alone (magenta), 3.21 Km simultaneous 4-PAM data 2 GHz RF clock signal (green).

These measurements were collected at a communication threshold of BER=10^{-9} using an Agilent sampling scope. As seen in fig 8.10, the eye voltages (V) of the 20 Gbps 4-PAM data signal (red) and the simultaneous 4-PAM data 2 GHz RF clock signal (blue) at B2B analysis remained at the same level. The eye diagram also remained clearly open after a 3.21 Km fibre transmission implying that the PIN receiver could clearly distinguish between the 0 0, 0 1, 1 0 and 1 1 multi-level bits therefore minimizing bit errors.

8.4 Simulation demonstration of 120 Gbps 8-PAM data transmission

To demonstrate high capacity data transmission using higher level PAM formats that could not be readily realized experimentally in our lab environment, computer simulations using OptiSytem software version 7.1 were applied. Fig 8.11 shows the simulation setup used to demonstrate 120 Gbps 8-PAM data transmission fibre system.

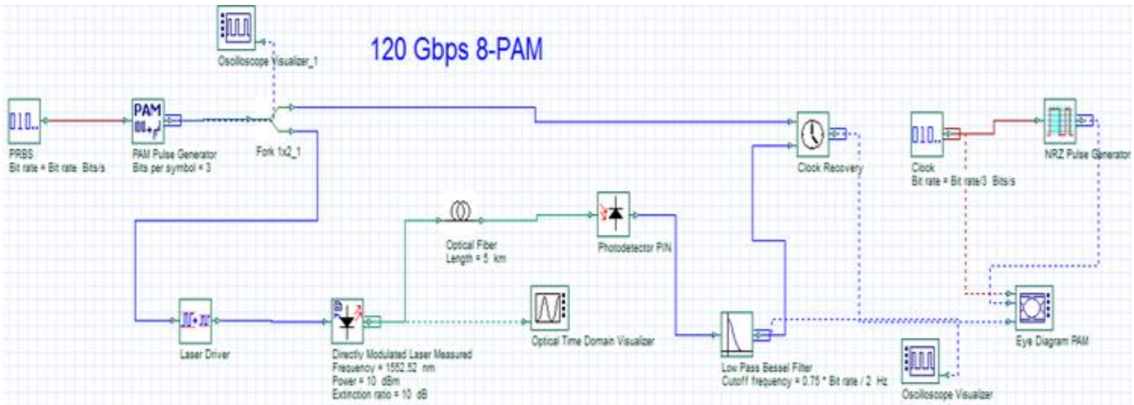

Fig 8.11: Simulation setup for 120 Gbps 8-PAM data transmission system.

A directly modulated laser (DML) module was used to emulate the VCSEL laser used in the experimental demonstration discussed in section 8.3. The central frequency of the WDM laser module was set at 1552.52 nm, output power to 10 dBm and the extinction ratio adjusted to 10 dB. A PRBS module was used to generate an electrical data signal at a bit rate of 40 Gbps. The high-speed data was modulated onto the DML laser module using a PAM pulse generator module. This module was used to code 3 bits per symbol high speed data therefore upgrading the transmission link into 120 Gbps 8-PAM data transmission system. The high capacity 120 Gbps 8-PAM data were transmitted over a single mode fibre of length 5 Km. The parameters of the fibre module (attenuation, dispersion, PMD coefficient, attenuation, linear and nonlinear effects) were adjusted to match those of the SMF-RS fibre used in the experimental demonstration. On the receiver end, a PIN photodiode module was used to recover the data signal from the received optical signal. An eye diagram PAM receiver module was used to plot the eye diagram of the recovered 120 Gbps 8-PAM data signal as shown in fig 8.11.

8.5 Transmission performance of the simulated 120 Gbps 8-PAM data transmission link

Transmission performance of the simulated 120 Gbps 8-PAM data transmission system over an SMF of length 5 Km is analyzed using the eye diagrams and data patterns as collected by the eye diagram PAM receiver module. Fig 8.12 shows a back-to-back data pattern (blue) of the simulated 120 Gbps 8-PAM. The back-to-back data pattern (blue) results in fig 8.12 shows that 8-PAM can be used to triple the data rate of a transmission link by providing 8 distinct amplitude levels, with three bits per symbol (000, 001, 010, 011, 100, 101, 110 and 111) using the same network infrastructure. The pattern amplitude (a.u) after 5 Km fibre transmission had a slight reduction compared to that at B2B. This was due to attenuation of the optical fibre medium which increases with fibre length.

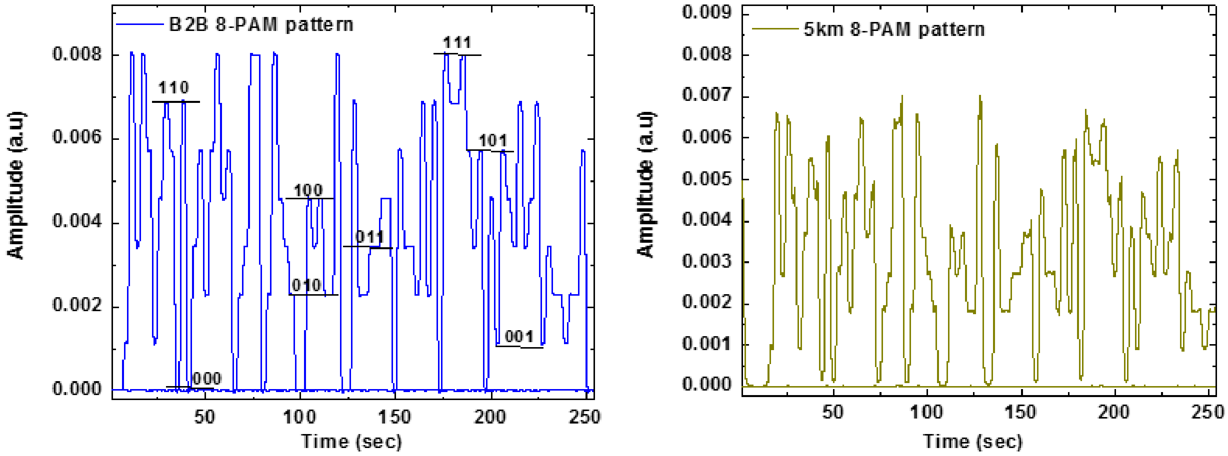

Fig 8.12: Simulated pattern for 120 Gbps 8-PAM data signal at back-to-back analysis (blue) and after 5 Km fibre transmission (green).

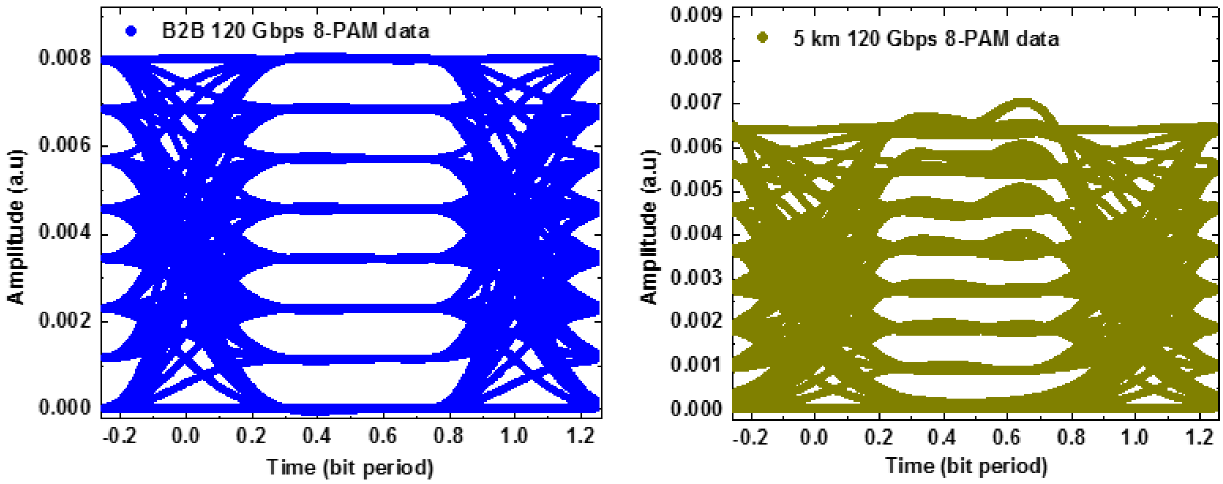

Fig 8.13: Simulated eye diagrams for 120 Gbps 8-PAM data signal at back-to-back analysis (blue) and after 5 Km fibre transmission (green).

The 120 Gbps 8-PAM eye diagrams at back-to-back analysis (blue) and 5 Km fibre transmission (green) are shown in fig 8.13. A set of 7 clearly open eyes were observed at B2B analysis. A clear and open eye with a high extinction ratio illustrates a clean signal and therefore implies an error-free transmission. However, a 5 Km fibre transmission introduced a transmission penalty therefore resulting to a slight reduction in the eye opening as illustrated by the green eye diagram in fig 8.13. The reduction in the eye-opening for 120 Gbps 8-PAM data transmission after 5 Km fibre length was due to the effect arising from inter symbol interference between the different levels of the data signal at such a high bit rate. Inter symbol interference results to a combined overlap of the different bits at different PAM levels therefore, the PAM receiver could not distinguish clearly between the received PAM bits for different PAM levels.

8.6 Summary

In this chapter, we have experimentally demonstrated the first reported technique for capacity upgrade and spectral efficiency improvement in optical fibre networks we refer to as multi-signal modulation onto a single VCSEL carrier. Combined use of 4-PAM and phase modulation to simultaneously transmit a 20 Gbps 4-PAM data and 2 GHz RF clock signal using a single mode 10 GHz bandwidth VCSEL carrier has experimentally been achieved, and a fibre transmission length of 3.21 Km attained. The high data rate (20 Gbps) and the 3.21 Km experimentally achieved in this chapter suits bandwidth '*hungry*' high speed short reach optical network applications such as telescope arrays data processing centres and supercomputers.

A 120 Gbps 8-PAM data transmission system over a 5 Km fibre length has been demonstrated through simulation. Other than the high-speed requirements, the proposed combined 4-PAM and phase modulation VCSEL technology demonstrated in this chapter comply with strict power consumption, cost and size limitations, thus allowing for integration with optical interconnects to further increase data centre network capacity. The high capacity simultaneous 4-PAM data and phase modulation RF VCSEL technology concept was demonstrated in this chapter using data rates of 20 Gbps and 2 GHz RF clock frequency due to the availability of the equipment in our laboratory. However, higher data rates and reference clock frequencies can still be supported using the same concept where splitting ratio, reach, and aggregated capacity can be traded off against one another to maximize system's performance. In addition, innovative network designs techniques aimed at reducing the overall network cost and complexity through shared infrastructure is an ideal alternative approach to address connectivity issues in densely packed telescope array networks and data centres.

The next chapter presents reach extension in VCSEL-based RF clock signal distribution in long-haul fibre networks through the adoption of Raman amplification. This is achieved experimentally by utilizing two pumping techniques namely forward pumping and backward pumping.

Chapter 9

Raman amplification for reach extension in long-haul telescope array networks

As demonstrated in chapter 4, high-speed VCSEL technology is limited by low optical power and frequency chirping resulting from dispersion effects within the fibre transmission length therefore limiting the total reach attainable. To extend the transmission reach of VCSEL-based links for adoption in long haul networks such as the SKA spiral arm, a proper signal amplification technique should be adopted. In this chapter, Raman amplification for RF clock signal distribution in extended reach astronomical telescope array networks and other extended reach terrestrial optical fibre network applications is experimentally demonstrated. This is achieved by employing two pumping techniques namely forward pumping and backward pumping. A maximum on off gain of 5.7 dB and 1.5 dB was experimentally attained for forward pumping and backward pumping at 24 dBm pump power respectively.

9.1 Raman amplification for extended Reach VCSEL-based clock signal distribution systems

Raman amplification is a promising approach for reach extension in terrestrial optical fibre networks, for long-haul transmission applications. This is due to its ability to achieve a high flat gain over wide range of wavelengths, and the ability to achieve distributed Raman gain on any transmission fibre [296-300]. Raman amplification is a potential approach in meeting unique requirements of very large baseline interferometry (VLBI) and certain kinds of astronomical observation such as pulsar work in next-generation telescope array networks. This section experimentally demonstrates the potential of Raman amplification for its adoption in long-haul reach optimization in astronomical telescope array networks and other extended reach terrestrial optical fibre network applications.

Fig 9.1 shows the experimental set up used to study Raman gain characterization. An Agilent tunable laser source model number 8164A was used to generate a signal source at wavelength λ_S =1550.4 nm. An optical attenuator was used to vary the optical power of the signal source so as to attain an optimum signal power. The optical signal was therefore attenuated to -10 dBm using an optical attenuator. A single mode GVT 074 laser diode operating at a high power range with a lasing bias threshold of about 62 mA and a maximum output power of approximately. 254.6 mW at 1454.3 mA was used as a Raman pump (λ_P) as shown in fig 9.1.

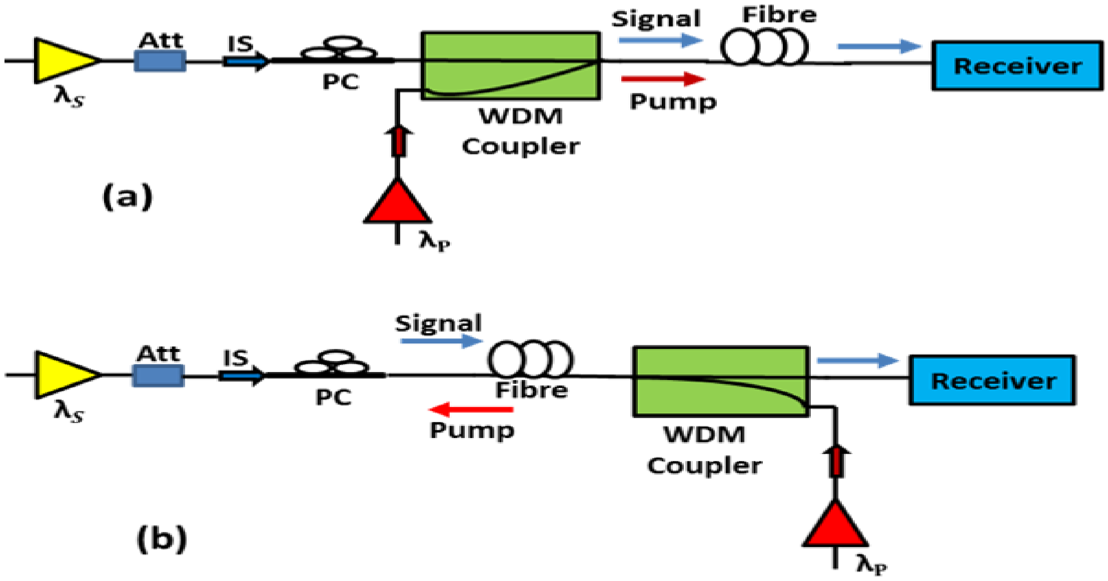

Fig 9.1: Experimental setup for gain characterisation for distributed fibre Raman amplification (FRA) at (a) Co-pumping and (b) Counter pumping schemes.

The Raman pump had a lasing wavelength of 1448 nm, and its output was varied to optimize for Raman gain. Optical isolators were used on the Raman pump as well as the signal laser source to maintain the output light beam in a forward direction thus protecting the laser sources from the counter-propagating light wave. Polarization controllers were used at the input to vary the orientation of signal and pump polarization states to ensure best coupling into the fibre. A WDM coupler was used to couple the pump and signal wavelengths to ensure Raman amplification over a transmission fibre length. At the receiver end, a WDM Raman filter was used to separate the pump wavelength from the signal wavelength for analysis.

In this study, two Raman pumping techniques namely co-pumping and counter- pumping were considered for analysis. Co-pumping here refers to a scheme where the pump and the signal wavelengths are propagated in the same direction as shown in fig 9.1 (a). Counter-pumping refers to a scheme where the pump and the signal wavelengths are propagated in opposite direction as shown in fig 9.1 (b). For distributed Raman gain optimization, 25.4 Km, 50.6 Km, 75.3 Km and 100.8 Km of true-wave reach fibre from OFS Furukawa company were utilized [301, 302]. True Wave reach optical fibre provides maximum performance for optically amplified systems over longer distances with higher capacity. This fibre meets both the ITU-T G. 655 C and E and G. 656 standards. Optimized for Raman amplification, the fibre minimizes the need for complex dispersion management and additional amplification [303].

9.1.1 Raman gain optimization

Distributed Raman gain optimization in optical fibre networks is highly dependent on wavelength separation between the pump wavelength and the signal wavelength. The frequency difference between the pump and the signal is referred to as the Stokes shift or the pump-signal detuning [304]. Fig 9.2 (b), shows experimentally measured pump-signal wavelength separation. The bias characteristics of a single mode GVT 074 laser diode (Raman pump) used in this study is shown in fig 9.2 (a). From fig 9.2 (b), a maximum gain is achieved when the pump is detuned 100 nm below the signal wavelength as depicted in fig 9.2 (b). The bias characteristics of a Raman Pump is shown in fig 9.2 (a). The Raman laser diode was noted to operate at higher bias currents as shown in fig 9.2 (a).

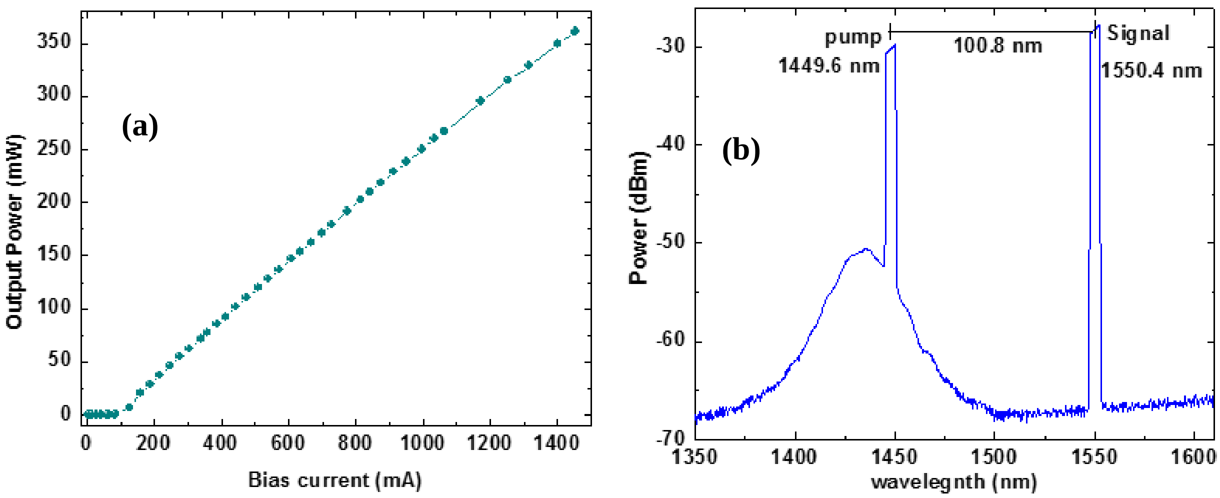

Fig 9.2: Static performance of a single mode GVT 074 Raman pump (a), pump-signal wavelength detuning (b).

Raman gain spectrum in standard single mode optical fibres is extremely broad and extends over a wide range of wavelengths as shown in fig 9.3 (a). The broad gain is an indicator of the continuum nature of the vibrational states of silica corresponding to different transition states as reported in [305, 306]. The Raman on-off gain performance of a VCSEL laser source is shown in fig 9.3 (b). On-off gain here refers to the difference between the signal power at the receiver end when the Raman pump laser diode is on and when off.

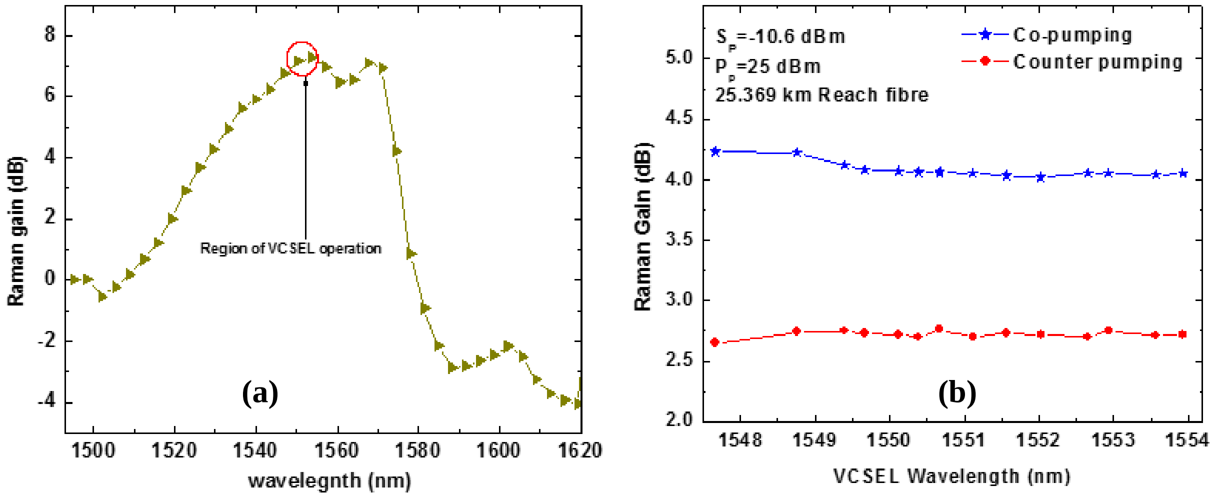

Fig 9.3: Illustration of the Raman gain spectrum in a single mode fibre at co-pumping, showing the wavelength region of VCSEL operation (a), Raman gain spectrum of a single mode Raycan VCSEL at co-pumping and counter pumping (b).

The experimentally measured VCSEL-based Raman on-off gain for co-pumping and counter pumping schemes was attained by exploiting VCSEL tuneability with change is bias current to attain different emission wavelengths as shown in fig 9.3 (b).

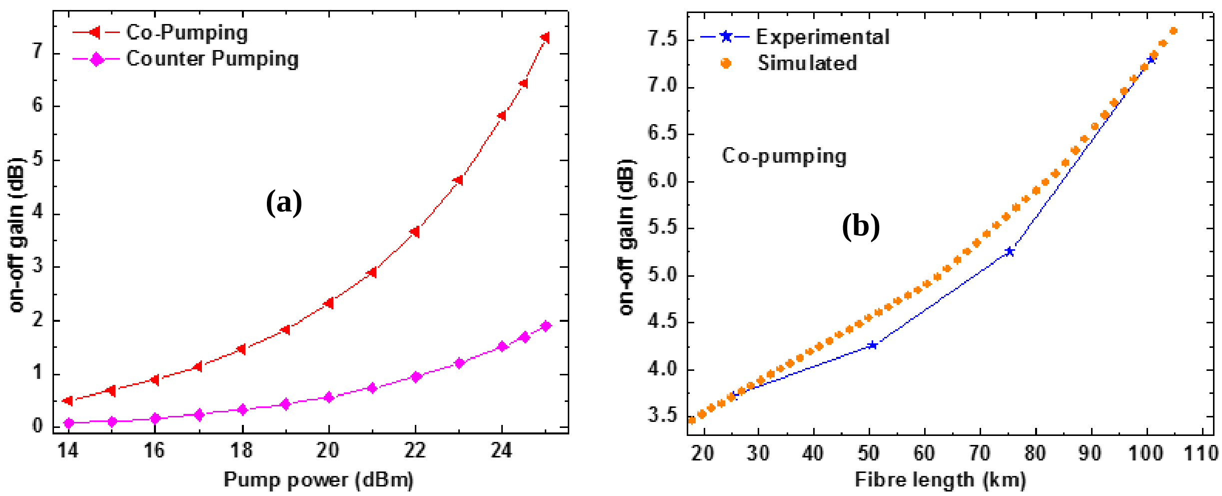

Fig 9.4: Experimentally measured Raman on-off gain with changing pump power for co-pumping and counter pumping schemes (a), experimental and simulated Raman on-off gain optimization over varying fibre lengths for a co-pumping scheme (b).

The VCSEL emission wavelength shifted from 1547.7 nm to 1554.2 nm as the bias current was changed from changed from this was changed from 3.6 mA to 9.6 mA. Fig 9.4 (a) shows experimentally measured Raman gain performance at different pump powers for co-pumping and counter pumping schemes. A signal power of -10 dBm was used throughout this study. A total fibre length of 100.8 Km was used. As depicted in fig 9.4 (a), Raman gain was noted to increase with an increase in pump power for both pumping schemes. This is because as the pump power is increased, the relative power difference between the pump and the signal also increases thus the pump transfers more energy to the signal resulting to more Raman gain [89, 298, 304].

From results in fig 9.4 (a), co-pumping was noted to have a superior Raman gain performance as opposed to counter pumping. It is true that when a pump wavelength is co-propagated with a signal wavelength, more pump energy is transferred to the weak signal thus higher amplification levels can be achieved due to proper utilization of the pump power [297, 304]. Experimental and simulated Raman on-off gain optimization over varying fibre lengths for a co-pumping scheme is shown in fig 9.4 (b). As can be seen in fig 9.4 (b), the experimental results agree with the simulations. The small mismatch between the Raman gain obtained in simulations and the one measured experimentally might be a result of losses due to fibre splices and connectors which were not considered in the simulations. From results in fig 9.4 (b), it is true that Raman on-off gain increases with increase in fibre length a maximum gain of 7.2 dB was experimentally realized for 100.8Km fibre length at 24 dBm pump power. An increase in fibre length means more pump to signal interaction time which leads to more pump to signal energy transfer therefore improving the obtained Raman gain [305, 307].

9.1.2 Experimental demonstration of Raman amplification in extended reach clock signal distribution

The experimental setup shown in fig 9.5, was used to illustrate Raman amplification in extended reach clock signal distribution for telescope array networks. This is a demonstration on the use of Raman amplification to distribute reference frequency clock signals (RF) from a central processor unit to remote antennae elements over a long-haul optical fibre span. A 1550 nm VCSEL laser was modulated with a 2 GHz RF clock signal from a signal generator as shown in fig 9.5. The modulated VCSEL was therefore used as a signal source in this study. A Raman pump operating at a wavelength λ_P = 1448 nm and with an output power of

25 dBm was optimized for Raman amplification and coupled with the signal wavelength onto a single fibre strand to allow for Raman amplification as discussed in section 9.1. For a co-pumping Raman amplification scheme, only Raman pump 1 was used. Consequently, for a counter pumping scheme only Raman pump 2 was used as shown in fig 9.5. With the exploitation of Raman amplification, the RF clock signal was transmitted over a fibre length of 100.8 Km. the phase noise and jitter performance of the received RF clock signal was analyzed directly using an electrical spectrum analyzer as shown in fig 9.5.

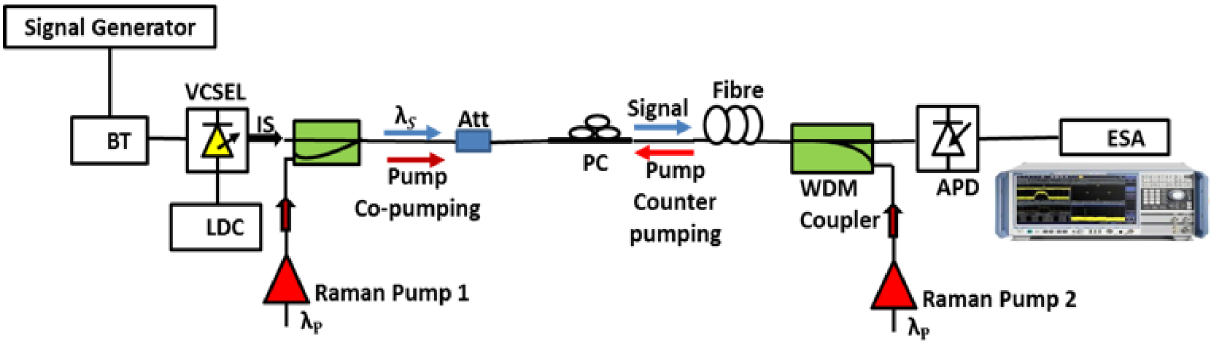

Fig 9.5: Schematic experimental research setup used to study Raman-based extended reach clock signal distribution employing co-pumping and counter-pumping schemes.

9.1.3 Stability analysis of Raman-based 2 GHz reference frequency clock signal distribution

As demonstrated in chapter 5 and other subsequent chapters, VCSEL transmitters are characterized with incredible power efficiency and high-speed transmissions because of their high bandwidth. However, this comes at a cost of low optical power output and frequency chirping thus significantly increasing dispersion effects therefore degrading the QoS. Dispersion effects worsen with longer transmission fibre lengths. To adopt VCSEL transmission in long-haul systems, amplification or use of sensitive receivers such as APD is a viable option. Raman amplification can be adopted in next-generation telescope array networks employing VCSELs if longer transmission reach is to be achieved.

Fig 9.6 (a), shows experimentally measured power spectrum of a 2 GHz RF clock signal over 100.8 Km employing Raman amplification at both co-pumping and counter pumping schemes fig 9.6 (a). From results in fig 9.6 (a), the output RF power level remained high for both co-pumping (blue) and counter pumping (green) schemes respectively. However, when no amplification mechanism was used (red), the signal level remained at low levels due to signal attenuation along the optical fibre medium as depicted in fig 9.6 (a). Fig 9.6 (b) shows RF clock signal sine wave at different modulation clock frequencies. For demonstration purposes, a 25.4 Km of G. 655 SMF-Reach optical fibre was used. It was noted that, dispersion effects caused the signal quality to distort as the clock signal modulation frequency increased from 2 GHz to 10 GHz. In this case, no signal amplification was utilized.

The experimental phase noise measurement for a 2 GHz VCSEL transmission over 100.8 Km fibre exploiting co-pumping and counter pumping amplification schemes is shown in fig 9.7.

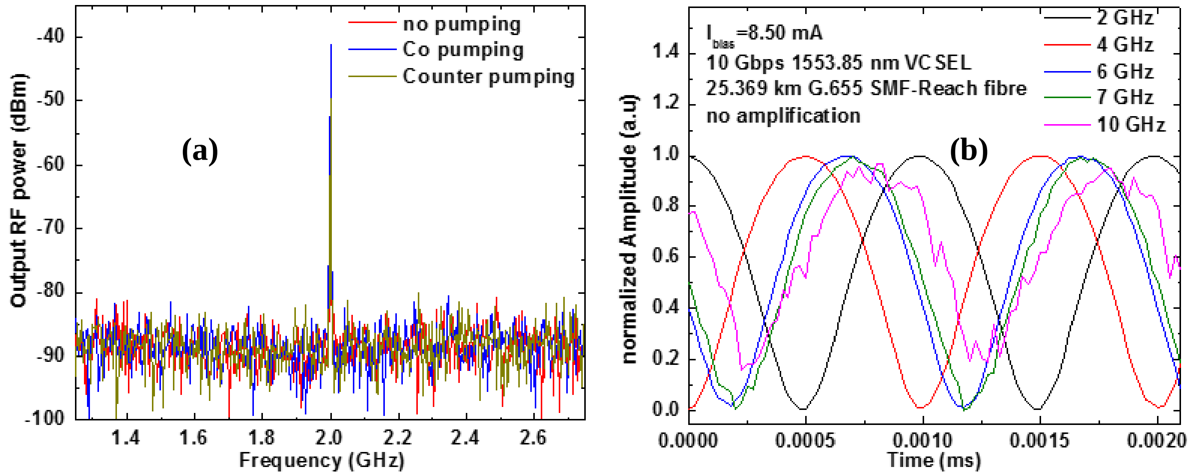

Fig 9.6: Experimentally measured power spectrums for a 2 GHz RF clock signal at co-pumping and counter pumping schemes (a), Measured RF clock signal sine wave at different modulation frequencies (b).

The used 100.8 Km fibre length had a maxim cumulative dispersion of 89 ps which degraded the received phase noise to -86.59 dBc/Hz at 100 KHz offset frequency, without Raman amplification as shown in fig 9.7. However, with the adoption of Raman amplification, the phase noise of the received signal improved to -117.66 dBc/Hz and -105.16 dBc/Hz for counter pumping and co-pumping schemes respectively at the same frequency offset. This improvement was due to signal power gains because of Raman amplification that enabled the long reach VCSEL-based transmission. The high signal power attained due to amplification reduced the dispersion effects resulting to a lower phase noise performance. It is true that co-pumping had superior phase noise performance than counter pumping as depicted by RF clock jitter measurement results in fig 9.7.

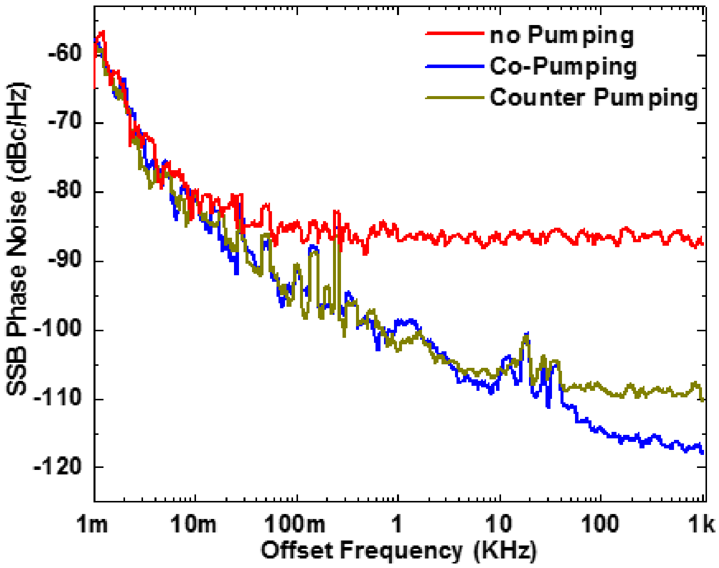

Fig 9.7: Experimentally measured Phase noise for a 2 GHz RF clock signal transmission over 100.8 Km fibre at co-pumping and counter pumping schemes.

Fig 9.8 shows experimentally measured RF clock jitter performance for co-pumping and counter pumping schemes at different fibre lengths. The measured RF clock jitter was analysed over a frequency range of 1 Hz to 1 MHz. Short term stability (Jitter) in optical reference signal is vital for proper control performance of signal to noise degradation by electronic digitizers during data digitization process for telescope array networks. It was noted that the maximum measured clock jitter increased with increase in fibre length as shown in fig 9.8.

A maximum RF clock jitter (RMS) of 5.36 ps was incurred without Raman amplification over a 100.8 Km fibre transmission length. However, with the adoption of Raman amplification, this value reduced to 3.55 ps and 1.7 ps for counter and co-pumping schemes respectively. The time domain sin wave of a 2 GHz RF clock signal is shown in fig 9.8. From the results in fig 9.8, noise contribution over the fibre transmission length caused the instantaneous frequency to "jitter" around the nominal frequency, with probability of being higher or lower than the nominal frequency. This resulted in the distortion of the RF signal sine wave especially when no pumping was applied, therefore accounting for its worst jitter performance. Co-pumping was noted to show a superior performance as opposed to counter pumping at the same pump power and fibre length. Co-pumping scheme is therefore a recommended Raman amplification approach to next-generation telescope array networks due to its incredible signal recovery performance.

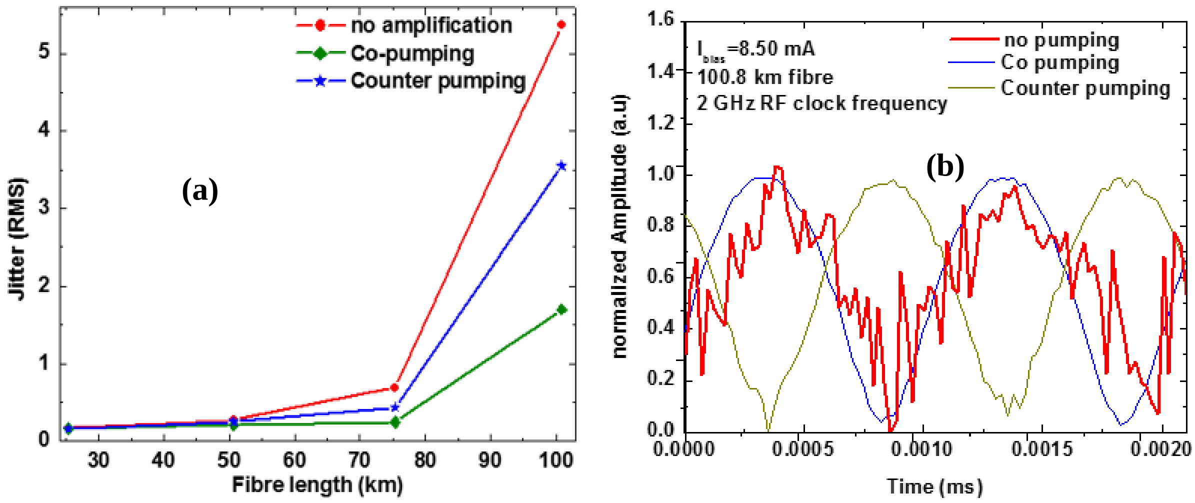

Fig 9.8: Experimentally RF clock jitter performance with fibre length for co-pumping and counter pumping schemes (a), measured 2 GHz RF clock signal sine wave at signal at co-pumping and counter pumping schemes (b).

Long-haul telescope array networks such as SKA spiral-arms which are characterized with longer baselines (over 76 Km for SKA) need an intelligent dispersion management mechanism to achieve its observational objectives. This can be implemented by exploiting high speed VCSELs in RF clock signal transmission, and Raman amplification in dispersion management to maximize the transmission reach. By adopting the discussed experimental demonstrations, it is true that the integration of Raman amplification and VCSEL-based RF clock signal transmission is an exciting alternative for maximizing reach in next-generation telescope array networks.

9.2 Summary

This chapter has provided experimental findings for reach optimization in long-haul optical fibre networks. In extending reach to meet the unique requirements of terrestrial fibre networks such as telescope array networks with longer base-lines like SKA spiral arms, Raman amplification has been adopted and experimentally demonstrated. By considering a 1550 nm VCSEL in transmission of a 2 GHz RF clock signal, dispersion management in RF clock signal distribution has been demonstrated and over 100.8 Km of Raman assisted clock distribution attained. Two pumping techniques namely forward pumping and backward pumping have been experimentally demonstrated. A maximum on off gain of 5.7 dB and 1.5 dB has been achieved experimentally for forward pumping and backward pumping at 24 dBm pump power respectively. A maximum jitter improvement of 3.66 ps and 3.38 ps has been achieved using co-pumping and counter pumping schemes respectively over a 100.8 Km fibre transmission. The work presented in this chapter therefore proves a key concept for adoption in next-generation extended reach telescope array networks.

Chapter 10

Conclusions

Optical fibre transport forms the backbone of modern astronomical telescope arrays as well as time and frequency reference systems. Reference frequency clock signals are of great importance in timekeeping systems such as Coordinated Universal Time (UTC), global positioning system (GPS) and in banking. Optical fibres also plays a key role in telecommunication networks such as data centre networks and terrestrial optical networks in transmission of high-speed data traffics. The first part of this thesis exploited wavelength tunable VCSEL transmitters to simultaneously distribution both data and timing signals over shared network infrastructure as a desirable cost effective approach in meeting unique requirements of large and most challenging optical fibre network systems in science like astronomical telescope array networks. Dual modulation of a single mode 10 GHz bandwidth VCSEL carrier in simultaneous transmission of directly modulated 10 Gbps data signal and polarization-based pulse-per-second (PPS) clock signal was proposed as an alternative technique to maximize carrier spectral efficiency and network flexibility. This thesis further
Proposed on a number of capacity and carrier spectral efficiency upgrade schemes such as VCSEL-based 4-PAM for simultaneous data and RF clock signal transmission, simultaneous data and RF clock transmission in WDM solutions, simultaneous multiple-signal modulation on a single VCSEL carrier for multicast transmission systems as well as Raman amplification for reach optimization in optical communication networks.

Capacity and spectral efficiency improvement of existing optical networks means that these networks can be used to transmit higher bitrates without the need of rewiring, and that new, longer links can be implemented without compromising the transmission speeds. Findings of this thesis therefore have key implications for adoption in high capacity short range data centre links at a benefit of reduced installation cost, power efficiency and low complexity, however at the cost of limited transmission reach. Proposed transmission techniques from this thesis will enable the transition to the next-generation, high-speed optical applications such as big data science projects, new consumer links like thunderbolts and cloud computing.

Appendix A

Research outputs in journals, peer reviewed conferences and books of abstracts

Published articles

2017:

1) **G. M. Isoe**, S. Wassin, R. Gamatham, A. Leitch, and T. Gibbon, "Capacity upgrade in short-reach optical fibre networks: simultaneous 4-PAM 20 Gbps data and polarization-modulated PPS clock signal using a single VCSEL carrier," Journal of Modern Optics, vol. 64, (20), pp. 2245-2254, 2017.
2) **G. M. Isoe**, S. Wassin, R. R. G. Gamatham, A. W. R. Leitch, and T. B. Gibbon, "A high capacity data Centre network: Simultaneous 4-PAM data at 20 Gbps and 2 GHz phase modulated RF clock signal over a single VCSEL carrier," Journal of Modern Optics, vol. 64, (21), pp. 2336-2344, 2017.
3) E. K. Rotich Kipnoo, D. Kiboi Boiyo, **G. M. Isoe**, T. V. Chabata, R. R. G. Gamatham, A. W. R. Leitch, et al., "Demonstration of Raman-based, dispersion-managed VCSEL technology for fibre-to-the-hut application," Optical Fiber Technology, vol. 34, pp. 1-5, 3// 2017.
4) S wassin, **G. M. Isoe**, R. R. G. Gamatham, A. W. R. Leitch, and T. B. Gibbon, "Application of VCSELs in Next-Generation Telescope Array Networks such as the Square Kilometre Array," Journal of Optics and Laser Technology, 2018: *In Press*.
5) **G. M. Isoe**, S. Wassin, R. R. G. Gamatham, A. W. R. Leitch, and T. B. Gibbon, "Simultaneous 10 Gbps data and polarization-based pulse-per-second clock transmission using a single VCSEL for high-speed optical fibre access networks," Proc. SPIE 10129, Optical Metro Networks and Short-Haul Systems IX, 101290F (January 28, 2017); doi:10.1117/12.2252230, pp. 101290F-101290F-12.
6) S. Wassin, **G. M. Isoe**, R. R. G. Gamatham, A. W. R. Leitch, and T. B. Gibbon, "Highly accurate pulse-per-second timing distribution over optical fibre network using VCSEL side-mode injection," Proc. SPIE. 10129, Optical Metro Networks and Short-

Haul Systems IX, 101290G. (January 28, 2017) doi: 10.1117/12.2252069, pp. 101290G-101290G-12.

7) **G. M. Isoe**, S. Wassin, R. R. G. Gamatham, A. W. R. Leitch, and T. B. Gibbon, "High Capacity Data Centre Network: Simultaneous 4-PAM Data at 20 Gbps and 2 GHz Phase Modulated RF Clock Signal over a Single VCSEL Carrier," The annual 2017 Southern African Telecommunication Networks and Application Conference (SATNAC) 3rd – 10th September 2017 on the Freedom of the Seas Cruise Liner, Royal Caribbean International, Barcelona, Spain, pp. 148-153.
8) S. Wassin, **G. M. Isoe**, R. R. G. Gamatham, A. W. R. Leitch, and T. B. Gibbon, "Fibre-Based Time and Frequency Distribution using a DFB Phase Error Correction Actuator," The annual 2017 Southern African Telecommunication Networks and Application Conference (SATNAC) 3rd – 10th September 2017 on the Freedom of the Seas Cruise Liner, Royal Caribbean International, Barcelona, Spain, pp. 154-157.
9) **G. M. Isoe**, S. Wassin, R. R. G. Gamatham, A. W. R. Leitch, and T. B. Gibbon, "Transmission performance of 10 Gbps OOK, 15 Gbps 2-PAM and 20 Gbps 4-PAM data signals over 11 Km using a 1310 nm VCSEL," the 62nd annual conference of the South Africa Institute of Physics (SAIP), Stellenbosch University, 3rd – 7th July 2017.
10) S. Wassin, **G. M. Isoe**, R. R. G. Gamatham, A. W. R. Leitch, and T. B. Gibbon, " Towards the Development of VCSEL-Based Time and Frequency Dissemination System using a DFB Phase Error Correction Actuator for the SKA," the 62nd annual conference of the South Africa Institute of Physics (SAIP), Stellenbosch University, 3rd – 7th July 2017.

2016:

1) **G. M. Isoe**, S. Wassin, D. Kiboi Boiyo, E. K. Rotich Kipnoo, R.R.G. Gamatham, A.W.R. Leitch and T. B. Gibbon, "Effect of 10 Gbps Data Transmission on 1.712 GHz 1309.97 nm VCSEL Based Radio Frequency Distribution over a Single Optical Fibre for the Telescope Array," The annual 2016 Southern African Telecommunication Networks and Application Conference (SATNAC) 4th to 7th September 2016 at Fancourt in George, Western Cape, South Africa, pp. 150-153, ISBN: 978-0-620-72418-0.

2) D. Kiboi Boiyo, **G. M. Isoe**, E. K. Rotich Kipnoo, R. R. G. Gamatham, A.W. R. Leitch and T. B. Gibbon, "Utilization of Flexible Spectrum to Optimize a 24.7 Km Fibre TDM Passive Optical Network", Proceedings of the SATNAC Conference 2016, Fancourt, George, South Africa (4th – 7th Sept 2016), pp. 8-12. ISBN: 978-0-620-72418-0.
3) S. Wassin, **G. M. Isoe**, R. R. G. Gamatham, A. W. R. Leitch, T. B. Gibbon, "Component Power Budget Analysis and VCSEL Characterization for the Square Kilometre Array Signal and Data Transport Network," The annual 2016 Southern African Telecommunication Networks and Application Conference (SATNAC) 4th to 7th September 2016 at Fancourt in George, Western Cape, South Africa pp. 154-159, ISBN: 978-0-620-72418-0.
4) K. J. Leburu, **G. M. Isoe**, S. Wassin, D. Kiboi Boiyo, R.R.G. Gamatham, A.W.R. Leitch and T. B. Gibbon, "Transmission of Pulse per Second Clock Tone Signals in Optical Communication Systems over Optical Fibre and Free Space," The annual 2016 Southern African Telecommunication Networks and Application Conference (SATNAC) 4th to 7th September 2016 at Fancourt in George, Western Cape, South Africa.
5) **G. M. Isoe**, D. K. Boiyo, S. Wassin, R. R. G. Gamatham, A.W. R. Leitch and T. B. Gibbon, "Effect of 1.712 GHz RF-Clock Signal Distribution on 10 Gbps 1550.89 nm VCSEL Based Transmission over Single Optical Fibre for Square Kilometre Telescope Array," 61 South African Institute of Physics (SAIP) 2016 Conference, university of Cape Town, South Africa, 04-08 July 2016.
6) Kiboi Boiyo, **G. M. Isoe**, R. R. G. Gamatham, A. W. R. Leitch, T. B. Gibbon, "A 1550-nm all-optical VCSEL-to-VCSEL wavelength conversion of a 8.5-Gb/s data signal and transmission over a 24.7-Km fibre." Proc. SPIE 10036, Fourth Conference on Sensors, MEMS, and Electro-Optic Systems, 100360X (February 3, 2017); doi:10.1117/12.2244524.
7) D. K. Boiyo, **G. M. Isoe**, S. Wassin, E. K. Rotich Kipnoo, R. R. G. Gamatham, A.W. R. Leitch and T. B. Gibbon, "Characterization and Compensation of Fibre Link Dispersion in a 10 Gb/s Flexible Network," 61 South African Institute of Physics (SAIP) 2016 Conference, university of Cape Town, South Africa, 04-July 8, 2016.

8) S. Wassin, **G. M. Isoe**, D. K. Boiyo, R. R. G. Gamatham, A.W. R. Leitch and T. B. Gibbon, “Power Budget Analysis of Passive Components along an Optical Fibre Link of a Frequency Dissemination System within the MeerKAT Telescope Array,” 61 South African Institute of Physics (SAIP) 2016 Conference, university of Cape Town, South Africa, 04-July 8, 2016.
9) K. J. Leburu, **G. M. Isoe**, D. K. Boiyo, S. Wassin, R. R. G. Gamatham, A.W. R. Leitch and T. B. Gibbon, “Advantages of Free Space Optics over Optical Fibre for Clock Tone Distribution in a 2.5 GHz Transmission Link,” 61 South African Institute of Physics (SAIP) 2016 Conference, university of Cape Town, South Africa, 04-July 8, 2016.
10) D. Kiboi Boiyo, **G. M. Isoe**, S. Wassin, E. K. Rotich Kipnoo, R. R. Gamatham, A. W. R. Leitch and T. B. Gibbon, “An all Optical VCSEL Wavelength Conversion for Optical Fibre Access Networks,” Proceedings of 2016 international conference on Sustainable Research and innovation (SRI), Vol. 7, ISSN: 2079-6226, pp. 17-20, May 2016.
11) S. Wassin, **G. M. Isoe**, D. Kiboi Boiyo, R. R. Gamatham, A. W. R. Leitch and T. B. Gibbon, “The Square Kilometre Array: The Notion of Timing and Synchronization,” Proceedings of 2016 international conference on Sustainable Research and innovation (SRI), Vol. 7, ISSN: 2079-6226, pp. 52-55, May 2016.
12) Cherutoi, Henry, Muguro K., Waswa D., **Isoe G. M.**, “Performance of DQPSK, NRZ and RZ modulation formats in different optical fibres,” Proceedings of 2016 international conference on Sustainable Research and innovation (SRI), Vol. 7, ISSN: 2079-6226, pp. 186-189, May 2016.

2015:

1) **G. M. Isoe**, E. K. Rotich, R. R. G. Gamatham, A.W. R. Leitch and T. B. Gibbon, “Stimulated Brillouin Scattering Threshold Measurement for Optical Fibre Temperature Sensor Design for the Square Kilometre Array (SKA) Telescope,” Proceedings of 2015 Southern African Telecommunication Networks and Application Conference (SATNAC), Arabella Hotel & Spa, Kogelberg Biosphere Reserve near

Hermanus, Western Cape, South Africa, ISBN: 978-0-620-67151-4, pp. 11-12, 6th – 9th September 2015.

2) **G M Isoe**, R R G Gamatham, A W R Leitch and T B Gibbon, "Simultaneous Clock Tone and Data Transmission over Same Optical Fibre for Square Kilometre Array Cost Effective Telescope Network," SKA SA-HCD 2015 Postgraduate Bursary Conference, Stellenbosch, Cape Town, 30th Nov- 8th Dec 2015.
3) **G. M. Isoe**, E. K. Rotich, D. K. Boiyo, R. R. G. Gamatham, A. W. R. Leitch, T. B. Gibbon D.W.Waswa and K. M. Muguro, "Noise Fig and Pump Reflection Power in SMF-Reach Optical Fibre for Raman Amplification," AFRICON, 2015 Addis Ababa, 2015, pp.1-5. doi:10.1109/AFRCON.2015.7332036, pp 1 – 5, 2015.
4) **G. M. Isoe**, E. K. Rotich, R. R. G. Gamatham, A.W. R. Leitch and T. B. Gibbon, "Fibre-to-the-Hut Technology: A Solution for Cheap Access for High Speed-Optical Network in South Africa," 60th South African Institute of Physics (SAIP) 2014 Conference, board work conference centre, Eastern Cape, South Africa, ISBN: 978-0-620-70714-5, pp.440-444, 29th June -3rd July 2015.
5) D. M. Osiemo, **G. M. Isoe**, D. W. Waswa and K. M. Muguro "Investigation of Slow Light in Single Mode Fibres (SMF) for the Basis of Stimulated Brillouin Scattering and the Application in Sensing," Proceedings of 2015 international conference on Sustainable Research and innovation (SRI), Vol. 6, ISSN: 2079-6226, pp. 74-79, May 2015.
6) D. M. Osiemo, D.W. Waswa, K.M. Muguro, **G. M. Isoe**, & H. Cherutoi, "Stimulated Brillouin Scattering (SBS) Characterization of Optical Fibres and a Technique of Slow Light Generation," University of Eldoret 1st interdisplinary conference,18th – 19th June 2015.

References

[1] P. J. Hall, *The square kilometre array: An engineering perspective* vol. 2: Springer, 2005.

[2] P. E. Dewdney, P. J. Hall, R. T. Schilizzi, and T. J. L. W. Lazio, "The Square Kilometre Array," *Proceedings of the IEEE*, vol. 97, pp. 1482-1496, 2009.

[3] K. Grainge, B. Alachkar, S. Amy, D. Barbosa, M. Bommineni, P. Boven*, et al.*, "Square Kilometre Array: The radio telescope of the XXI century," *Astronomy Reports*, vol. 61, pp. 288-296, 2017.

[4] D. Lucero, C. Carignan, E. Elson, T. Randriamampandry, T. Jarrett, T. Oosterloo*, et al.*, "H i observations of the nearest starburst galaxy NGC 253 with the SKA precursor KAT-7," *Monthly Notices of the Royal Astronomical Society*, vol. 450, pp. 3935-3951, 2015.

[5] T. B. Gibbon, E. K. R. Kipnoo, R. R. Gamatham, A. W. Leitch, R. Siebrits, R. Julie*, et al.*, "Fiber-to-the-telescope: MeerKAT, the South African precursor to Square Kilometre Telescope Array," *Journal of Astronomical Telescopes, Instruments, and Systems*, vol. 1, pp. 028001-028001, 2015.

[6] D. B. Davidson, "MeerKAT and SKA phase 1," in *Antennas, Propagation & EM Theory (ISAPE), 2012 10th International Symposium on*, 2012, pp. 1279-1282.

[7] D. R. DeBoer, R. G. Gough, J. D. Bunton, T. J. Cornwell, R. J. Beresford, S. Johnston*, et al.*, "Australian SKA pathfinder: A high-dynamic range wide-field of view survey telescope," *Proceedings of the IEEE*, vol. 97, pp. 1507-1521, 2009.

[8] P. J. Hall, "The Square Kilometre Array," 2007.

[9] P. A. Woudt, R. P. Fender, R. P. Armstrong, and C. Carignan, "Early science with the Karoo Array Telescope test array KAT-7," *South African Journal of Science*, vol. 109, pp. 01-02, 2013.

[10] D. B. Davidson, "Potential technological spin-offs from MeerKAT and the South African Square Kilometre Array bid," *South African Journal of Science*, vol. 108, pp. 01-03, 2012.

[11] R. Booth and J. Jonas, "An overview of the MeerKAT project," *African Skies*, vol. 16, p. 101, 2012.

[12] R. Armstrong, R. Fender, G. Nicolson, S. Ratcliffe, M. Linares, J. Horrell*, et al.*, "A return to strong radio flaring by Circinus X-1 observed with the Karoo Array Telescope test array KAT-7," *Monthly Notices of the Royal Astronomical Society*, vol. 433, pp. 1951-1957, 2013.

[13] C. Carignan, B. Frank, K. Hess, D. Lucero, T. Randriamampandry, S. Goedhart*, et al.*, "Kat-7 science verification: Using hi observations of ngc 3109 to understand its kinematics and mass distribution," *The Astronomical Journal*, vol. 146, p. 48, 2013.

[14] G. Heald, W. de Blok, D. Lucero, C. Carignan, T. Jarrett, E. Elson*, et al.*, "Neutral hydrogen and magnetic fields in M83 observed with the SKA Pathfinder KAT-7," *Monthly Notices of the Royal Astronomical Society*, vol. 462, pp. 1238-1255, 2016.

[15] C. Carignan, "Cosmic Web Research with KAT-7, MeerKAT & FAST," *arXiv preprint arXiv:1510.03462*, 2015.

[16] C. Carignan, Y. Libert, D. Lucero, T. Randriamampandry, T. Jarrett, T. Oosterloo*, et al.*, "H I observations of two new dwarf galaxies: Pisces A and B with the SKA Pathfinder KAT-7," *Astronomy & Astrophysics*, vol. 587, p. L3, 2016.

[17] K. M. Hess, T. Jarrett, C. Carignan, S. S. Passmoor, and S. Goedhart, "KAT-7 science verification: cold gas, star formation, and substructure in the nearby Antlia Cluster," *Monthly Notices of the Royal Astronomical Society*, vol. 452, pp. 1617-1636, 2015.

[18] S. Wild, "Ghana telescope ready for action," ed: NATURE PUBLISHING GROUP MACMILLAN BUILDING, 4 CRINAN ST, LONDON N1 9XW, ENGLAND, 2017.

[19] B. D. Asabere, M. Gaylard, C. Horellou, H. Winkler, and T. Jarrett, "Radio astronomy in Africa: the case of Ghana," *arXiv preprint arXiv:1503.08850*, 2015.

[20] M. Gaylard, M. Bietenholz, L. Combrinck, R. Booth, S. Buchner, B. Fanaroff, *et al.*, "An African VLBI network of radio telescopes," *arXiv preprint arXiv:1405.7214*, 2014.

[21] M. Gaylard, "Expanding radio astronomy in Africa," in *IOP Conference Series: Materials Science and Engineering*, 2013, p. 012020.

[22] D. Barbosa, J. P. Barraca, A.-J. Boonstra, R. Aguiar, A. van Ardenne, J. de Santander-Vela, *et al.*, "A Sustainable approach to large ICT Science based infrastructures; the case for Radio Astronomy," in *Energy Conference (ENERGYCON), 2014 IEEE International*, 2014, pp. 668-674.

[23] M. Gastrow, "Understanding interactive capabilities for skills development in sectoral systems of innovation: A case study of astronomy and the Square Kilometre Array telescope," 2015.

[24] G. SPACE, "Ghana Space Science and Technology Institute (GSSTI)."

[25] A. A. Abiodun, "Trends in the global space arena–Impact on Africa and Africa's response," *Space Policy*, vol. 28, pp. 283-290, 2012.

[26] R. Schilizzi and A. Wilkinson. (13th August 2017). *SKA-SADT technical development plan, No. SKA-TEL.SADT-PROP_Tech-RED-001*. Available: http://skatelescope.org/wp-content/uploads/2013/09/SKA-TEL-SADT-PROP_TECH-001_Redacted_final_24Sept13.pdf

[27] R. Schilizzi, P. Alexander, J. Cordes, P. Dewdney, R. Ekers, A. Faulkner, *et al.*, "Preliminary specifications for the square kilometre array," *SKA Memorandum*, vol. 100, 2007.

[28] W. Turner, "SKA phase 1 system (level 1) requirements specification," 2014.

[29] A. R. C. James A. Barnes, Leonard S. Cutler, Daniel J. Healey, David B. Leeson, Thomas E. Mcgunigal, James A. Mullen, Jr., Warren L. Smith, Richard L. Sydnor, Robert F. C. Vessot, Gernot M. R. Winkler "Characterization of Frequency Stability," *IEEE transformations on instrumentation and measurement*, vol. IM-20, pp. 105-120, May 1971.

[30] R. McCool, M. Bentley, M. Argo, R. Spencer, and S. Garrington, "Transfer of a 1486.3 MHz frequency standard over installed fibre links for local oscillator distribution with a stability of 1 picosecond."

[31] J. Lauf, M. Calhoun, P. Kuhnle, R. Sydnor, and R. Tjoelker, "Master clock and time distribution system for the NASA deep space network," MASSACHUSETTS UNIV AMHERST COLL OF ENGINEERING2004.

[32] S. Schiller, A. Görlitz, A. Nevsky, J. Koelemeij, A. Wicht, P. Gill, *et al.*, "Optical clocks in space," *Nuclear Physics B-Proceedings Supplements*, vol. 166, pp. 300-302, 2007.

[33] S. A. Diddams, J. C. Bergquist, S. R. Jefferts, and C. W. Oates, "Standards of time and frequency at the outset of the 21st century," *Science*, vol. 306, pp. 1318-1324, 2004.

[34] A. D. Ludlow, M. M. Boyd, J. Ye, E. Peik, and P. O. Schmidt, "Optical atomic clocks," *Reviews of Modern Physics*, vol. 87, p. 637, 2015.

[35] J. D. Kraus, "Radio astronomy," *New York: McGraw-Hill, 1966*, 1966.

[36] W. N. Christiansen and J. A. Högbom, *Radiotelescopes*: CUP Archive, 1987.

[37] V. Rubin, "OBSERVATIONS OF RADIO GALAXIES," *Hautes Énergies en Astrophysique: High Energy Astrophysics. Lectures Delivered at Les Houches During the 1966 Session of the Summer School of Theoretical Physics, with a Grant from NATO.*, vol. 1, p. 135, 1967.

[38] M. Tiuri, "Radio astronomy receivers," *IEEE Transactions on Antennas and Propagation*, vol. 12, pp. 930-938, 1964.

[39] K. Rohlfs and T. Wilson, *Tools of radio astronomy*: Springer Science & Business Media, 2013.

[40] P. Moore, "1985 yearbook of astronomy," *1985 yearbook of astronomy.. P. Moore (Editor). WW Norton and Co., 500 Fifth Avenue, New York, NY 10036, USA. 208 pp. Price US $9.95 (1984). ISBN 0-393-30203-2.*, 1984.
[41] C. M. Cade, "Radio-astronomy and navigation," *The Aeronautical Journal,* vol. 62, pp. 805-828, 1958.
[42] P. J. Napier, A. R. Thompson, and R. D. Ekers, "The very large array: Design and performance of a modern synthesis radio telescope," *Proceedings of the IEEE,* vol. 71, pp. 1295-1320, 1983.
[43] J. Wild, "Observational radio astronomy," *Advances in Electronics and Electron Physics,* vol. 7, pp. 299-362, 1955.
[44] F. Haddock, "Introduction to radio astronomy," *Proceedings of the IRE,* vol. 46, pp. 3-12, 1958.
[45] R. N. Manchester, G. B. Hobbs, A. Teoh, and M. Hobbs, "The Australia telescope national facility pulsar catalogue," *The Astronomical Journal,* vol. 129, p. 1993, 2005.
[46] S. Johnston, M. Bailes, N. Bartel, C. Baugh, M. Bietenholz, C. Blake*, et al.*, "Science with the Australian square kilometre array pathfinder," *Publications of the Astronomical Society of Australia,* vol. 24, pp. 174-188, 2007.
[47] D. DeBoer, R. Gough, J. Bunton, T. Cornwell, R. Beresford, S. Johnston*, et al.*, "Australian SKA Pathfinder: A High-Dynamic Range Wide-Field of View Survey Telescope," *Proceedings of the IEEE,* vol. 8, pp. 1507-1521, 2009.
[48] A. Hotan, J. Bunton, L. Harvey-Smith, B. Humphreys, B. Jeffs, T. Shimwell*, et al.*, "The australian square kilometre array pathfinder: System architecture and specifications of the boolardy engineering test array," *Publications of the Astronomical Society of Australia,* vol. 31, 2014.
[49] D. DeBoer, "Australian SKA Pathfinder."
[50] A. van Ardenne, J. D. Bregman, W. A. van Cappellen, G. W. Kant, and J. G. B. de Vaate, "Extending the field of view with phased array techniques: Results of European SKA research," *Proceedings of the IEEE,* vol. 97, pp. 1531-1542, 2009.
[51] S. Johnston, I. J. Feain, and N. Gupta, "Science with the Australian square kilometre array pathfinder (ASKAP)," *arXiv preprint arXiv:0903.4011,* 2009.
[52] A. Tzioumis, S. Tingay, B. Stansby, J. Reynolds, C. Phillips, S. Amy*, et al.*, "Evolution of the Parsec-Scale Structure of PKS 1934–638 Revisited: First Science with the ASKAP and New Zealand Telescopes," *The Astronomical Journal,* vol. 140, p. 1506, 2010.
[53] S. Johnston, R. Taylor, M. Bailes, N. Bartel, C. Baugh, M. Bietenholz*, et al.*, "Science with ASKAP," *Experimental Astronomy,* vol. 22, pp. 151-273, 2008.
[54] L. Harvey-Smith, "The Australian SKA Pathfinder: First Science Results," *IAU General Assembly,* vol. 22, 2015.
[55] R. Beck, J. Anderson, G. Heald, A. Horneffer, M. Iacobelli, J. Koehler*, et al.*, "The LOFAR view of cosmic magnetism," *Astronomische Nachrichten,* vol. 334, pp. 548-557, 2013.
[56] R. L. Brown, W. Wild, and C. Cunningham, "ALMA–the Atacama large millimeter array," *Advances in Space Research,* vol. 34, pp. 555-559, 2004.
[57] A. Wootten and A. R. Thompson, "The Atacama large millimeter/submillimeter array," *Proceedings of the IEEE,* vol. 97, pp. 1463-1471, 2009.
[58] H. Ezawa, R. Kawabe, K. Kohno, and S. Yamamoto, "The Atacama Submillimeter Telescope Experiment(ASTE)," in *Proceedings of SPIE*, 2004, pp. 763-772.
[59] B. Shillue, "High-frequency local oscillator transmission for the atacama large millimeter array (ALMA)," in *Digest of the LEOS Summer Topical Meetings (IEEE): p. 119-120, 2005*, 2005, pp. 119-120.
[60] A. Wootten, "Atacama large millimeter array (ALMA)," in *Astronomical Telescopes and Instrumentation*, 2003, pp. 110-118.

[61] H. Russell, M. McDonald, B. McNamara, A. Fabian, P. Nulsen, M. Bayliss, *et al.*, "ALMA observations of massive molecular gas filaments encasing radio bubbles in the Phoenix cluster," *The Astrophysical Journal*, vol. 836, p. 130, 2017.

[62] S. K. Pavan, J. Lavrencik, R. Shubochkin, Y. Sun, J. Kim, D. S. Vaidya, *et al.*, "50Gbit/s PAM-4 MMF transmission using 1060nm VCSELs with reach beyond 200m," in *Optical Fiber Communication Conference*, 2014, p. W1F. 5.

[63] A. Isella, G. Guidi, L. Testi, S. Liu, H. Li, S. Li, *et al.*, "Ringed structures of the HD 163296 protoplanetary Disk Revealed by ALMA," *Physical review letters*, vol. 117, p. 251101, 2016.

[64] T. Shimonishi, T. Onaka, A. Kawamura, and Y. Aikawa, "The Detection of a Hot Molecular Core in the Large Magellanic Cloud with ALMA," *The Astrophysical Journal*, vol. 827, p. 72, 2016.

[65] A. K. Inoue, Y. Tamura, H. Matsuo, K. Mawatari, I. Shimizu, T. Shibuya, *et al.*, "Detection of an oxygen emission line from a high-redshift galaxy in the reionization epoch," *Science*, vol. 352, pp. 1559-1562, 2016.

[66] D. Gerdes, M. Sako, S. Hamilton, K. Zhang, T. Khain, J. Becker, *et al.*, "Discovery and physical characterization of a large scattered disk object at 92 au," *The Astrophysical Journal Letters*, vol. 839, p. L15, 2017.

[67] S. M. Andrews, D. J. Wilner, Z. Zhu, T. Birnstiel, J. M. Carpenter, L. M. Pérez, *et al.*, "Ringed Substructure and a Gap at 1 au in the Nearest Protoplanetary Disk," *The Astrophysical Journal Letters*, vol. 820, p. L40, 2016.

[68] F. Abellán, R. Indebetouw, J. Marcaide, M. Gabler, C. Fransson, J. Spyromilio, *et al.*, "Very Deep Inside the SN 1987A Core Ejecta: Molecular Structures Seen in 3D," *arXiv preprint arXiv:1706.04675*, 2017.

[69] Y.-W. Tang, S. Guilloteau, A. Dutrey, T. Muto, B.-T. Shen, P.-G. Gu, *et al.*, "Planet Formation in AB Aurigae: Imaging of the inner gaseous Spirals observed inside the Dust Cavity," *The Astrophysical Journal*, vol. 840, p. 32, 2017.

[70] C. Papovich, I. Labbé, K. Glazebrook, R. Quadri, G. Bekiaris, M. Dickinson, *et al.*, "Large molecular gas reservoirs in ancestors of Milky Way-mass galaxies nine billion years ago," *Nature*, vol. 1, p. 0003, 2016.

[71] J. F. Gallimore, M. Elitzur, R. Maiolino, A. Marconi, C. P. O'Dea, D. Lutz, *et al.*, "High-Velocity Bipolar Molecular Emission from an AGN Torus," *The Astrophysical Journal Letters*, vol. 829, p. L7, 2016.

[72] J. Lieman-Sifry, A. M. Hughes, J. M. Carpenter, U. Gorti, A. Hales, and K. M. Flaherty, "Debris Disks in the Scorpius–Centaurus OB Association Resolved by ALMA," *The Astrophysical Journal*, vol. 828, p. 25, 2016.

[73] M. Neeleman, J. X. Prochaska, M. A. Zwaan, N. Kanekar, L. Christensen, M. Dessauges-Zavadsky, *et al.*, "First connection between cold gas in emission and absorption: CO emission from a galaxy–quasar pair," *The Astrophysical Journal Letters*, vol. 820, p. L39, 2016.

[74] C. Walsh, R. A. Loomis, K. I. Öberg, M. Kama, M. L. van't Hoff, T. J. Millar, *et al.*, "First detection of gas-phase methanol in a protoplanetary disk," *The Astrophysical Journal Letters*, vol. 823, p. L10, 2016.

[75] Y. Oya, N. Sakai, A. López-Sepulcre, Y. Watanabe, C. Ceccarelli, B. Lefloch, *et al.*, "Infalling-rotating motion and associated chemical change in the envelope of IRAS 16293-2422 Source A studied with ALMA," *Astrophys. J*, vol. 824, p. 88, 2016.

[76] L. A. Cieza, S. Casassus, J. Tobin, S. P. Bos, J. P. Williams, S. Perez, *et al.*, "Imaging the water snow-line during a protostellar outburst," *Nature*, vol. 535, pp. 258-261, 2016.

[77] T. Tsukagoshi, H. Nomura, T. Muto, R. Kawabe, D. Ishimoto, K. D. Kanagawa, *et al.*, "A gap with a deficit of large grains in the protoplanetary disk around TW Hya," *The Astrophysical Journal Letters*, vol. 829, p. L35, 2016.

[78] J. Geach, D. Narayanan, Y. Matsuda, M. Hayes, L. Mas-Ribas, M. Dijkstra, *et al.*, "ALMA Observations of Lyα Blob 1: Halo Substructure Illuminated from Within," *The Astrophysical Journal,* vol. 832, p. 37, 2016.

[79] T. Izumi, N. Kawakatu, and K. Kohno, "Do Circumnuclear Dense Gas Disks Drive Mass Accretion onto Supermassive Black Holes?," *The Astrophysical Journal,* vol. 827, p. 81, 2016.

[80] M. Kaufman, B. G. Elmegreen, C. Struck, D. M. Elmegreen, F. Bournaud, E. Brinks, *et al.*, "Ocular Shock Front in the Colliding Galaxy IC 2163," *The Astrophysical Journal,* vol. 831, p. 161, 2016.

[81] W. Rujopakarn, J. Dunlop, G. Rieke, R. Ivison, A. Cibinel, K. Nyland, *et al.*, "VLA AND ALMA IMAGING OF INTENSE GALAXY-WIDE STAR FORMATION IN z∼ 2 GALAXIES," *The Astrophysical Journal,* vol. 833, p. 12, 2016.

[82] C.-F. Lee, Z.-Y. Li, P. T. Ho, N. Hirano, Q. Zhang, and H. Shang, "First detection of equatorial dark dust lane in a protostellar disk at submillimeter wavelength," *Science Advances,* vol. 3, p. e1602935, 2017.

[83] R. Sahai, W. Vlemmings, and L. Nyman, "The Coldest Place in the Universe: Probing the Ultra-cold Outflow and Dusty Disk in the Boomerang Nebula," *The Astrophysical Journal,* vol. 841, p. 16pp, 2017.

[84] J. Bahcall, S. Kirhakos, D. Schneider, R. Davis, T. Muxlow, S. Garrington, *et al.*, "Hubble Space Telescope and MERLIN observations of the jet in 3C 273," *The Astrophysical Journal Letters,* vol. 452, p. L91, 1995.

[85] R. Conway, S. Garrington, T. Muxlow, and R. Davis, "Merlin and HST Observations of the Jet in 3C273," in *Extragalactic Radio Sources*, ed: Springer, 1996, pp. 203-204.

[86] C. Romero-Cañizales, M. Pérez-Torres, A. Alberdi, M. Argo, R. Beswick, E. Kankare, *et al.*, "e-MERLIN and VLBI observations of the luminous infrared galaxy IC 883: a nuclear starburst and an AGN candidate revealed," *Astronomy & Astrophysics,* vol. 543, p. A72, 2012.

[87] M. Giroletti, B. Marcote, M. Garrett, Z. Paragi, J. Yang, K. Hada, *et al.*, "FRB 150418: clues to its nature from European VLBI Network and e-MERLIN observations," *Astronomy & Astrophysics,* vol. 593, p. L16, 2016.

[88] M. A. Perez-Torres, A. Alberdi, C. Romero-Canizales, and M. Bondi, "Serendipitous discovery of the long-sought active galactic nucleus in Arp 299-A," *Astronomy & Astrophysics,* vol. 519, p. L5, 2010.

[89] E. K. Rotich Kipnoo, D. Kiboi Boiyo, G. M. Isoe, T. V. Chabata, R. R. G. Gamatham, A. W. R. Leitch, *et al.*, "Demonstration of Raman-based, dispersion-managed VCSEL technology for fibre-to-the-hut application," *Optical Fiber Technology,* vol. 34, pp. 1-5, 3// 2017.

[90] S. Li, C. Wang, H. Lu, and J. Zhao, "Performance evaluation at the remote site for RF frequency dissemination over fiber," *IEEE Photonics Journal*, 2017.

[91] S. Wassin, G. M. Isoe, R. R. G. Gamatham, A. W. R. Leitch, and T. B. Gibbon, "Highly accurate pulse-per-second timing distribution over optical fibre network using VCSEL side-mode injection," 2017, pp. 101290G-101290G-12.

[92] Ł. Śliwczyński, P. Krehlik, A. Czubla, Ł. Buczek, and M. Lipiński, "Dissemination of time and RF frequency via a stabilized fibre optic link over a distance of 420 km," *Metrologia,* vol. 50, p. 133, 2013.

[93] O. Lopez, A. Kanj, P.-E. Pottie, D. Rovera, J. Achkar, C. Chardonnet, *et al.*, "Simultaneous remote transfer of accurate timing and optical frequency over a public fiber network," *Applied Physics B,* vol. 110, pp. 3-6, 2013.

[94] K. W. Holman, D. D. Hudson, J. Ye, and D. J. Jones, "Remote transfer of a high-stability and ultralow-jitter timing signal," *Optics letters,* vol. 30, pp. 1225-1227, 2005.

[95] O. Lopez, A. Amy-Klein, C. Daussy, C. Chardonnet, F. Narbonneau, M. Lours, *et al.*, "86-km optical link with a resolution of 2 × 10-18 for RF frequency transfer," *The European Physical Journal D,* vol. 48, pp. 35-41, June 01 2008.

[96] B. Ning, D. Hou, T. Zheng, and J. Zhao, "Hybrid Analog-Digital Fiber-Based Radio-Frequency Signal Distribution," *IEEE Photonics Technology Letters,* vol. 25, pp. 1551-1554, 2013.

[97] C.-T. Lin, J. Chen, P.-C. Peng, C.-F. Peng, W.-R. Peng, B.-S. Chiou*, et al.*, "Hybrid optical access network integrating fiber-to-the-home and radio-over-fiber systems," *IEEE Photonics Technology Letters,* vol. 19, pp. 610-612, 2007.

[98] K. G. Baldwin, Y. He, M. Hsu, M. Wouters, M. Gray, B. J. Orr*, et al.*, "Analog and all-digital frequency distribution via optical fiber links," in *CLEO: Science and Innovations*, 2012, p. CTh4A. 2.

[99] B. Ning, S. Zhang, D. Hou, J. Wu, Z. Li, and J. Zhao, "High-precision distribution of highly stable optical pulse trains with 8.8× 10− 19 instability," *Scientific reports,* vol. 4, 2014.

[100] B. Ning, S. Zhang, D. Hou, J. Wu, Z. Li, and J. Zhao, "High-precision Distribution of Highly-stable Optical Pulse Trains with Sub-10-fs Timing Jitter," *arXiv preprint arXiv:1402.5631,* 2014.

[101] J. Kim, J. A. Cox, J. Chen, and F. X. Kärtner, "Drift-free femtosecond timing synchronization of remote optical and microwave sources," *Nature Photonics,* vol. 2, pp. 733-736, 2008.

[102] J.-F. Cliche and B. Shillue, "Applications of control Precision timing control for radioastronomy maintaining femtosecond synchronization in the atacama large millimeter array," *IEEE control systems,* vol. 26, pp. 19-26, 2006.

[103] C. Clivati, R. Ambrosini, T. Artz, A. Bertarini, C. Bortolotti, M. Frittelli*, et al.*, "A VLBI experiment using a remote atomic clock via a coherent fibre link," *Scientific Reports,* vol. 7, p. 40992, 2017.

[104] J.-F. Cliche and B. Shillue, "Precision timing control for radioastronomy: maintaining femtosecond synchronization in the Atacama Large Millimeter Array," *IEEE control systems,* vol. 26, pp. 19-26, 2006.

[105] K. G. Baldwin, Y. He, M. Hsu, M. Wouters, M. Gray, B. J. Orr*, et al.*, "Analog and all-digital frequency distribution via optical fiber links," in *Conference on Lasers and Electro-Optics 2012*, San Jose, California, 2012, p. CTh4A.2.

[106] W. Riley, "Techniques for frequency stability analysis," in *IEEE international frequency control symposium, Tampa, FL*, 2003.

[107] J. Rutman and F. Walls, "Characterization of frequency stability in precision frequency sources," *Proceedings of the IEEE,* vol. 79, pp. 952-960, 1991.

[108] J. A. Barnes, A. R. Chi, L. S. Cutler, D. J. Healey, D. B. Leeson, T. E. McGunigal*, et al.*, "Characterization of frequency stability," *IEEE transactions on instrumentation and measurement,* vol. 1001, pp. 105-120, 1971.

[109] L. Xiaohui, L. Ya, W. Danni, and B. Yujing, "Heterodyne Frequency Measurement Method Based on Virtual Instrument," in *2007 IEEE International Frequency Control Symposium Joint with the 21st European Frequency and Time Forum*, 2007, pp. 220-222.

[110] D. W. Allan, "Report on NBS dual mixer time difference system (DMTD) built for time domain measurements associated with phase 1 of GPS," *NBS IR 75 827,* 1976.

[111] W. Riley, "A Small Dual Mixer Time Difference (DMTD) Clock Measuring System," *Manual, Hamilton Technical Services Beaufort, SC,* vol. 29907, 2013.

[112] L. Sojdr, J. Cermak, and R. Barillet, "Optimization of dual-mixer time-difference multiplier," 2004.

[113] F. Nakagawa, M. Imae, Y. Hanado, and M. Aida, "Development of multichannel dual-mixer time difference system to generate UTC (NICT)," *IEEE transactions on instrumentation and measurement,* vol. 54, pp. 829-832, 2005.

[114] M. Eldesouki and M. J. Deen, "Injection locking based power amplifier," ed: Google Patents, 2015.

[115] D. Owen, "Good practice guide to phase noise measurement," *National Physical Laboratory, Middlesex, UK, Tech. Note,* vol. 68, 2004.

[116] I. Milanovic, S. Renovica, I. Župunski, M. Banović, and P. Rakonjac, "How To Measure Oscillator's Short-Term Stability Using Frequency Counter," *Electronics,* vol. 16, pp. 104-111, 2012.
[117] B. Kim, R. N. Candler, M. Hopcroft, M. Agarwal, W.-T. Park, and T. W. Kenny, "Frequency stability of wafer-scale encapsulated MEMS resonators," in *Solid-State Sensors, Actuators and Microsystems, 2005. Digest of Technical Papers. TRANSDUCERS'05. The 13th International Conference on,* 2005, pp. 1965-1968.
[118] R. E. Beehler, R. C. Mockler, and J. M. Richardson, "Cesium beam atomic time and frequency standards," *Metrologia,* vol. 1, p. 114, 1965.
[119] D. W. Allan, "Statistics of atomic frequency standards," *Proceedings of the IEEE,* vol. 54, pp. 221-230, 1966.
[120] W. J. Klepczynski, "GPS for Precise Time and Time Interval Measurement," *Global Positioning Systems: Theory and Applications,* vol. 2, 1996.
[121] S. Lea, "Limits to time variation of fundamental constants from comparisons of atomic frequency standards," *Reports on Progress in Physics,* vol. 70, p. 1473, 2007.
[122] N. Hinkley, J. Sherman, N. Phillips, M. Schioppo, N. Lemke, K. Beloy*, et al.*, "An atomic clock with 10–18 instability," *Science,* vol. 341, pp. 1215-1218, 2013.
[123] N. Ashby, T. P. Heavner, S. R. Jefferts, T. E. Parker, A. Radnaev, and Y. Dudin, "Testing local position invariance with four cesium-fountain primary frequency standards and four NIST hydrogen masers," *Physical review letters,* vol. 98, p. 070802, 2007.
[124] D. W. Allan, "Should the classical variance be used as a basic measure in standards metrology?," *IEEE Transactions on Instrumentation and Measurement,* vol. 1001, pp. 646-654, 1987.
[125] J. Rutman, "Characterization of frequency stability: A transfer function approach and its application to measurements via filtering of phase noise," *IEEE Transactions on Instrumentation and Measurement,* vol. 23, pp. 40-48, 1974.
[126] K. Iga, "Surface-emitting laser-its birth and generation of new optoelectronics field," *IEEE Journal of Selected Topics in Quantum Electronics,* vol. 6, pp. 1201-1215, 2000.
[127] E. M. Bradley, "Surface emitting laser," ed: Google Patents, 1990.
[128] H. Soda, K.-i. Iga, C. Kitahara, and Y. Suematsu, "GaInAsP/InP surface emitting injection lasers," *Japanese Journal of Applied Physics,* vol. 18, p. 2329, 1979.
[129] H. Soda, Y. Motegi, and K. Iga, "GaInAsP/InP surface emitting injection lasers with short cavity length," *IEEE Journal of Quantum Electronics,* vol. 19, pp. 1035-1041, 1983.
[130] K. Iga, S. Kinoshita, and F. Koyama, "Microcavity GalaAs/GaAs surface-emitting laser with Ith= 6 mA," *Electronics letters,* vol. 23, pp. 134-136, 1987.
[131] F. Koyama, "Recent advances of VCSEL photonics," *Journal of Lightwave Technology,* vol. 24, pp. 4502-4513, 2006.
[132] D. M. Kuchta, "High capacity VCSEL-based links," in *Optical Fiber Communications Conference and Exhibition (OFC), 2017,* 2017, pp. 1-94.
[133] R. Michalzik and K. J. Ebeling, "Operating principles of VCSELs," in *Vertical-Cavity Surface-Emitting Laser Devices*, ed: Springer, 2003, pp. 53-98.
[134] P. Moser, P. Wolf, G. Larisch, H. Li, J. A. Lott, and D. Bimberg, "Energy-efficient oxide-confined high-speed VCSELs for optical interconnects," in *Proc. SPIE,* 2014, p. 900103.
[135] H. Nasu, T. Kise, K. Nagashima, N. Nishimura, M. Funabashi, T. Suzuki*, et al.*, "VCSEL-based parallel-optical modules for> 100 Gb/s applications," in *Optical Communication (ECOC), 2014 European Conference on,* 2014, pp. 1-3.
[136] R. Rodes Lopez, J. M. Estaran Tolosa, B. Li, M. Muller, J. B. Jensen, T. Gründl*, et al.*, "100 Gb/s single VCSEL data transmission link," in *2012 Optical Fiber Communication Conference and Exposition and the National Fiber Optic Engineers Conference*.
[137] R. Szweda, "VCSEL applications diversify as technology matures," *III-Vs Review,* vol. 19, pp. 34-38, 2// 2006.

[138] R. Szweda, "VCSELs market diversifies for success," *III-Vs Review*, vol. 19, pp. 32-35, 11// 2006.

[139] P. Westbergh, J. S. Gustavsson, Å. Haglund, M. Skold, A. Joel, and A. Larsson, "High-speed, low-current-density 850 nm VCSELs," *IEEE Journal of Selected Topics in Quantum Electronics*, vol. 15, pp. 694-703, 2009.

[140] M. Crisp, R. V. Penty, I. H. White, and A. Bell, "Wideband radio over fiber distributed antenna systems for energy efficient in-building wireless communications," in *Vehicular Technology Conference (VTC 2010-Spring), 2010 IEEE 71st*, 2010, pp. 1-5.

[141] S. Blokhin, J. Lott, A. Mutig, G. Fiol, N. Ledentsov, M. Maximov, *et al.*, "Oxide-confined 850 nm VCSELs operating at bit rates up to 40 Gbit/s," *Electronics Letters*, vol. 45, pp. 501-503, 2009.

[142] E. Haglund, Å. Haglund, J. S. Gustavsson, B. Kögel, P. Westbergh, and A. Larsson, "Reducing the spectral width of high speed oxide confined VCSELs using an integrated mode filter," in *Vertical-Cavity Surface-Emitting Lasers Xvi*, 2012.

[143] J. D. Ingham, R. V. Penty, I. H. White, P. Westbergh, J. Gustavsson, A. Haglund, *et al.*, "32 Gb/s multilevel modulation of an 850 nm VCSEL for next-generation datacommunication standards," in *CLEO: Science and Innovations*, 2011, p. CWJ2.

[144] E. Kapon and A. Sirbu, "Long-wavelength VCSELs: Power-efficient answer," *Nature Photonics*, vol. 3, pp. 27-29, 2009.

[145] K. Prince, M. Ma, T. B. Gibbon, C. Neumeyr, E. Rönneberg, M. Ortsiefer, *et al.*, "Free-running 1550 nm VCSEL for 10.7 Gb/s transmission in 99.7 km PON," *Journal of Optical Communications and Networking*, vol. 3, pp. 399-403, 2011.

[146] N. Quadir, P. Ossieur, and P. D. Townsend, "A 56Gb/s PAM-4 VCSEL driver circuit," in *IET Irish Signals and Systems Conference (ISSC 2012)*, 2012, pp. 1-5.

[147] D. K. Boiyo, G. M. Isoe, R. R. G. Gamatham, A. W. R. Leitch, and T. B. Gibbon, "A 1550-nm all-optical VCSEL-to-VCSEL wavelength conversion of a 8.5-Gb/s data signal and transmission over a 24.7-km fibre," 2017, pp. 100360X-100360X-6.

[148] R. Gamatham, E. Rotich, A. Leitch, and T. Gibbon, "Fibre-to-the-Hut: Research into tailored FTTH solutions for Africa," in *AFRICON, 2013*, 2013, pp. 1-5.

[149] T. B. Gibbon, K. Prince, T. T. Pham, A. Tatarczak, C. Neumeyr, E. Rönneberg, *et al.*, "VCSEL transmission at 10Gb/s for 20km single mode fiber WDM-PON without dispersion compensation or injection locking," *Optical fiber technology*, vol. 17, pp. 41-45, 2011.

[150] G. M. Isoe, E. K. Rotich, R. R. G. Gamatham, A. W. R. Leitch, and T. B. Gibbon, "Fibre-to-the-Hut Technology: A Solution for Cheap Access for High Speed-Optical Network in South Africa," in *SAIP,2015*, 2015, pp. 440-444.

[151] G. M. Isoe, S. Wassin, D. K. Boiyo, E. K. R. Kipnoo, R. R. G. Gamatham, A. W. R. Leitch, *et al.*, "Effect of 10 Gbps Data Transmission on 1.712 GHz 1309.97 nm VCSEL Based Radio Frequency Distribution over a Single Optical Fibre for the Telescope Array," in *The annual 2016 Southern African Telecommunication Networks and Application Conference (SATNAC)*, Fancourt in George, Western Cape, South Africa, 2016, pp. 150-153.

[152] D. Li, Y. Li, J. Wu, S. Su, and J. Yu, "ESM: efficient and scalable data center multicast routing," *IEEE/ACM Transactions on Networking (TON)*, vol. 20, pp. 944-955, 2012.

[153] P. Samadi, V. Gupta, J. Xu, H. Wang, G. Zussman, and K. Bergman, "Optical multicast system for data center networks," *Optics express*, vol. 23, pp. 22162-22180, 2015.

[154] K. Tokas, C. Spatharakis, I. Kanakis, N. Iliadis, P. Bakopoulos, H. Avramopoulos, *et al.*, "A scalable optically-switched datacenter network with multicasting," in *2016 European Conference on Networks and Communications (EuCNC)*, 2016, pp. 265-270.

[155] B. Whetten, L. Vicisano, R. Kermode, M. Handley, S. Floyd, and M. Luby, "Reliable multicast transport building blocks for one-to-many bulk-data transfer," 2070-1721, 2000.

[156] (2016). *IEEE P802.3bs 400 Gb/s Ethernet Task Force*. Available: http://www.ieee802.org/3/bs/

[157] S. Aleksic and M. Fiorani, "The Future of Switching in Data Centers," in *Optical Switching in Next Generation Data Centers*, ed: Springer, 2018, pp. 301-328.

[158] Infiniband. *Infiniband Roadmap*. Available: http://www.infinibandta.org/content/pages.php?pg=technology%20_overview

[159] F. Channel. *Fiber Channel Roadmap*. Available: http://brechannel.org/wp-content/uploads/2015/11/FCIA RoadMap Front.jpg

[160] G.-K. Chang, L. Cheng, M. Xu, and D. Guidotti, "Integrated fiber-wireless access architecture for mobile backhaul and fronthaul in 5G wireless data networks," in *Avionics, Fiber-Optics and Photonics Technology Conference (AVFOP), 2014 IEEE*, 2014, pp. 49-50.

[161] A. Ibaraki, K. Kawashima, K. Furusawa, T. Ishikawa, T. Yamaguchi, and T. Niina, "Buried heterostructure GaAs/GaAlAs distributed Bragg reflector surface emitting laser with very low threshold (5.2 mA) under room temperature CW conditions," *Japanese Journal of Applied Physics*, vol. 28, p. L667, 1989.

[162] J. Jewell, A. Scherer, S. McCall, Y. Lee, S. Walker, J. Harbison, *et al.*, "Low-threshold electrically pumped vertical-cavity surface-emitting microlasers," *Electronics Letters*, vol. 25, pp. 1123-1124, 1989.

[163] S. M. Sze and K. K. Ng, *Physics of semiconductor devices*: John wiley & sons, 2006.

[164] D. Huffaker, D. Deppe, K. Kumar, and T. Rogers, "Native-oxide defined ring contact for low threshold vertical-cavity lasers," *Applied Physics Letters*, vol. 65, pp. 97-99, 1994.

[165] R. Michalzik, *VCSELs: fundamentals, technology and applications of vertical-cavity surface-emitting lasers* vol. 166: Springer, 2012.

[166] L. A. Coldren, S. W. Corzine, and M. L. Mashanovitch, *Diode lasers and photonic integrated circuits* vol. 218: John Wiley & Sons, 2012.

[167] J. M. Senior and M. Y. Jamro, *Optical fiber communications: principles and practice*: Pearson Education, 2009.

[168] H.-Y. Kao, C.-T. Tsai, S.-F. Leong, C.-Y. Peng, Y.-C. Chi, J. J. Huang, *et al.*, "Comparison of single-/few-/multi-mode 850 nm VCSELs for optical OFDM transmission," *Optics Express*, vol. 25, pp. 16347-16363, 2017.

[169] M. Hari, "Advanced Modulation Formats for High-Bit-Rate Optical Networks," PhD, School of Electrical and computer Engineering, Georgia Institute of Technology, 2008.

[170] K. Grobe, M. Roppelt, A. Autenrieth, J.-P. Elbers, and M. Eiselt, "Cost and energy consumption analysis of advanced WDM-PONs," *IEEE Communications Magazine*, vol. 49, 2011.

[171] R. Hui, S. Zhang, B. Zhu, R. Huang, C. Allen, and D. Demarest, "Advanced optical modulation formats and their comparison in fiber-optic systems," 2004.

[172] P. J. Winzer and R.-J. Essiambre, "Advanced optical modulation formats," *Proceedings of the IEEE*, vol. 94, pp. 952-985, 2006.

[173] D. J. Law, W. W. Diab, A. Healey, S. B. Carlson, V. Maguire, J. D'Ambrosia, *et al.*, "IEEE 802.3 industry connections Ethernet bandwidth assessment," *Recuperado en http://www. ieee802. org/3/ad_hoc/bwa/BWA_Report. pdf*, 2012.

[174] P. Dong, J. Lee, Y.-K. Chen, L. L. Buhl, S. Chandrasekhar, J. H. Sinsky, *et al.*, "Four-channel 100-Gb/s per channel discrete multitone modulation using silicon photonic integrated circuits," *Journal of Lightwave Technology*, vol. 34, pp. 79-84, 2016.

[175] Y. Matsui, T. Pham, T. Sudo, G. Carey, B. Young, and C. Roxlo, "112-Gb/s WDM link using two directly modulated Al-MQW BH DFB lasers at 56 Gb/s," in *Optical Fiber Communication Conference*, 2015, p. Th5B. 6.

[176] M. Mazzini, M. Traverso, M. Webster, C. Muzio, S. Anderson, P. Sun, *et al.*, "25GBaud PAM-4 error free transmission over both single mode fiber and multimode fiber in a QSFP form factor based on silicon photonics," in *Optical Fiber Communications Conference and Exhibition (OFC), 2015*, 2015, pp. 1-3.

[177] J. Lee, S. Shahramian, N. Kaneda, Y. Baeyens, J. Sinsky, L. Buhl, *et al.*, "Demonstration of 112-Gbit/s optical transmission using 56GBaud PAM-4 driver and clock-and-data recovery ICs," in *Optical Communication (ECOC), 2015 European Conference on*, 2015, pp. 1-3.

[178] P. Westbergh, J. S. Gustavsson, B. Kogel, A. Haglund, A. Larsson, A. Mutig, *et al.*, "40 Gbit/s error-free operation of oxide-confined 850 nm VCSEL," *Electronics Letters,* vol. 46, pp. 1014-1016, 2010.

[179] C.-T. Tsai, S. Chang, C.-Y. Pong, S.-F. Liang, Y.-C. Chi, C.-H. Wu, *et al.*, "RIN suppressed multimode 850-nm VCSEL for 56-Gbps 16-QAM OFDM and 22-Gbps PAM-4 transmission," in *Optical Fiber Communications Conference and Exhibition (OFC), 2016*, 2016, pp. 1-3.

[180] K. Iga and H. Li, *Vertical-cavity surface-emitting laser devices*: Springer, 2003.

[181] D. Kuchta, A. V. Rylyakov, C. L. Schow, J. Proesel, C. Baks, P. Westbergh, *et al.*, "64Gb/s Transmission over 57m MMF using an NRZ Modulated 850nm VCSEL," in *Optical Fiber Communications Conference and Exhibition (OFC), 2014*, 2014, pp. 1-3.

[182] P. Westbergh, R. Safaisini, E. Haglund, B. Kogel, J. S. Gustavsson, A. Larsson, *et al.*, "High-speed 850 nm VCSELs with 28 GHz modulation bandwidth operating error-free up to 44 Gbit/s," *Electronics Letters,* vol. 48, pp. 1145-1147, 2012.

[183] A. Gholami, D. Molin, and P. Sillard, "Compensation of chromatic dispersion by modal dispersion in MMF-and VCSEL-based gigabit ethernet transmissions," *IEEE Photonics Technology Letters,* vol. 21, pp. 645-647, 2009.

[184] C. Xie, P. Dong, P. Winzer, C. Gréus, M. Ortsiefer, C. Neumeyr, *et al.*, "960-km SSMF transmission of 105.7-Gb/s PDM 3-PAM using directly modulated VCSELs and coherent detection," *Optics express,* vol. 21, pp. 11585-11589, 2013.

[185] M. P. Tan, S. T. M. Fryslie, J. A. Lott, N. N. Ledentsov, D. Bimberg, and K. D. Choquette, "Error-free transmission over 1-km OM4 multimode fiber at 25 Gb/s using a single mode photonic crystal vertical-cavity surface-emitting laser," *IEEE Photonics Technology Letters,* vol. 25, pp. 1823-1825, 2013.

[186] R. Safaisini, E. Haglund, P. Westbergh, J. S. Gustavsson, and A. Larsson, "20 Gbit/s data transmission over 2 km multimode fibre using 850 nm mode filter VCSEL," *Electronics Letters,* vol. 50, pp. 40-42, 2014.

[187] C. Xie, S. Spiga, P. Dong, P. J. Winzer, M. Bergmann, B. Kögel, *et al.*, "Generation and transmission of a 400-Gb/s PDM/WDM signal using a monolithic 2x4 VCSEL array and coherent detection," in *Optical Fiber Communication Conference*, 2014, p. Th5C. 9.

[188] D. Kuchta, A. Rylyakov, F. Doany, C. Schow, J. Proesel, C. Baks, *et al.*, "A 71 Gb/s NRZ Modulated 850 nm VCSEL-based Optical Link," *IEEE Photonics Technology Letters,* vol. 27, pp. 577-580, 2015.

[189] P. Moser, J. A. Lott, and D. Bimberg, "Energy efficiency of directly modulated oxide-confined high bit rate 850-nm VCSELs for optical interconnects," *IEEE Journal of Selected Topics in Quantum Electronics,* vol. 19, pp. 1702212-1702212, 2013.

[190] S.-Y. Lin, Y.-C. Su, Y.-C. Li, H.-L. Wang, G.-C. Lin, S.-M. Chen, *et al.*, "10-Gbit/s direct modulation of a TO-56-can packed 600-μm long laser diode with 2% front-facet reflectance," *Optics express,* vol. 21, pp. 25197-25209, 2013.

[191] K. Szczerba, P. Westbergh, E. Agrell, M. Karlsson, P. A. Andrekson, and A. Larsson, "Comparison of intersymbol interference power penalties for OOK and 4-PAM in short-range optical links," *Journal of Lightwave Technology,* vol. 31, pp. 3525-3534, 2013.

[192] F. Breyer, J. Lee, S. Randel, and N. Hanik, "Comparison of OOK-and PAM-4 modulation for 10 Gbit/s transmission over up to 300 m polymer optical fiber," in *Optical Fiber Communication Conference*, 2008, p. OWB5.

[193] J. Lavrencik, S. Varughese, V. A. Thomas, G. Landry, Y. Sun, R. Shubochkin, *et al.*, "100Gbps PAM-4 transmission over 100m OM4 and wideband fiber using 850nm VCSELs," in *ECOC 2016; 42nd European Conference on Optical Communication; Proceedings of*, 2016, pp. 1-3.

[194] C. Kottke, C. Caspar, V. Jungnickel, R. Freund, M. Agustin, and N. Ledentsov, "High speed 160 Gb/s DMT VCSEL transmission using pre-equalization," in *Optical Fiber Communication Conference*, 2017, p. W4I. 7.

[195] M. Müller, W. Hofmann, A. Nadtochiy, A. Mutig, G. Böhm, M. Ortsiefer, *et al.*, "1.55 µm high-speed VCSELs enabling error-free fiber-transmission up to 25 Gbit/s," in *Semiconductor Laser Conference (ISLC), 2010 22nd IEEE International*, 2010, pp. 156-157.

[196] C. Xie, P. Dong, S. Randel, D. Pilori, P. Winzer, S. Spiga, *et al.*, "Single-VCSEL 100-Gb/s short-reach system using discrete multi-tone modulation and direct detection," in *Optical Fiber Communications Conference and Exhibition (OFC), 2015*, 2015, pp. 1-3.

[197] R. Rodes, M. Müeller, B. Li, J. Estaran, J. B. Jensen, T. Gruendl, *et al.*, "High-speed 1550 nm VCSEL data transmission link employing 25 GBd 4-PAM modulation and hard decision forward error correction," *Journal of Lightwave Technology,* vol. 31, pp. 689-695, 2013.

[198] F. Karinou, C. Prodaniuc, N. Stojanovic, M. Ortsiefer, A. Daly, R. Hohenleitner, *et al.*, "Directly PAM-4 Modulated 1530-nm VCSEL Enabling 56 Gb/s/$\lambda $ Data-Center Interconnects," *IEEE Photonics Technology Letters,* vol. 27, pp. 1872-1875.

[199] N. Eiselt, J. Wei, H. Griesser, A. Dochhan, M. Eiselt, J.-P. Elbers, *et al.*, "First real-time 400G PAM-4 demonstration for inter-data center transmission over 100 km of SSMF at 1550 nm," in *Optical Fiber Communications Conference and Exhibition (OFC), 2016*, 2016, pp. 1-3.

[200] K. Szczerba, P. Westbergh, J. Karout, J. Gustavsson, Å. Haglund, M. Karlsson, *et al.*, "30 Gbps 4-PAM transmission over 200 m of MMF using an 850 nm VCSEL," *Optics express,* vol. 19, pp. B203-B208, 2011.

[201] F. Tan, M.-K. Wu, M. Liu, M. Feng, and N. Holonyak, "850 nm oxide-VCSEL with low relative intensity noise and 40 Gb/s error free data transmission," *IEEE Photonics Technology Letters,* vol. 26, pp. 289-292, 2014.

[202] F. Karinou, C. Prodaniuc, N. Stojanovic, M. Ortsiefer, A. Daly, R. Hohenleitner, *et al.*, "Directly PAM-4 Modulated 1530-nm VCSEL Enabling 56 Gb/s/$\ lambda $ Data-Center Interconnects," *IEEE Photonics Technology Letters,* vol. 27, pp. 1872-1875.

[203] K. Szczerba, P. Westbergh, M. Karlsson, P. Andrekson, and A. Larsson, "60 Gbits error-free 4-PAM operation with 850 nm VCSEL," *Electronics Letters,* vol. 49, pp. 953-955, 2013.

[204] K. Szczerba, P. Westbergh, M. Karlsson, P. A. Andrekson, and A. Larsson, "70 Gbps 4-PAM and 56 Gbps 8-PAM using an 850 nm VCSEL," *Journal of Lightwave Technology,* vol. 33, pp. 1395-1401, 2015.

[205] P. Westbergh, R. Safaisini, E. Haglund, J. S. Gustavsson, A. Larsson, M. Geen, *et al.*, "High-Speed Oxide Confined 850-nm VCSELs Operating Error-Free at 40 Gb/s up to 85$^{\circ}{\rm C} $," *IEEE Photonics Technology Letters,* vol. 25, pp. 768-771.

[206] G. M. Isoe, D. K. Boiyo, S. Wassin, R. R. G. Gamatham, A. W. R. Leitch, and T. B. Gibbon, "Effect of 1.712 GHz RF-Clock Signal Distribution on 10 Gbps 1550.89 nm VCSEL Based Transmission over Single Optical Fibre for Square Kilometre Telescope Array," in *61 South African Institute of Physics (SAIP),* university of cape town, South frica, 2016.

[207] G. M. Isoe, S. Wassin, R. R. G. Gamatham, A. W. R. Leitch, and T. B. Gibbon, "Simultaneous 10 Gbps data and polarization-based pulse-per-second clock transmission using a single VCSEL for high-speed optical fibre access networks," 2017, pp. 101290F-101290F-12.

[208] G. Breed, "A tutorial introduction to optical modulation techniques," *High frequency design optical modulation, From May,* 2007.

[209] T. Yamamoto, "High-speed directly modulated lasers," in *Optical Fiber Communication Conference and Exposition (OFC/NFOEC), 2012 and the National Fiber Optic Engineers Conference*, 2012, pp. 1-39.

[210] C. H. Cox, G. E. Betts, and L. M. Johnson, "An analytic and experimental comparison of direct and external modulation in analog fiber-optic links," *IEEE Transactions on microwave theory and techniques*, vol. 38, pp. 501-509, 1990.

[211] F. Chang, K. Onohara, and T. Mizuochi, "Forward error correction for 100 G transport networks," *IEEE Communications Magazine*, vol. 48, 2010.

[212] M. Ariga, M. Arai, T. Kageyama, C. Setiagung, Y. Ikenaga, N. Iwai*, et al.*, "Noise characteristics of GaInNAsSb 1300-nm-range VCSEL with optical feedback for isolator-free module," *IEEE Journal of selected topics in quantum electronics,* vol. 11, pp. 1074-1078, 2005.

[213] W. Soenen, R. Vaernewyck, X. Yin, S. Spiga, M.-C. Amann, G. Van Steenberge*, et al.*, "56 Gb/s PAM-4 driver IC for long-wavelength VCSEL transmitters," in *ECOC 2016; 42nd European Conference on Optical Communication; Proceedings of*, 2016, pp. 1-3.

[214] N. Eiselt, H. Griesser, J. Wei, A. Dochhan, R. Hohenleitner, M. Ortsiefer*, et al.*, "Experimental demonstration of 56 Gbit/s PAM-4 over 15 km and 84 Gbit/s PAM-4 over 1 km SSMF at 1525 nm using a 25G VCSEL," in *ECOC 2016; 42nd European Conference on Optical Communication; Proceedings of*, 2016, pp. 1-3.

[215] N. Eiselt, H. Griesser, J. Wei, R. Hohenleitner, A. Dochhan, M. Ortsiefer*, et al.*, "Experimental Demonstration of 84 Gb/s PAM-4 Over up to 1.6 km SSMF Using a 20-GHz VCSEL at 1525 nm," *Journal of Lightwave Technology,* vol. 35, pp. 1342-1349, 2017.

[216] G. M. Isoe, D. K. Boiyo, S. Wassin, R. R. G. Gamatham, A. W. R. Leitch, and T. B. Gibbon, "Transmission performance of 10 Gbps OOK, 15 Gbps 2-PAM and 20 Gbps 4-PAM data signals over 11 km using a 1310 nm VCSEL," presented at the The 62 Annual conferecne of the South African Institute of Physics SAIP 2017), the departement of physics Stellenbosch university, 2017.

[217] G. M. Isoe, S. Wassin, R. R. G. Gamatham, A. W. R. Leitch, and T. B. Gibbon, "High Capacity Data Centre Network: Simultaneous 4-PAM Data at 20 Gbps and 2 GHz Phase Modulated RF Clock Signal over a Single VCSEL Carrier," presented at the The annual 2017 Southern African Telecommunication Networks and Application Conference (SATNAC), Freedom of the Seas, Royal Caribbean International, Barcelona, Spain, 2017.

[218] G. M. Isoe, S. Wassin, R. R. G. Gamatham, A. W. R. Leitch, and T. B. Gibbon, "A high capacity data centre network: simultaneous 4-PAM data at 20 Gbps and 2 GHz phase modulated RF clock signal over a single VCSEL carrier," *Journal of Modern Optics,* vol. 64, pp. 2336-2344, 2017.

[219] G. Isoe, S. Wassin, R. Gamatham, A. Leitch, and T. Gibbon, "Capacity upgrade in short-reach optical fibre networks: simultaneous 4-PAM 20 Gbps data and polarization-modulated PPS clock signal using a single VCSEL carrier," *Journal of Modern Optics,* vol. 64, pp. 2245-2254, 2017.

[220] K. Szczerba, P. Westbergh, J. Karout, J. S. Gustavsson, Å. Haglund, M. Karlsson*, et al.*, "4-PAM for high-speed short-range optical communications," *Journal of Optical Communications and Networking,* vol. 4, pp. 885-894, 2012.

[221] J. M. Castro, R. Pimpinella, B. Kose, Y. Huang, M. Bigot, and P. Sillard, "200m 2x50Gbps PAM-4 SWDM transmission over WideBand Multimode Fiber using VCSELs and pre-distortion signal," in *Optical Fiber Communication Conference*, 2016, p. Tu2G. 2.

[222] A. J. Van Doorn, M. Van Exter, and J. Woerdman, "Elasto-optic anisotropy and polarization orientation of vertical-cavity surface-emitting semiconductor lasers," *Applied physics letters,* vol. 69, pp. 1041-1043, 1996.

[223] K. Panajotov, B. Ryvkin, J. Danckaert, M. Peeters, H. Thienpont, and I. Veretennicoff, "Polarization switching in VCSEL's due to thermal lensing," *IEEE Photonics Technology Letters,* vol. 10, pp. 6-8, 1998.

[224] K. D. Choquette, D. Richie, and R. Leibenguth, "Temperature dependence of gain-guided vertical-cavity surface emitting laser polarization," *Applied physics letters,* vol. 64, pp. 2062-2064, 1994.

[225] K. D. Choquette, K. Lear, R. Leibenguth, and M. Asom, "Polarization modulation of cruciform vertical-cavity laser diodes," *Applied physics letters,* vol. 64, pp. 2767-2769, 1994.

[226] J. Martin-Regalado, F. Prati, M. San Miguel, and N. Abraham, "Polarization switching in quantum-well vertical-cavity surface-emitting lasers," *Optics letters,* vol. 21, pp. 351-353, 1996.

[227] A. Valle, L. Pesquera, and K. Shore, "Polarization behavior of birefringent multitransverse mode vertical-cavity surface-emitting lasers," *IEEE Photonics Technology Letters,* vol. 9, pp. 557-559, 1997.

[228] A. Quirce, P. Pérez, A. Popp, A. Valle, L. Pesquera, Y. Hong, *et al.*, "Theoretical and experimental study of polarization switching in long-wavelength VCSELs subject to parallel optical injection," 2016, pp. 98920Q-98920Q-9.

[229] P. Pérez, H. Lin, Á. Valle, and L. Pesquera, "Polarization dynamics induced by orthogonal optical injection close to the lasing mode of a single-transverse-mode VCSEL," *Journal of the Optical Society of America B,* vol. 31, pp. 2901-2907, 2014/11/01 2014.

[230] J. Martin-Regalado, S. Balle, M. San Miguel, A. Valle, and L. Pesquera, "Polarization and transverse-mode selection in quantum-well vertical-cavity surface-emitting lasers: Index-and gain-guided devices," *Quantum and Semiclassical Optics: Journal of the European Optical Society Part B,* vol. 9, p. 713, 1997.

[231] J. Martin-Regalado, F. Prati, M. San Miguel, and N. Abraham, "Polarization properties of vertical-cavity surface-emitting lasers," *IEEE Journal of Quantum Electronics,* vol. 33, pp. 765-783, 1997.

[232] R. Mueller, A. Klehr, A. Valle, J. Sarma, and K. Shore, "Effects of spatial hole burning on polarization dynamics in edge-emitting and vertical-cavity surface-emitting laser diodes," *Semiconductor science and technology,* vol. 11, p. 587, 1996.

[233] H. Kawaguchi, I. Hidayat, Y. Takahashi, and Y. Yamayoshi, "Pitchfork bifurcation polarisation bistability in vertical-cavity surface-emitting lasers," *Electronics letters,* vol. 31, pp. 109-111, 1995.

[234] M. Sondermann, M. Weinkath, and T. Ackemann, "Polarization switching to the gain disfavored mode in vertical-cavity surface-emitting lasers," *IEEE journal of quantum electronics,* vol. 40, pp. 97-104, 2004.

[235] F. Robert, P. Besnard, M.-L. CharéS, and G. Stephan, "Polarization control in a vertical cavity surface emitting laser submitted to optical feedback," in *Annales des télécommunications*, 1997, pp. 575-587.

[236] Z. G. Pan, S. Jiang, M. Dagenais, R. A. Morgan, K. Kojima, M. T. Asom, *et al.*, "Optical injection induced polarization bistability in vertical-cavity surface-emitting lasers," *Applied physics letters,* vol. 63, pp. 2999-3001, 1993.

[237] V. Ramaswamy, W. G. French, and R. Standley, "Polarization characteristics of noncircular core single-mode fibers," *Applied optics,* vol. 17, pp. 3014-3017, 1978.

[238] M. Travagnin, "Misaligned anisotropies and nonlinear polarization effects in vertical-cavity surface-emitting lasers," *Quantum and Semiclassical Optics: Journal of the European Optical Society Part B,* vol. 10, p. 223, 1998.

[239] R. W. Boyd, "Nonlinear Optics (Academic, New York, 1992)," *Chap,* vol. 6, pp. 241-257, 1992.

[240] R. W. Boyd, *Nonlinear Optics*, 2nd ed. San Diego: Academic Press, 2003.

[241] T. Schneider, *Nonlinear Optics in Telecommunications*: Springer, 2004.

[242] Y. R. Shen, *The Principles of Nonlinear Optics*. New York: Wiley, 1984.

[243] S. Miller, *Optical fiber telecommunications*: Elsevier, 2012.

[244] G. P. Agrawal, *Fiber-optic communication systems* vol. 222: John Wiley & Sons, 2012.

[245] (29/08/2017). *EIA/TIA 568 For Fiber Optics, The Fiber Optic Association - Tech Topics*. Available: http://www.thefoa.org/tech/tia568b3.htm

[246] J. Gordon and H. Kogelnik, "PMD fundamentals: Polarization mode dispersion in optical fibers," *Proceedings of the National Academy of Sciences*, vol. 97, pp. 4541-4550, 2000.

[247] C. Poole and R. Wagner, "Phenomenological approach to polarisation dispersion in long single-mode fibres," *Electronics Letters,* vol. 22, pp. 1029-1030, 1986.

[248] P. Wai and C. Menyak, "Polarization mode dispersion, decorrelation, and diffusion in optical fibers with randomly varying birefringence," *Journal of Lightwave Technology,* vol. 14, pp. 148-157, 1996.

[249] H. Kogelnik, R. M. Jopson, and L. E. Nelson, "Polarization-mode dispersion," in *Optical Fiber Telecommunications IV-B (Fourth Edition)*, ed: Elsevier, 2002, pp. 725-861.

[250] J. N. Ross, "Birefringence measurement in optical fibers by polarization-optical time-domain reflectometry," *Applied optics,* vol. 21, pp. 3489-3495, 1982.

[251] E. Brinkmeyer, "Forward-backward transmission in birefringent single-mode fibers: interpretation of polarization-sensitive measurements," *Optics letters,* vol. 6, pp. 575-577, 1981.

[252] W. Nakwaski, "Thermal aspects of efficient operation of vertical-cavity surface-emitting lasers," *Optical and Quantum Electronics,* vol. 28, pp. 335-352, 1996.

[253] R. B. Boone, K. A. Galvin, M. B. Coughenour, J. W. Hudson, P. J. Weisberg, C. H. Vogel*, et al.*, "Ecosystem modeling adds value to a South African climate forecast," *Climatic Change,* vol. 64, pp. 317-340, 2004.

[254] X. Cheng, Y. J. Wen, Z. Xu, X. Shao, Y. Wang, and Y.-k. Yeo, "10-Gb/s WDM-PON transmission using uncooled, directly modulated free-running 1.55-μm VCSELs," in *2008 34th European Conference on Optical Communication*.

[255] K.-D. Langer, J. Vathke, K. Habel, and C. Arellano, "Recent developments in WDM-PON technology," in *Transparent Optical Networks, 2006 International Conference on*, 2006, pp. 12-13.

[256] OFS. (2014, 2017-04-21). *OFS TrueWave RS low water peak fiber*. Available: http://fiber-optic-catalog.ofsoptics.com/Asset/TrueWaveRSLWP-120-web.pdf

[257] W. Freude, R. Schmogrow, B. Nebendahl, M. Winter, A. Josten, D. Hillerkuss*, et al.*, "Quality metrics for optical signals: eye diagram, Q-factor, OSNR, EVM and BER," in *Transparent Optical Networks (ICTON), 2012 14th International Conference on*, 2012, pp. 1-4.

[258] G. Breed, "Analyzing signals using the eye diagram," 2005.

[259] J. Lee, J. Kim, G. Ji, H. Kim, and Y. Eo, "Efficient eye-diagram determination technique of non-linearly-switching coupled-data links under power and ground fluctuation noises," in *SoC Design Conference (ISOCC), 2014 International*, 2014, pp. 122-123.

[260] J. Lee and Y. Eo, "An efficient eye-diagram determination technique for multi-coupled interconnect lines," in *Power and Timing Modeling, Optimization and Simulation (PATMOS), 2013 23rd International Workshop on*, 2013, pp. 185-190.

[261] Anritsu. (2017-06-18). *Understanding Eye Pattern Measurements Application Note*. Available: rintintin.colorado.edu/~gifford/5830-AWL/Anritsu%20Eye%20Diagram.pdf

[262] Tektronix. (2017-06-18). *Anatomy of an Eye Diagram*. Available: http://www.montana.edu/aolson/eele445/homework_labs/Tektronix_eyediagram.pdf

[263] E. G. Najle and R. M. Buckley, "Phase noise measurements utilizing a frequency down conversion/multiplier, direct spectrum measurement technique," ed: Google Patents, 1994.

[264] D. B. Sullivan, Allan, David W, Howe, David A, Walls, Fred L, *Characterization of clocks and oscillators*. Time and Frequency Division Center for Atomic, Molecular, and Optical Physics National Measurement Laboratory National Institute of Standards and Technology Boulder, Colorado 80303-3328: U.S. DEPARTMENT OF COMMERCE,NATIONAL INSTITUTE OF STANDARDS AND TECHNOLOGY, March 1990.

[265] D. Sullivan, Allan, DW, Howe, DA, Walls, EL, "Characterization of Clocks and Oscillators," *National Institute of Standards and Technology Technical Note 1337,* vol. 1337, pp. 1 - 352, 1974.

[266] P. Pérez, A. Valle, I. Noriega, and L. Pesquera, "Measurement of the intrinsic parameters of single-mode VCSELs," *Journal of Lightwave Technology,* vol. 32, pp. 1601-1607, 2014.

[267] G. M. Isoe, S. Wassin, R. R. G. Gamatham, A. W. R. Leitch, and T. B. Gibbon, "Capacity upgrade in short-reach optical fibre networks: simultaneous 4-PAM 20 Gbps data and polarization-modulated PPS clock signal using a single VCSEL carrier," *Journal of Modern Optics,* pp. 1-10, 2017.

[268] U. Schmid, M. Horauer, and N. Kero, "How to distribute GPS-time over COTS-based LANs," DTIC Document1999.

[269] S. inc., *FS725 Rubidium Frequency Standard Operation and Service Manual* vol. Version 1.3. 1290-D Reamwood Avenue, Sunnyvale, California 94089: stanford research systems, 2015.

[270] S. Chandrasekhar, C. Doerr, L. Buhl, Y. Matsui, D. Mahgerefteh, X. Zheng*, et al.*, "Repeaterless transmission with negative penalty over 285 km at 10 Gb/s using a chirp managed laser," *IEEE photonics technology letters,* vol. 17, pp. 2454-2456, 2005.

[271] T. L. Koch and R. Linke, "Effect of nonlinear gain reduction on semiconductor laser wavelength chirping," *Applied Physics Letters,* vol. 48, pp. 613-615, 1986.

[272] Y. Matsui, D. Mahgerefteh, X. Zheng, C. Liao, Z. F. Fan, K. McCallion*, et al.*, "Chirp-managed directly modulated laser (CML)," *IEEE Photonics Technology Letters,* vol. 18, pp. 385-387, 2006.

[273] Photline. (2017-05-17). *LASER COMPONENTS Deutschland*. Available: https://www.lasercomponents.com/de/?embedded=1&file=fileadmin/user_upload/home/Datasheets/ixblue/modbox-an-1550nm-40g.pdf&no_cache=1

[274] Y. Shibata and T. Yasui, "Lossless Operation in InP Mach-Zehnder Modulator Monolithically Integrated with Semiconductor Optical Amplifier," in *Semiconductor Technologies*, ed: InTech, 2010.

[275] J. Svarny, "Bias driver of the Mach–Zehnder intensity electro–optic modulator, based on harmonic analysis," *Advances in robotics, mechatronics and circuits,* pp. 184-189, 2014.

[276] G. L. Gilad Goldfarb, "BER estimation of QPSK homodyne detection with carrier phase estimation using digital signal processing," *Optical Society of America*, vol. Vol. 14, 4 September 2006 2006.

[277] W. D. S. Algie L. Lance, Frederik Labaar, "Phase Noise and AM Noise Measurements in the Frequency Domain," *infrared and millimeter waves,* vol. II, pp. 239-289, 1984.

[278] W. L. Koontz and D. Mandloi, "Application of optical system simulation software in a fiber optic telecommunications program," in *Photonics North*, 2004, pp. 705-712.

[279] X. Cheng, Y. J. Wen, Z. Xu, X. Shao, Y. Wang, and Y.-k. Yeo, "10-Gb/s WDM-PON transmission using uncooled, directly modulated free-running 1.55-μm VCSELs," in *2008 34th European Conference on Optical Communication*, 2008.

[280] T. B. Gibbon, K. Prince, C. Neumeyr, E. Rönneberg, M. Ortsiefer, and I. Tafur Monroy, "10 Gb/s 1550 nm VCSEL Transmission over 23.6 km SMF with No Dispersion Compensation and No Injection Locking for WDM PONs," in *National Fiber Optic Engineers Conference*, San Diego, California, 2010, p. JThA30.

[281] F. Karinou, L. Deng, R. R. Lopez, K. Prince, J. B. Jensen, and I. T. Monroy, "Performance comparison of 850-nm and 1550-nm VCSELs exploiting OOK, OFDM, and 4-PAM over SMF/MMF links for low-cost optical interconnects," *Optical Fiber Technology,* vol. 19, pp. 206-212, 2013.

[282] T. Y. Elganimi, "Performance comparison between OOK, PPM and pam modulation schemes for free space optical (FSO) communication systems: analytical study," *International Journal of Computer Applications,* vol. 79, 2013.

[283] H.-H. Lu, C.-Y. Li, C.-M. Ho, M.-T. Cheng, X.-Y. Lin, Z.-Y. Yang*, et al.*, "64 Gb/s PAM4 VCSEL-based FSO link," *Optics Express,* vol. 25, pp. 5749-5757, 2017.

[284] R. Motaghiannezam, I. Lyubomirsky, H. Daghighian, C. Kocot, T. Gray, J. Tatum*, et al.*, "Four 45 Gbps PAM4 VCSEL based transmission through 300 m wideband OM4 fiber over SWDM4 wavelength grid," *Optics Express,* vol. 24, pp. 17193-17199, 2016.

[285] R. Motaghiannezam, T. Pham, A. Chen, T. Du, C. Kocot, J. Xu, *et al.*, "52 Gbps PAM4 receiver sensitivity study for 400GBase-LR8 system using directly modulated laser," *Optics express,* vol. 24, pp. 7374-7380, 2016.

[286] K. Szczerba, M. Karlsson, P. A. Andrekson, and A. Larsson, "Intersymbol interference penalties for OOK and 4-PAM in short-range optical communications," in *Optical Fiber Communication Conference*, 2013, p. OW4A. 3.

[287] K. Szczerba, P. Westbergh, M. Karlsson, P. Andrekson, and A. Larsson, "60 Gbits error-free 4-PAM operation with 850 nm VCSEL," *Electronics Letters,* vol. 49, p. 1, 2013.

[288] C. Yang, R. Hu, M. Luo, Q. Yang, C. Li, H. Li, *et al.*, "IM/DD-based 112-Gb/s/lambda PAM-4 transmission using 18-Gbps DML," *IEEE Photonics Journal,* vol. 8, pp. 1-7, 2016.

[289] S. Zhou, X. Li, L. Yi, Q. Yang, and S. Fu, "Transmission of 2× 56 Gb/s PAM-4 signal over 100 km SSMF using 18 GHz DMLs," *Optics letters,* vol. 41, pp. 1805-1808, 2016.

[290] P. Technologies. MODBOX-AN-1550nm-PM-40G [Online]. Available: https://www.lasercomponents.com/de/?embedded=1&file=fileadmin/user_upload/home/Datasheets/ixblue/modbox-an-1550nm-40g.pdf&no_cache=1

[291] G. T. Reed, G. Mashanovich, F. Gardes, and D. Thomson, "Silicon optical modulators," *Nature photonics,* vol. 4, pp. 518-526, 2010.

[292] Y. Shibata and T. Yasui, *Lossless Operation in InP Mach-Zehnder Modulator Monolithically Integrated with Semiconductor Optical Amplifier*.

[293] G. M. Isoe, S. Wassin, R. R. G. Gamatham, A. W. R. Leitch, and T. B. Gibbon, "A high capacity data centre network: Simultaneous 4-PAM data at 20 Gbps and 2 GHz phase modulated RF clock signal over a single VCSEL carrier," *Journal of Modern Optics*.

[294] R. Exel and F. Ring, "Direct-digital time-domain oscillator stability measurement," in *Microelectronic Systems Symposium (MESS), 2014*, 2014, pp. 1-5.

[295] J. Anthes, "OOK, ASK and FSK Modulation in the Presence of an Interfering signal," *RF Monolithics,* 2004.

[296] G. Isoe, K. Muguro, and D. Waswa, "Noise Figure Analysis of Distributed Fibre Raman Amplifier."

[297] G. Isoe, K. Muguro, D. Waswa, D. Osiemo, E. Kirui, H. Cherutoi, *et al.*, "Forward Raman Amplification Characterization in Optical Networks," in *Proceedings of Sustainable Research and Innovation Conference*, 2014, pp. 251-253.

[298] G. M. Isoe, K. M. Muguro, D. W. Waswa, E. K. R. Kipnoo, T. B. Gibbon, and A. W. R. Leitch, "Effects of Double Rayleigh Scattering in Fibre Raman Amplifier at Different Pump Configurations," in *Proceedings of 2013 Southern African Telecommunication Networks and Application Conference (SATNAC 2013)*, Spier Wine Estate, Stellenbosch, Western Cape, South Africa, 2013.

[299] G. M. Isoe, K. M. Muguro, D. W. Waswa, E. K. R. Kipnoo, T. B. Gibbon, and A. W. R. Leitch, "Performance Comparison of SMF-Reach and SMF-RS Optical Fibres for Raman Amplification," presented at the 59th South African Institute of Physics (SAIP) 2014, University of Johannesburg, South Africa, 2014.

[300] G. M. Isoe, E. K. Rotich, D. K. Boiyo, R. R. G. Gamatham, A. W. R. Leitch, T. B. Gibbon, *et al.*, "Noise figure and pump reflection power in SMF-reach optical fibre for raman amplification," in *AFRICON, 2015*, 2015, pp. 1-5.

[301] B. Zhu, L. Leng, L. Nelson, L. Gruner-Nielsen, Y. Qian, J. Bromage, *et al.*, "3.2 Tb/s (80 x 42.7 Gb/s) transmission over 20 x 100km of non-zero dispersion fiber with simultaneous C+ L-band dispersion compensation," in *Optical Fiber Communication Conference*, 2002, p. FC8.

[302] W. S. Pelouch, "Raman amplification: An enabling technology for long-haul coherent transmission systems," *Journal of Lightwave Technology,* vol. 34, pp. 6-19, 2016.

[303] OFS. (2013, 2017-07-12). *TrueWave Reach low water peak fiber*. Available: http://fiber-optic-catalog.ofsoptics.com/Asset/TrueWaveREACHFiber-124-web.pdf

[304] J. Bromage, "Raman amplification for fiber communications systems," *Journal of Lightwave Technology*, vol. 22, pp. 79-93, 2004.

[305] J. Auyeung and A. Yariv, "Spontaneous and stimulated Raman scattering in long low loss fibers," *IEEE Journal of Quantum Electronics*, vol. 14, pp. 347-352, 1978.

[306] R. H. Stolen, W. Tomlinson, H. Haus, and J. Gordon, "Raman response function of silica-core fibers," *JOSA B*, vol. 6, pp. 1159-1166, 1989.

[307] A. Caballero, N. Guerrero, F. Amaya, F. Amaya, D. Zibar, and I. T. Monroy, "Long reach and enhanced power budget DWDM radio-over-fibre link supported by Raman amplification and coherent detection," *ECOC 2009*, 2009.